Wright State University
CORE Scholar

Browse all Theses and Dissertations | Theses and Dissertations

2015

Integrated Magnetic Components for RF Applications

Sheena Hussaini
Wright State University

Follow this and additional works at: https://corescholar.libraries.wright.edu/etd_all

Part of the Engineering Commons

Repository Citation
Hussaini, Sheena, "Integrated Magnetic Components for RF Applications" (2015). *Browse all Theses and Dissertations*. 1288.
https://corescholar.libraries.wright.edu/etd_all/1288

This Dissertation is brought to you for free and open access by the Theses and Dissertations at CORE Scholar. It has been accepted for inclusion in Browse all Theses and Dissertations by an authorized administrator of CORE Scholar. For more information, please contact library-corescholar@wright.edu.

Integrated Magnetic Components for RF Applications

A dissertation submitted in partial fulfillment of the
requirements for the degree of
Doctor of Philosophy

By

Sheena Hussaini

M.S.E.E., Wright State University, 2011
B. Tech., Jawaharlal Nehru Technological University, 2008

2015

Wright State University

WRIGHT STATE UNIVERSITY
GRADUATE SCHOOL

February 23, 2015

I HEREBY RECOMMEND THAT THE DISSERTATION PREPARED UNDER MY SUPERVISION BY Sheena Hussaini ENTITLED Integrated Magnetic Components for RF Applications BE ACCEPTED IN PARTIAL FULFILLMENT OF THE REQUIREMENTS FOR THE DEGREE OF Doctor of Philosophy.

Yan Zhuang, Ph.D.

Dissertation Director

Ramana V. Grandhi, Ph.D.

Director, Ph.D. in Engineering Program

Robert E. W. Fyffe, Ph.D.

Vice President for Research and

Dean of the Graduate School

Committee on Final Examination

Yan Zhuang, Ph.D.

Marian Kazimierczuk, Ph.D.

Henry Chen, Ph.D.

Robert C. Fitch, Ph.D.

Guru Subramanyam, Ph.D.

© Sheena Hussaini

All Rights Reserved, 2015.

ABSTRACT

Sheena Hussaini. Ph.D., Engineering Ph.D. Program, Wright State University, 2015.
Integrated Magnetic Components for RF Applications.

Integrated r-f passive components such as inductors, transmission lines, transformers etc, form the basic building blocks in r-f integrated circuits (RFICs) such as matching networks, low noise amplifiers (LNAs), synthesizers and r-f mixers. One main challenge faced by current technology developers in integrating r-f components on integrated chip (IC) are related to operation and size. Tremendous efforts were made for overcoming challenges of r-f integrated circuits to meet growing technology demands.

In general, r-f devices utilize magnetic materials such as ferrites for their operation for improving device performance and scaling. However, due to material properties and size ferrite materials are poor choices when attempting to scale r-f components. The main focus of this work has been to explore new material properties and investigate applications of ferromagnetic (FM) films as potential solution for device scaling. One attractive property of ferromagnetic materials is low processing temperature and high magnetic saturation which eliminates the need for continuous application of magnetic (d-c) field and are compatible with CMOS technology. The disadvantage of ferromagnetic films is high conductivity which induces ohmic losses and affects r-f device performance.

In this work a novel concept of low-loss conductor has been introduced whose conductivity can be modeled by utilizing multilayered superlattice structure. The low-loss conductor is made of artificial layered metamaterial (ARLYM) consisting $Ni_{80}Fe_{20}$/Cu superlattice. By modeling thickness ratio between superlattice layers the skin effect has been suppressed by increasing skin depth at r-f frequencies. The experimental results presented in this work indicates significant improvement in r-f

device characteristics such as inductance, quality factor (85%), loss reduction ratio (70%) etc, operating at r-f frequencies. In addition, application of continuous magnetic field was not required in this work due to magnetic anisotropy property in ferromagnetic materials.

Further, a new approach for studying magneto-dynamics in thin ferromagnetic films has been investigated in this work by modeling r-f solenoid single-turn inductor fabricated using thin ferromagnetic core. The effect of magnetic resonances in thin ferromagnetic films has been calculated using magneto-static thin film approximation and Greens function. Therefore, these newly developed concepts of artificial low-loss conductor and magneto-dynamics in thin ferromagnetic structures can be applied for improving speed, clock frequency, power dissipation etc in r-f integrated circuits, microprocessor applications etc, and are fully compatible with CMOS technology.

TABLE OF CONTENTS

CHAPTERS

I. Introduction 1

1.1 Introduction to RF/Microwave Technology 1
1.2 RC Delay 3
1.3 Ferrite Materials 9
1.4 Ferromagnetic Materials 10
1.4.1 Ferromagnetic materials for r-f applications 11
1.5 Objectives 12
1.6 Thesis Outline 13

II. Low-Loss Superlattice Conductor Featured with Skin Effect Suppression for RF Applications 15

2.1 Introduction 15
2.2 Magnetic Permeability in Low-Loss Superlattice 16
2.3 Skin Depth Calculation and Current Distribution in Low-Loss Conductor 20
2.4 Modeling and Calculation of Sheet Resistance 23
2.4.1 Skin Effect Suppression in Low-Loss Conductor . . . 28
2.4.2 Modeling Anti-Magnetic Resonance Frequency . . . 29
2.5 Summary 32
2.6 Conclusion 33

III. Experimental Results for Magnetic Multilayered Meta-Conductors 34

3.1 Introduction 34
3.2 Device Fabrication and Characterization 34
3.2.1 Coplanar Waveguide Device 35
3.2.2 Inductor Device 36
3.3 Experimental Results 38
3.3.1 RF Measurement Setup 38
3.3.2 Materials Characterization 40
3.3.3 Measurement Results 42
3.3.4 Coplanar Waveguide Results 42
3.3.5 Single-turn Inductor Results 45
3.4 Summary 49
3.5 Conclusion 50

IV. Theoretical Study of Magneto-Dynamics in Thin Ferromagnetic Films 51

4.1 Introduction 51
4.2 RF susceptibility in thin ferromagnetic film 53
4.3 Impedance of single-turn inductor utilizing thin ferromagnetic core 64
4.4 Simulation Results 67
4.5 Solenoid Inductor Device Configuration and Fabrication . . . 70
4.6 RF Characterization and Measurement 72
4.7 Experimental Results and Analysis 73
4.8 Conclusions 75

V. Recommendations for Future Work 76

5.1 Conclusions 76
5.2 Future work 78

APPENDICES 80

A. 81

B. 90

C. 105

D. 123

BIBLIOGRAPHY 133

LIST OF FIGURES

Figure

1.1 History of communication (a) Hieroglyphic writing developed by ancient Egyptians around 2900 B.C., (b) Pigeon messengers to send messages (776 B.C.), (c) Air Mail, (d) Alexander Bain's first fax machine, (e) Mobile phone. 1

1.2 Guglielmo Marconi transmits radio signals from Cornwall to Newfoundland. The first wireless transmission radio signal to cross the Atlantic ocean in 1902. 2

1.3 The complexity for minimum device cost and integration complexity increasing nearly by a factor of two per year as predicted by Gordon E. Moore, (Source: Intel-2005) (Left). Road-map of technology generation (Right). 3

1.4 Increasing RC delay (ps) with new technology generation as proposed by international technology road-map for semiconductors (ITRS) (Right). The number of device layers integrated on-chip (Source: IBM) (Left). 4

1.5 RC delay (ns) versus low dielectric constant (k) as proposed by international technology road-map for semiconductors (ITRS). 5

1.6 Improvement in CMOS device performance with Copper (Cu) and Aluminum (Al) interconnects. 6

1.7 Current density across conductor with certain length and diameter at DC/low frequency (Left) and r-f frequency (Right). 7

1.8 Double sub-lattice crystal structure of ferrite materials showing direction of magnetic moment alignment. 9

1.9 Single crystal sub-lattice structure in ferromagnetic materials showing magnetic alignment. 11

1.10 Schematic top view of r-f components utilizing thin ferromagnetic (FM) films. 12

2.1 Low-loss superlattice conductor structure fabricated using alternating layers of non-magnetic (Copper) and magnetic (NiFe) films. 16

2.2 Plots of measured and simulated magnetic permeability (μ) as a function of frequency for single ferromagnetic ($Ni_{80}Fe_{20}$) film with thickness 100nm, length 4mm and width 200μm. The dashed line shows calculated permeability at $\alpha = 2.5\times10^2$. 19

2.3 Plots of calculated effective skin depth versus frequency for low-loss (δ_{eff}) conductor and copper (δ_{Cu}) conductor. 21

2.4 Simulation results showing current distribution across thickness of reference copper (Cu) conductor (a, b, c) and low-loss conductor (d, e, f) at 7, 10 and 14GHz frequency. 23

2.5 Cross-section of low-loss superlattice conductor with thickness (t). The total thickness (t) comprises of copper metal (t_{Cu}) and ferromagnetic (t_{NiFe}) layers. 24

2.6 Plots of sheet resistance (ρ_s) versus frequency for low-loss superlattice conductor ($Ni_{80}Fe_{20}$/Cu) for different number of superlattice layers (N= 9, 17, 25 and 37) with constant thickness ratio (r=3). The total thickness of low-loss and copper conductors are 6.7μm. 29

2.7 Plots of sheet resistance (ρ_s) versus frequency for superlattice (NiFe/Cu) conductor with total thickness 6.7μm and different thickness ratios (i) r=1.0, N=33 (ii) r=2.0, N=22 (iii) r=3.0, N=16. The thickness of Cu and NiFe are t_{Cu} and t_{NiFe}. 'N' is number of layers in superlattice. 30

2.8 Plots of sheet resistance (ρ_s) versus frequency for low-loss superlattice (NiFe/Cu) conductor with constant thickness ratio (r=3) with varied NiFe thickness and number of layers (N) (i) t_{NiFe}=50nm, N=33 (ii) t_{NiFe}=100nm, N=16 (iii) t_{NiFe}=150nm, N=10. The total thickness of low-loss superlattice and copper conductors are 6.7μm. 31

2.9 Plots of sheet resistance (ρ_s) versus frequency for low-loss superlattice (FeCo/Cu) with thickness 6.7μm. The thickness of FeCo is 50nm with varying thickness ratio and number of layers (N) (i) r=1.0, N=67 (ii) r=2.0, N=44 (iii) r=3.0, N=33. 32

3.1 Coplanar waveguide (CPW) device (a) Structure and design in ADS, (b) Surface morphology, (c) Undercut measured using Atomic force microscopy (AFM). 36

3.2 Structure of single-turn spiral inductor designed using Advanced design system (ADS). 37

3.3 Measurement setup showing cascade r-f wafer probe station (M150), network analyzer and r-f probes connected using cables. 38

3.4 Plot of extracted magnetic permeability (μ) versus frequency for ferromagnetic permalloy ($Ni_{80}Fe_{20}$) film. 40

3.5 Plots of magnetic B-H loop for single ferromagnetic ($Ni_{80}Fe_{20}$) layer and low-loss multilayer superlattice (ARLYM) conductor. 41

3.6 Measured attenuation per length as a function of frequency for CPW built using multilayer (#1) listed in table-(3.1) and reference copper (Cu). 42

3.7 Propagation wavelength as a function of frequency for coplanar waveguide (CPW) built using multilayer low-loss superlattice (#1) listed in table-(3.1) and reference copper (Cu). 43

3.8 Loss reduction ratio (η) versus signal line width for coplanar waveguide (CPW) devices listed in table-(3.1). 44

3.9 Plots of measured inductance (L) as a function of frequency for fabricated single-turn inductors. 45

3.10 Plots of measured resistance (R) as a function of frequency for single-turn inductors. 46

3.11 Plots of measured quality factor (Q) as a function of frequency for fabricated single-turn inductors. 47

3.12 Relative quality factor versus inductance at different frequencies (a) 10GHz (b) 12.5GHz (c) 15GHz for fabricated single-turn inductors. 49

4.1 Solenoid inductor built using thin ferromagnetic film and magnetic coil separated by dielectric layers (top). The cross-section of thin ferromagnetic stripe across x-y plane (bottom). 53

4.2 Plots of eigen functions $\psi_k(x)$ for different modes across width (300μm) and thickness (0.3μm) of thin ferromagnetic film. 61

4.3 Real and imaginary part of susceptibility (χ^q_{xx}) versus frequency for thin ferromagnetic film for four eigen modes. The width and thickness of ferromagnetic stripe are 300μm and 0.3μm 63

4.4 Plots of resistance (R) and inductance (L) versus frequency for single-turn inductor with length 1mm. The thin ferromagnetic film inductor core with width $300\mu m$ and thickness $0.3\mu m$. 68

4.5 Plots of resistance (R) and inductance (L) versus frequency for single-turn inductor with length 1mm and various ferromagnetic film widths. 69

4.6 Plots of resistance (R) and inductance (L) versus frequency for single-turn inductor with length 1mm and variations in damping constant. 70

4.7 Single-turn inductors designed in Advanced design system (ADS). . 71

4.8 ADS layout of single-turn solenoid inductors with various structural parameters. 72

4.9 Plots of measured resistance (R) and inductance (L) versus frequency for single-turn inductor (Row1-Column2) with signal line width (W_1) 10μm, NiFe pattern width (W) 300μm, NiFe pattern length (L) 1000μm, NiFe Pattern (Solid), Device position (Center), Total device length 1200μm. 73

4.10 Plots of measured resistance (R) and inductance (L) versus frequency for single-turn inductor (Row2-Column8) with signal line width (W_1) 20μm, NiFe pattern width (W) 300μm, NiFe pattern length (L) 1000μm, NiFe Pattern (Solid), Device position (edge-1), Total device length 1200μm. 74

B.1 Figures showing (a) Impedance standard calibration substrate, (b) Short-Open-Load-Thru (SOLT) (c) r-f probe contact on load structure, (d) r-f infinity probes. 91

B.2 Calibration measurement results in magnitude (dB) versus frequency for (a) Open, (b) Load, (c) Short and (d) Thru. 92

B.3 Calibration measurement results on Smith chart for (a) Open, (b) Load, (c) Short and (d) Thru. 93

B.4 Signal flow graph (SFG) for forward model associated with 12 error-terms to calculate forward error terms. 95

B.5 Signal flow graph (SFG) for reverse model associated with 12 error-terms to calculate reverse error terms. 97

B.6 Signal flow graph (SFG) of S-parameter 2-port network. 101

B.7 Signal flow graph (SFG) for Thru de-embedding structure. 103

C.1 Representation of current density across surface 108

C.2 Representation of point source 'Q' and observation point 'P' with reference to origin in xyz plane 112

C.3 Plots of function $|\vec{r}|$ and its derivative $\frac{d|\vec{r}|}{dr}$ 116

D.1 AFM image of diluted (1:100) graphene oxide (Left) and concentrated graphene oxide (Right). 124

D.2 Thickness distribution of diluted graphene oxide (GO). 124

D.3 Coplanar waveguide (CPW) device with meander load. The width (W) and spacing (S) of meander line are 3μm and 10μm 125

D.4 Measured resistance versus frequency for coplanar waveguide (CPW) devices. 127

D.5 Measured reactance versus frequency for coplanar waveguide (CPW) devices. 127

D.6 RF impedance measured for coplanar waveguide (CPW) devices. (1) CPW, (2) CPW coated with graphene, (3) CPW coated with graphene and chitosan, (4) CPW coated with graphene, chitosan and DNA. 128

D.7 Measured change in resistance at resonance frequencies. (1) CPW, (2) CPW coated with graphene, (3) CPW coated with graphene and chitosan, (4) CPW coated with graphene, chitosan and DNA. 129

D.8 Equivalent circuit of coplanar waveguide (CPW) input impedance. . 130

LIST OF TABLES

Table

1.1 List of metals and corresponding conductivity values. 6

2.1 Materials with examples and corresponding permeability values. . . 16

2.2 Anti-resonance frequency and magnetic saturation for magnetic materials. 32

3.1 Design parameters of fabricated coplanar waveguides (CPWs) built using artificial layered metamaterial (ARLYM) low-loss conductor. . 36

3.2 Design parameters of fabricated single-turn inductors. 37

3.3 Fabricated single-turn inductors with various structural parameters width (W), length (L), and coil line width (d). 38

4.1 Single-turn inductor configuration with ferromagnetic (NiFe) pattern width (300μm), insulating layer (SiO_2) thickness (0.5μm), NiFe pattern length 1000/2000 (μm) and total device length 1200/2200 (μm). 70

D.1 Structural parameters of fabricated coplanar waveguides (CPWs). . 125

D.2 Effective substrate permitivity after adding chemicals. 131

ACKNOWLEDGEMENTS

Over the past years, I have benefited from help, encouragement and support offered by many people. This thesis would not be complete without acknowledging their contributions; and I shall attempt to express my deepest gratitude towards them here.

First and foremost, I would like to offer my deepest gratitude and thanks to my dissertation advisor, Dr.Yan Zhuang for his immense support and encouragement throughout all these years. Dr.Zhuang has always encouraged and showed me importance of being persistent while doing research by providing great examples when required.

I would like to thank Department of Electrical Engineering previous chair Dr.Kefu Xue for his immense support during my study at Wright State. A very special thank you goes to my dissertation committee members Dr.Marian Kazimierczuk, Dr.Robert C. Fitch, Dr.Henry Chen and Dr.Guru Subramanyam for serving on my dissertation committee and providing valuable suggestions. I would also like to offer special thanks and gratitude to my masters thesis committee members Dr.Saiyu Ren, Dr.Kuan-Lun-Chu, Dr.Kefu Xue and thesis advisor Dr.Yan Zhuang for their encouragement and support.

For successful completion of this dissertation work, I am also indebted and thankful to Dr.Behzad Rejaei from University of Tehran, Iran for providing guidance with single-turn inductor analysis and HFSS simulations. This thesis would not be complete without acknowledging his contribution and support. I would also like to offer my special thanks to Dr.Robert C. Fitch from Sensors Directorate, Air Force Research Laboratory (AFRL) at Wright-Patterson AFB for his contribution and help with cleanroom procedures and device fabrication. I am also very grateful to graduate advisor Mr.Ryan Hamilton and staff at Department of Electrical Engineering,

Wright State University. I would like to offer my deepest gratitude to lab manager Mr.Tony Tritschler for his help with lab equipment in Microwave laboratory and Ph.D. program coordinator Alysoun Taylor-Hall for her guidance and support.

I would like to thank my colleagues and fellow members of RF/Microwave research group at Wright State University: My colleagues Joshua Myers and Timothy Nicodemus who were always very kind and helpful. Gregory C. Hartman for performing mask design and device fabrication at Air force research laboratory (AFRL). My special thanks to previous group member Ruiping Zhou and colleague Kathleen Brockdorf for their immense support and encouragement. I would also like to thank all my other wonderful group members Timothy Sandoval, Jared Evans, Bella Yao, Pradyumna Aditya, Zhonghang Ji, Hyung Min Jeon, Jiahui Wang and many others. Thanks for all your support and making my research experience so valuable.

I am also indebted and thankful to have met some wonderful people during my research at Wright State. A very special thanks goes to Pedram Khalili from Device Research Laboratory (DRL) at University of California, Los Angeles (UCLA) for his valuable time and discussion. I am also thankful to Prof. Masahiro Yamaguchi from Department of Electrical and Communication Engineering, Tohoku University for providing brief insight into his research work. Lastly, I am indebted and thankful to Prof.Nian X. Sun from Northeastern University for his valuable time.

A very special thank you goes to all my fellow teaching assistants for their help with handling and scheduling labs. While one attends university to study and work on research, often the most valuable experiences in this environment are associated with people one gets to meet. In this spirit, I would like to thank all my friends and fellow classmates at Wright State, for making all these years so valuable.

Last but not least, I would like to thank all my family members for their constant support and encouragement. A very special thank you goes to Syed Hussaini, for his constant support. I am grateful to my late grandparents who will always remain a

great source of inspiration and motivation for rest of my life. I am very thankful to my dear brother, Saif who always encouraged and supported me to pursue my goals. I would also like to thank my sweet sisters, Mizba and Zeba, for all their kindness and love. I would like to thank my relative and also a dear friend Shahriyar (Sheiri) for always being there for me. Lastly, I would like to thank my childhood friend Rani with whom I had great time spending all those memorable years.

Dedicated to my family, friends and colleagues

CHAPTER I

Introduction

1.1 Introduction to RF/Microwave Technology

The biggest challenge faced by mankind during ancient time was related to effective long distance communication [1]. Over period of time new effective means of communication techniques evolved due to technological progress and advancement which allowed humans to connect globally within no time (figure-1.1) [1].

(a) (b) (c)

(d) (e)

Figure 1.1: History of communication (a) Hieroglyphic writing developed by ancient Egyptians around 2900 B.C., (b) Pigeon messengers to send messages (776 B.C.), (c) Air Mail, (d) Alexander Bain's first fax machine, (e) Mobile phone.

The current wireless communication techniques such as long-term evolution (LTE), 3G and 5G networks are developed based on discovery of James Maxwell in 1873 [1]. The theory of electromagnetic wave propagation discovered by Maxwell during

early nineteenth century has completely revolutionized microwave industry and is considered as most significant discovery in history of mankind [1, 2]. The microwave technology first came into existence during the period of World War II (1939-1945) [1]. During initial period (i.e., before 1980's) microwave technology was limited to defense and radar applications due to large component size and cost operating at high frequencies (2-15GHz) [3].

Figure 1.2: Guglielmo Marconi transmits radio signals from Cornwall to Newfoundland. The first wireless transmission radio signal to cross the Atlantic ocean in 1902.

Due to recent progress and advancement in semiconductor industry the size of components began to shrink continuously leading to large device integration (ULSI) on-chip [4]. As a result devices with increased functionality and affordable cost came into existence such as computers, digital cameras, mobile phones etc [1]. These devices can handle multiple operations and functionality at same time [5, 6]. Therefore, in today's integrated circuits the crucial parameters are size, cost and performance [4, 7]. On the other hand microwave industry began to expand and explore new areas such as communications, radar, military applications etc, in order to meet with growing technology demands [8].

1.2 RC Delay

In last 65 years ever since invention of first transistor in 1947 at AT&T Bell Laboratories there has been continuous improvement in device technology, size, cost, performance etc, leading to increased device density and functionality [1]. As a result of device scaling and integration more devices are being integrated on-chip as demonstrated by Moore's law in figure-(1.3) [4].

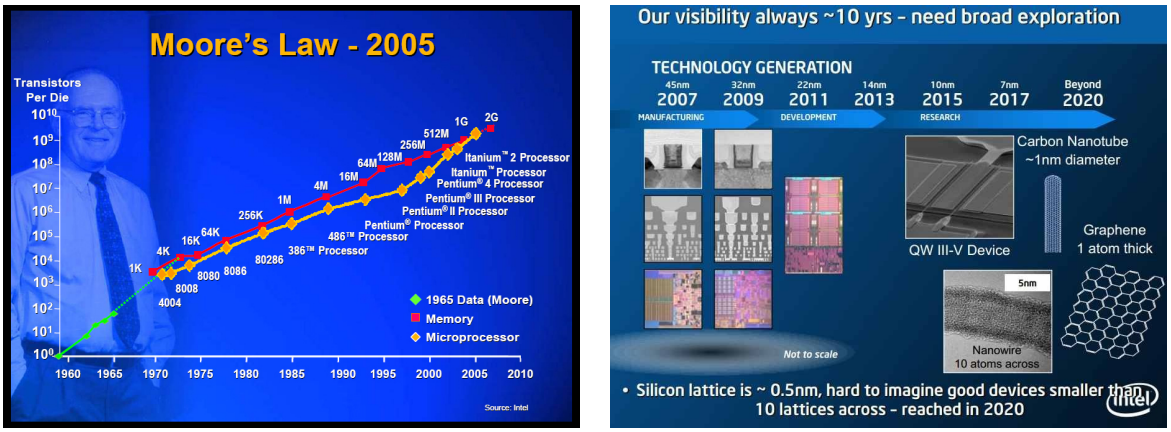

Figure 1.3: The complexity for minimum device cost and integration complexity increasing nearly by a factor of two per year as predicted by Gordon E. Moore, (Source: Intel-2005) (Left). Road-map of technology generation (Right).

Based on prediction of G.E. Moore the number of transistors integrated on-chip (IC) increases by a factor of two for every eighteen months [4]. Therefore, advancements in CMOS technology and device scaling led to devices with increased speed, device density, affordable cost and minimum power consumption [5, 6, 9]. The figure-(1.3) (right) shows evolution of technology generation due to improved device integration and scaling. It can be noticed in figure-(1.3) that in between years 1960 and 2000 there is dramatic rise in magnitude of number of transistors integrated on-chip by nearly nine orders which caused device dimensions to shrink continuously for accommodating more and more components on-chip (Moore's Law) [4]. Therefore, RC delay, cross-talk noise and power relating to RC interconnects are major limiting fac-

tors caused due to device integration which affects device performance [10, 11, 12, 15, 16-21]. The RC delay is caused due to interconnects i.e., wires required for connecting components on-chip. The problems related to RC delay continue to rise further as we approach to new technology generations in future by year 2020 [11, 12].

The figure-(1.4) demonstrates increasing RC delay with new technology generations as proposed by international technology road-map for semiconductors (ITRS) and shows number of device layers integrated on-chip.

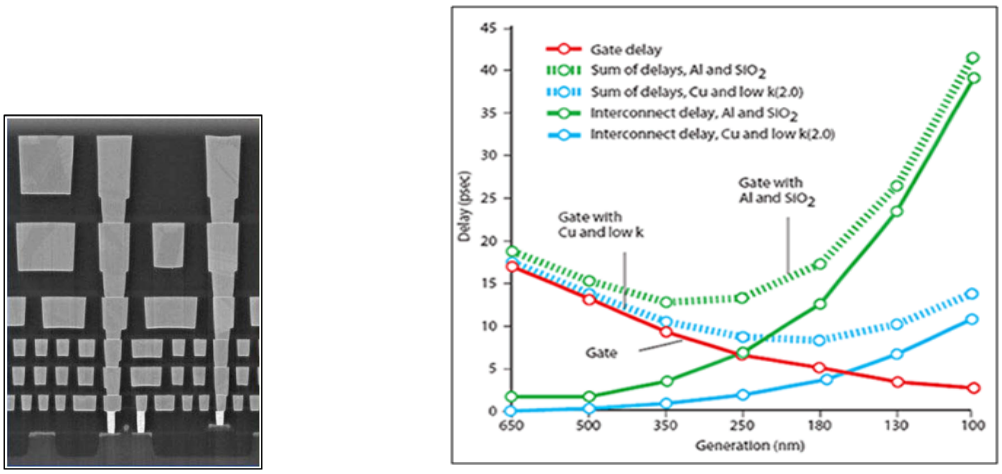

Figure 1.4: Increasing RC delay (ps) with new technology generation as proposed by international technology road-map for semiconductors (ITRS) (Right). The number of device layers integrated on-chip (Source: IBM) (Left).

Based on prediction of international technology roadmap for semiconductors (ITRS) as we approach towards 22nm technology generation by year 2016 there is strong need to investigate new approaches and materials with improved conductivity and permittivity values to meet growing technology demands and minimize RC delay [12]. The clock distribution techniques used in high performance microprocessor, off-chip integration, asynchronous distribution etc, are depended on minimizing RC delay which improves clock frequency [12, 13, 14, 17, 18]. Therefore, minimizing interconnect RC delay causes significant improvement in speed and performance of integrated circuits [11, 12]. On the other hand r-f integrated circuits (RFICs) and devices are having

major limitations and difficulties in maintaining same pace as its digital counterpart [1]. The major reason is that numerous factors are considered for integrating r-f devices on-chip which requires new techniques and approaches for r-f device integration. Therefore, main focus of this research work has been to investigate new methods and techniques for minimizing RC delay.

In general, there are two approaches proposed by international technology roadmap for semiconductor (ITRS) for improving RC delay. The first approach for minimizing RC delay is by using low-dielectric (k) materials as inter-layer dielectrics which reduces capacitance (C) [11, 12, 13, 14, 15]. The main challenge in implementing this approach of low-k-dielectric materials is depended on developing material with low dielectric constant (k) value and good thermal or mechanical stability [12, 13, 14, 15, 16].

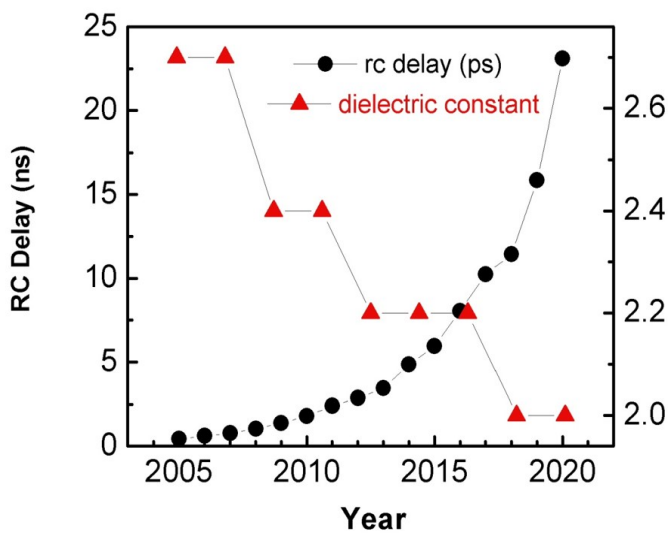

Figure 1.5: RC delay (ns) versus low dielectric constant (k) as proposed by international technology road-map for semiconductors (ITRS).

The figure-(1.5), shows RC delay (ns) versus low-dielectric (k) constant material values as suggested by international technology road-map for semiconductor (ITRS) [22]. In future, if material with lowest dielectric (k) constant value (i.e. ideal medium such as vacuum) i.e., 2.0 is implemented then improvement in RC delay is limited by

25% by year 2020 (figure-1.5) [12, 13, 14]. Therefore, approach of utilizing low dielectric (k) constant materials for minimizing RC delay is not suitable for eliminating RC delay problem.

The only alternative approach proposed for minimizing RC delay is by reducing resistance (R) using conductor with low-loss and improved conductivity [12, 13, 14].

The list of various metals and their corresponding conductivity values are shown in table-(1.1). The current semiconductor industry utilizes copper (Cu) metal whose conductivity value ($\sigma = 6\times10^7$S/m) is slightly less (5%) than silver (Ag) which has the highest conductivity at room temperature (table-1.1) [12, 13, 14].

Metal	**Conductivity (S/m)**
Ag	6.3x10^7
Cu	6.0x10^7
Au	4.1x10^7
Al	3.5x10^7

Table 1.1: List of metals and corresponding conductivity values.

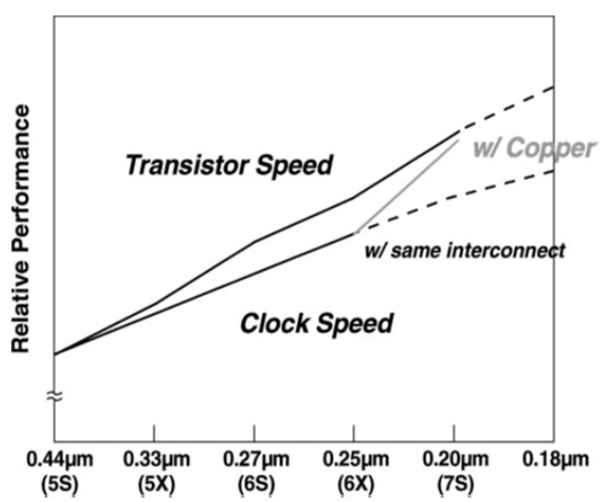

Figure 1.6: Improvement in CMOS device performance with Copper (Cu) and Aluminum (Al) interconnects.

The main advantage of using copper conductor is low resistivity, increased scalability, improved current carrying capability (i.e. high conductivity) and improved

performance [10, 12, 13, 14, 16].

The figure-(1.6), shows the result of using copper interconnects for CMOS applications which indicates that copper interconnects provides increased clock speed nearly equal to transistor speed when compared to Al interconnects [16]. The main challenge in utilizing conductor with high conductivity (Copper) for minimizing RC delay is rather limited.

In case of DC (or) low frequency applications the resistance (R) can be minimized by increasing thickness of conductor beyond certain skin depth value which reduces ohmic or metal losses by improving current distribution across conductor [12, 13, 14]. However, method of increasing conductor thickness is not effective when dealing with high (or) r-f frequencies. The reason behind is that at r-f or high frequencies the ohmic losses in conductor are depended on finite conductivity (σ) value and skin effect as demonstrated in figure-(1.7) [11, 12, 13, 14]. The skin effect is defined as the ability of electric current to flow only on surface of the conductor within certain depth into conductor known as skin depth (δ) at r-f (or) high frequencies [12, 13, 14].

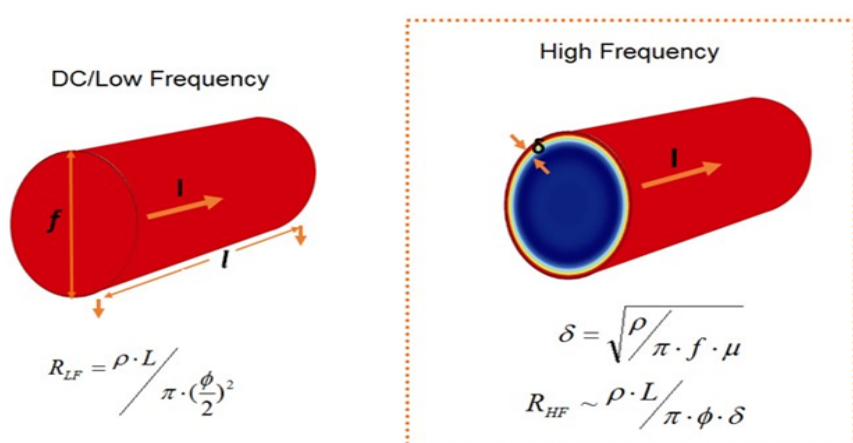

Figure 1.7: Current density across conductor with certain length and diameter at DC/low frequency (Left) and r-f frequency (Right).

The figure-(1.7) demonstrates the current density in conductor across diameter (d)

and length (l). It can be noticed in figure-1.7 (left) that at DC (or) low-frequencies the skin depth is large when compared to thickness of conductor i.e., uniform current distribution across entire volume of conductor [12, 18, 23]. At DC (or) low frequency the skin effect can be minimized by using thick metal layers or by increasing diameter of conductor.

However, this approach of increasing conductor thickness and diameter for improving skin depth cannot be applicable at r-f or high frequencies due to skin effect [11, 12, 13, 14]. It can be noticed in figure-1.7 (right) that at r-f or high frequencies the current density is maximum at conductor surface and decreases with conductor depth which causes ohmic losses in r-f (or) microwave circuits [16, 23]. The depth of current penetration into conductor at r-f frequencies is known as skin-depth (δ) calculated by formula listed in equation-(1.1) [12, 13, 14].

$$\delta = \sqrt{\frac{2}{\omega\sigma\mu_0}} \tag{1.1}$$

In equation-(1.1), 'ω' is angular frequency given by ω=2πf. Where, 'f' is frequency and 'μ_0' is vacuum permeability [12, 13, 14]. The skin depth in equation-(1.1) depends on resistivity (ρ), frequency (f) and permeability (μ). Therefore, based on equation-(1.1), the skin depth at r-f or high frequencies can be improved by investigating material having low-loss and improved conductivity. As mentioned earlier in this chapter the approach of utilizing conductor with high or improved conductivity (Copper) is rather limited. Therefore, the only alternative method is utilizing materials with low permeability value (i.e., magnetic materials) for improving skin depth at r-f frequencies.

1.3 Ferrite Materials

The magnetic materials such as ferrites were discovered during the period of world war-II by J.L Snoek at Philips Laboratory. Snoek studied ferrite material properties and demonstrated that magnetic losses increases as a function of frequency. In addition, he also demonstrated that materials with high permeability cannot be used for low-loss applications at r-f frequencies. In later years further explanations related to spin resonance were provided by Kittel using classical equations of motion to describe magnetic dipole moment alignment and internal magnetic field in ferrite materials. The ferrite materials are also applicable as dielectric layers for r-f applications as they restrict the flow of parasitic currents into the substrate which significantly minimizes substrate losses. In general, r-f components are built with ferrite materials as their core for improving device performance. The main attractive property of ferrite materials is high resistivity which leads to lower losses.

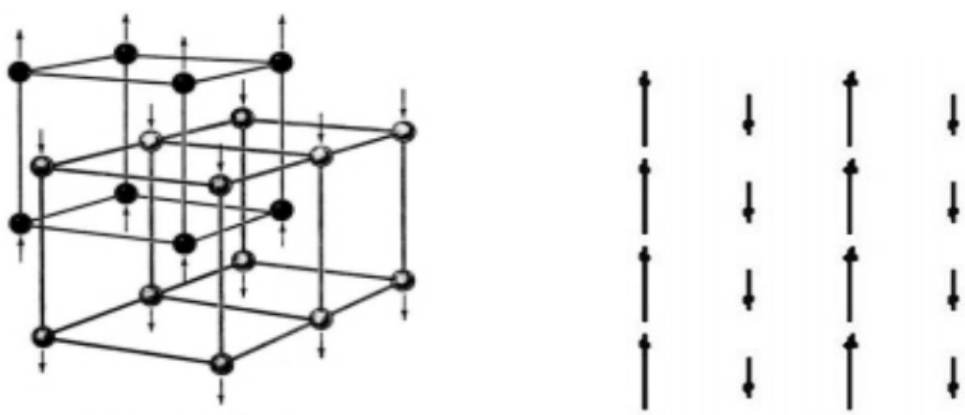

Figure 1.8: Double sub-lattice crystal structure of ferrite materials showing direction of magnetic moment alignment.

On the other hand r-f components built using ferrite magnetic materials require continuous application of magnetic field for aligning magnetic moments depending on double sublattice crystal structure (figure-1.8) [24, 25].

Therefore, utilizing ferrite materials for r-f components makes r-f device scaling

even more difficult. In addition, ferrite materials require high processing temperatures in range 500°-900^oC for relieving internal stress and attaining high permeability values. The high processing temperatures for ferrite materials in integrated circuits makes these materials incompatible with current semiconductor technology (CMOS) [26]. The other major drawback of ferrite materials is low magnetic saturation (M_s<0.1) which limits their application to low frequencies.

Previously, tremendous efforts and investigations were performed for improving on-chip r-f device performance and RC delay but it lead to increased device size and cost [12, 13, 14, 27]. A new approach of integrating thin ferromagnetic (FM) films with high permeability has been investigated in this work for improving r-f device size and performance leading to r-f integration into mainstream silicon technology [12, 13, 14, 28]. Therefore, ferromagnetic materials are chosen as most suitable alternative candidates for r-f device applications such as inductors, transmission lines, transformers, coplanar waveguides etc, [29].

1.4 Ferromagnetic Materials

Ferromagnetic (FM) materials comprises of single sub-lattice crystal structure as demonstrated in figure-(1.9) which shows magnetic moments aligned along same direction [24, 25]. The main advantage of ferromagnetic materials is high permeability and their ability to reach high magnetic saturation (M_s) in range 1.1-2.4 Tesla without applying external (d-c) magnetic field due to magnetic moment alignment in lattice structure. In addition, ferromagnetic materials require low processing temperature for fabrication which makes them compatible with CMOS technology.

One main disadvantage of ferromagnetic materials is high conductivity which leads to loss and degradation in r-f device performance.

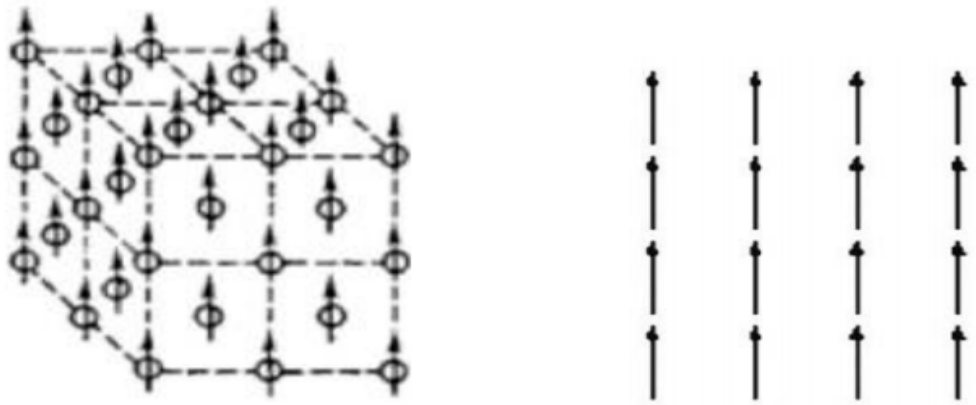

Figure 1.9: Single crystal sub-lattice structure in ferromagnetic materials showing magnetic alignment.

1.4.1 Ferromagnetic materials for r-f applications

As discussed earlier r-f devices in integrated circuits make use of magnetic materials such as ferrites and ferromagnetic materials for improving device characteristics, size and performance. The main disadvantage of r-f planar inductors integrated on-chip is large area and low quality factor [9]. In general, air core inductors are surrounded by non-magnetic layers which limits energy stored by these components. The energy storage capability of r-f devices increases with permeability. Therefore, incorporating high permeability materials (i.e., magnetic materials) improves the quality factor of r-f inductor components significantly.

The figure-(1.10) shows applications of thin ferromagnetic film for various r-f devices such as inductors, transmission lines, coplanar waveguides etc,.

In case of transmission lines integrated on-chip the use of thin ferromagnetic materials with high permeability causes the propagation velocity and wavelength to decrease at specific frequency which leads to reduction in on-chip device size. In addition, transmission lines fabricated by incorporating thin ferromagnetic (FM) films leads to increase in device characteristics such as characteristic impedance, quality factor and decrease in attenuation and propagation wavelength [30].

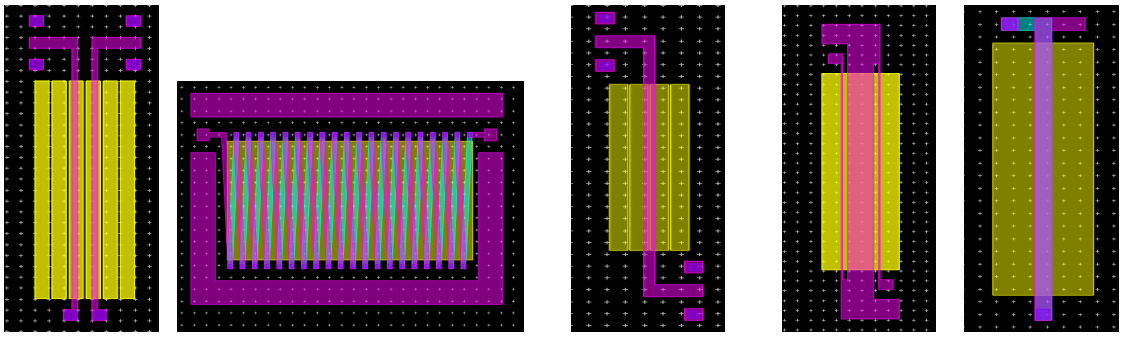

Figure 1.10: Schematic top view of r-f components utilizing thin ferromagnetic (FM) films.

The integrated r-f solenoid inductors built using patterned ferromagnetic (NiFe) films provides increase in magnetic flux associated with inductor coil leading to significant enhancement in inductance (L) and quality factor (Q) when compared to reference air core inductors [30, 31, 32, 33, 34, 35, 36]. On the other hand, planar inductors fabricated using thin ferromagnetic (FM) films suffered from drawbacks such as low ferromagnetic resonant frequency (FMR), magnetic precession and eddy current loss which lead to poor quality factor [9, 12, 13, 14, 37, 38, 39, 40].

In reality, an ideal conductor having maximum conductivity and minimum permeability (i.e., zero) values does not exist [12, 13, 14]. Therefore, main focus of this work has been to investigate and explore new materials having low permeability and improved conductivity values. A novel concept has been introduced in this work (chapter-2) for dealing with RC delay and increasing skin depth at r-f frequencies.

1.5 Objectives

The main objectives addressed in this dissertation are as follows:

• Investigate new approach and materials for minimizing RC delay and increasing skin depth at r-f frequencies.

• Perform r-f device characterization and experimental analysis for fabricated r-f devices such as single-turn inductors, coplanar waveguides (CPWs) etc, with various

structural parameters.

• Investigate new approach for studying magneto-dynamics in thin ferromagnetic films based on r-f single-turn inductors built using thin ferromagnetic core.

• Modeling the effect of magnetic resonances occurring in thin ferromagnetic films using magneto-static thin film approximation and Green's function.

1.6 Thesis Outline

The outline of this dissertation is summarized as follows:

• **Chapter 1: Introduction**

The introduction chapter begins with brief introduction to r-f (or) microwave technology and RC delay. The next section demonstrates introduction to various magnetic materials such as ferrites and ferromagnetic materials. The complexity and challenges related to r-f device integration has been addressed. Lastly, the need for integrating thin ferromagnetic (FM) films as potential solution for r-f device integration and their corresponding advantages are listed.

• **Chapter 2: Low-Loss Superlattice Conductor Featured with Skin Effect Suppression for RF Applications**

A novel concept of artificial low-loss superlattice (ARLYM) conductor has been introduced in this chapter which provided effective skin effect suppression at r-f frequencies. The equations for modeling and extracting magnetic permeability inside low-loss superlattice are outlined. The skin depth calculation and current distribution across artificial low-loss superlattice (ARLYM) conductor are presented. Lastly, simulation results for modeling skin depth and anti-magnetic resonance frequency are listed.

• **Chapter 3: Experimental Results for Magnetic Multilayered Meta-Conductors**

The device fabrication, characterization and measurement analysis for various r-f devices such as inductors, coplanar waveguides (CPWs) etc, built by utilizing ar-

tifical multilayered metaconductor (ARLYM) concept are presented in this chapter. The material characterization and experimental results for r-f single-turn inductors and coplanar waveguide components are presented in this chapter showing significant enhancement in r-f device characteristics and impedance parameters.

- **Chapter 4: Theoretical Study of Magneto-Dynamics in Thin Ferromagnetic Films**

The theoretical equations and experimental results for single-turn solenoid inductors fabricated using thin ferromagnetic film are presented in this chapter. The calculation of r-f susceptibility for thin ferromagnetic film based on Green's function has been presented. The impedance of single-turn inductor calculation and modeling results are illustrated. In addition, simulation results obtained by varying device parameters such as width, core length and magnetic loss are also presented in this chapter [42]. Lastly, magneto-static resonances caused by utilizing thin magnetic films has been investigated and verified in this work.

CHAPTER II

Low-Loss Superlattice Conductor Featured with Skin Effect Suppression for RF Applications

2.1 Introduction

A novel concept of low-loss conductor is introduced in this chapter based on artificial layered metamaterial (ARLYM) superlattice which provides improvement in skin depth by providing uniform current distribution at r-f frequencies [11, 12, 13, 14].

The propagation of electromagnetic waves in superlattice structure fabricated using dielectric and ferromagnetic (FM) films was studied by R.E. Camley and D.L. Mills [11, 38, 41]. They investigated decrease in attenuation for ferromagnetic films at anti-resonance frequency which caused significant skin effect suppression and increased skin depth [11, 38]. The main drawback of their approach was high resistivity in ferromagnetic films which led to poor quality factor.

In this work, a new concept of low-loss conductor (ARLYM) has been introduced by using alternating layers of metal (Cu) and ferromagnetic ($Ni_{80}Fe_{20}$) thin films as shown in figure-(2.1). The low-loss conductor consists of superlattice with non-magnetic high conductivity metal (Cu) layer and magnetic material ($Ni_{80}Fe_{20}$) with low permeability as illustrated in table-(2.1). When external magnetic field is applied perpendicular to ferromagnetic layer then magnetic permeability (i.e., real part) becomes negative between ferromagnetic resonance (FMR) and anti-resonance (AR) frequency as shown in figure-(2.2) [10, 11]. This attractive property of negative permeability in ferromagnetic films makes the overall permeability of artificial low-loss conductor to zero by modeling the thickness ratio between metal and ferromagnetic

films (equation-2.4) [11]. The field generated by current along magnetization makes the overall permeability in low-loss conductor small (i.e., nearly zero). Therefore, skin depth in low-loss conductor has been increased (equation-1.1) causing uniform current distribution and skin effect suppression [11].

Material	Example	Permeability
Non-magnetic	Cu, Ag, Au	1.0
Magnetic	NiFe	Negative below FMR

Table 2.1: Materials with examples and corresponding permeability values.

2.2 Magnetic Permeability in Low-Loss Superlattice

The figure-(2.1) shows the proposed structure of low-loss artificial layered metamaterial (ARLYM) superlattice conductor built using alternating layers of metal (Cu) and ferromagnetic (FM) films [11, 12, 27].

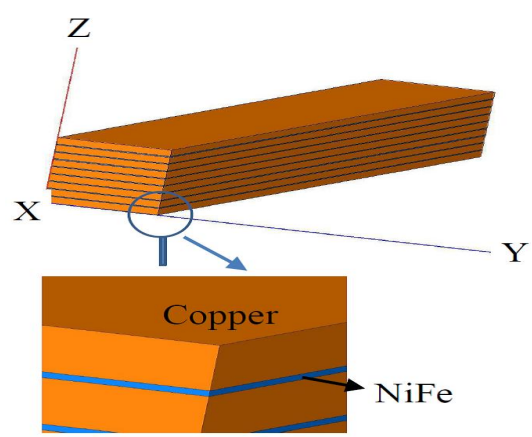

Figure 2.1: Low-loss superlattice conductor structure fabricated using alternating layers of non-magnetic (Copper) and magnetic (NiFe) films.

The ferromagnetic (FM) thin film is magnetized along x-direction with magnetization ($M_s\hat{x}$) by applying magnetic (d-c) field ($H_0\hat{x}$) along x-axis [42, 43]. In ferromagnetic (FM) film the electric current causes r-f magnetic field in perpendicular direction of film [11, 12, 13, 14, 42, 43]. Therefore, permeability in low-loss con-

ductor has been calculated by assuming length (l) of ferromagnetic thin stripe along x-direction much longer than width (w) along y-axis ($l >> w$).

Based on small-signal condition assumption the r-f magnetization vector ($\vec{m}$) is small when compared to magnetic saturation (M_s) [$\vec{m} << M_s$]. Therefore, longitudinal component of r-f magnetization vector has been neglected since stripe is magnetized along x-axis ($\vec{m} = m_y\hat{y} + m_z\hat{z}$) [11, 42].

The permeability tensor ($\check{\mu}$) of ferromagnetic film in low-loss superlattice structure is given by equation-(2.1). The derivation equations for permeability tensor ($\check{\mu}$) are listed in Appendix-(A) [11, 42].

$$\check{\mu} = \begin{bmatrix} 1 & 0 & 0 \\ 0 & \mu & -j\mu_a \\ 0 & j\mu_a & \mu \end{bmatrix} \tag{2.1}$$

Where,

$$\mu = 1 + \frac{\omega_H \omega_M}{\omega_H^2 - \omega^2} \tag{2.2}$$

$$\mu_a = \frac{\omega_M \omega}{\omega_H^2 - \omega^2} \tag{2.3}$$

$$\omega_M = \gamma M_s, \omega_H = \gamma H_0$$

In above equations (2.1)-(2.3), 'γ' is gyromagnetic factor, 'M_s' is magnetic saturation and 'H_0' is magnetic anisotropy field [1, 11]. The modeling simulations for low-loss conductor are performed by considering superlattice structure as metamaterial with thickness of copper (t_{Cu}) and ferromagnetic (t_{NiFe}) films small when compared to skin depth [1, 11, 42].

The effective permeability (μ_{eff}) of low-loss conductor superlattice structure is given by equation-(2.4) [10, 11, 12, 13, 14, 42, 44].

$$\mu_{eff} = \mu_0 \frac{\mu_\perp t_{NiFe} + t_{Cu}}{t_{NiFe} + t_{Cu}} \tag{2.4}$$

In equation-(2.4), the thickness of copper and ferromagnetic layers are 't_{cu}' and 't_{NiFe}'. Where, '$\mu_{\perp}$' is relative permeability of ferromagnetic film [12, 13, 14]. The relative permeability ($\mu_{\perp}$) of ferromagnetic film is given by equation-(2.5) and calculated by applying magnetic (d-c) field along ferromagnetic film (i.e., easy axis). The relative permeability ($\mu_{\perp}$) is a complex quantity which consists of magnetic loss [10, 11, 12, 13, 14].

$$\mu_{\perp} = \mu - \frac{\mu_a^2}{\mu} = \frac{f_{AR}^2 - f^2}{f_{FMR}^2 - f^2} \tag{2.5}$$

In equation-(2.5), 'f_{FMR}' is ferromagnetic resonance (FMR) frequency given by equation-(2.6) (Kittel formula) [10, 12].

$$f_{FMR} = (\gamma/2\pi)\sqrt{H_0\,(H_0 + M_s)} \tag{2.6}$$

The ferromagnetic resonance frequency (FMR) in simulation modeling is considered by substituting $H_0 \rightarrow H_0 + i\,(2\pi f/\gamma)\,\alpha$ for magnetic anisotropy field. Where, 'α' is Gilbert damping constant [12, 13, 14, 20, 45].

The anti-resonance frequency (f_{AR}) is given by equation-(2.7) and is frequency at which effective permeability (μ_{eff}=0) of low-loss superlattice conductor goes to zero (equation-2.4) [12, 13, 14].

$$f_{AR} = (\gamma/2\pi)\,(M_s + H_0) \tag{2.7}$$

The figure-(2.2) shows the plot of permeability (μ) as a function of frequency for single ferromagnetic film ($Ni_{80}Fe_{20}$). It can be noticed in figure-(2.2) that real part of permeability ($\mu_{\perp}^{'}$) is negative in certain frequency range between ferromagnetic resonance and anti-resonance frequency for Gilbert damping constant (α) shown in figure-(2.2) [11, 12, 13, 14]. The imaginary part of permeability ($\mu_{\perp}^{''}$) is positive over the entire frequency range.

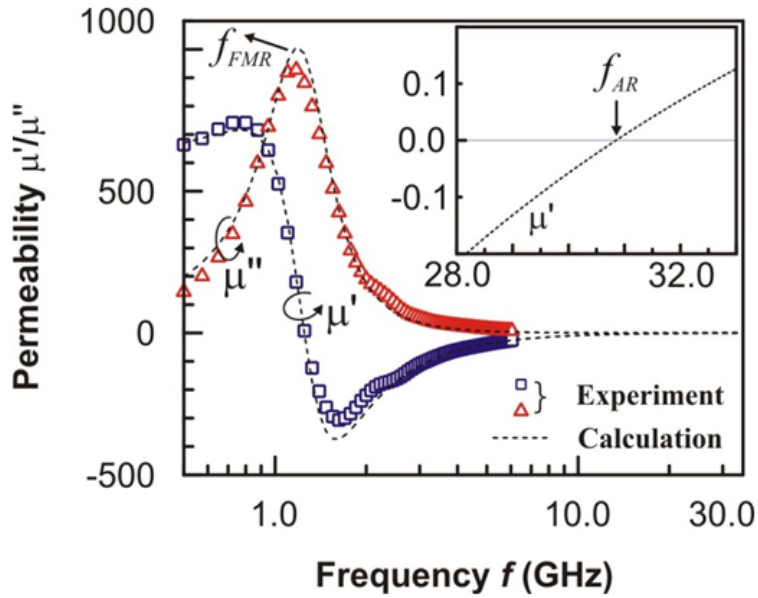

Figure 2.2: Plots of measured and simulated magnetic permeability (μ) as a function of frequency for single ferromagnetic ($Ni_{80}Fe_{20}$) film with thickness 100nm, length 4mm and width 200μm. The dashed line shows calculated permeability at $\alpha = 2.5\times10^2$.

The plot of permeability versus frequency (figure-2.2) is plotted by using microstrip structure with thickness 100nm [12, 13, 14]. The ferromagnetic film was patterned in rectangular shape with length 4mm and width 200μm. In addition, it can be noticed in figure-(2.2) that at frequency above 6GHz the permeability (i.e., real and imaginary) becomes zero [12, 13, 14, 42].

The real part of permeability in low-loss superlattice can be simulated by modeling the thickness ratio between metal (Cu) and ferromagnetic (FM) films $\left(\mu'_{\perp} = -t_{cu}/t_{NiFe}\right)$ in equation-(2.4) [12, 13, 14]. Therefore, property of ferromagnetic and anti-resonance frequency occurring in ferromagnetic film (figure-2.2) can be used for modeling the effective anti-resonance frequency (f_{EAR}) in low-loss superlattice conductor [12, 13, 14]. The effective anti-resonance frequency (f_{EAR}) in low-loss superlattice conductor depends on magnetic properties of ferromagnetic layers such as magnetic saturation (M_s) and magnetic anisotropy field (H_0). In addition, the effective anti-resonance fre-

quency (f_{EAR}) also depends on thickness ratio between copper (Cu) and ferromagnetic (NiFe) layers ($r = t_{cu}/t_{NiFe}$) [12, 13, 14].

The skin depth in low-loss superlattice (ARLYM) conductor can be increased by suppressing skin effect indicated by uniform current distribution across low-loss superlattice conductor [12, 13, 14].

2.3 Skin Depth Calculation and Current Distribution in Low-Loss Conductor

The skin depth as a function of frequency has been modeled in this section of chapter for proposed low-loss superlattice conductor and compared with reference copper conductor [12, 13, 14].

The plots of calculated skin depth for low-loss multilayer superlattice ($Ni_{80}Fe_{20}$/Cu) conductor and reference copper conductor are shown in figure-(2.3) [12, 13, 14]. The skin depth for copper conductor is plotted for comparison with low-loss multilayer superlattice structure [12, 13, 14]. The formula for skin depth calculation in low-loss superlattice conductor is listed in equation-(2.8).

$$\delta_{eff} = Re\left(\frac{1}{\sqrt{j\omega\mu_{eff}\sigma_{eff}}}\right) \tag{2.8}$$

In equation-(2.8), 'σ_{eff}' is average conductivity of low-loss conductor and 'μ_{eff}' is average permeability of multilayer superlattice given by equations-(2.9) and (2.10) [11, 12, 13, 14].

$$\sigma_{eff} = \frac{(\sigma_{NiFe}t_{NiFe} + \sigma_{Cu}t_{Cu})}{t} \tag{2.9}$$

$$\mu_{eff} = \frac{\mu_0\,(\mu_{\perp}t_{NiFe} + t_u)}{t} \tag{2.10}$$

In equations (2.9) and (2.10), 't' is total thickness of low-loss conductor given by t=t_{NiFe}+t_{Cu}. The conductivity of ferromagnetic permalloy ($Ni_{80}Fe_{20}$) and Cu

films are given by 'σ_{Cu}' and 'σ_{NiFe}' [28]. Where, '$\mu_{\perp}$' represents the permeability of ferromagnetic ($Ni_{80}Fe_{20}$) film dependent on frequency [12, 13, 14].

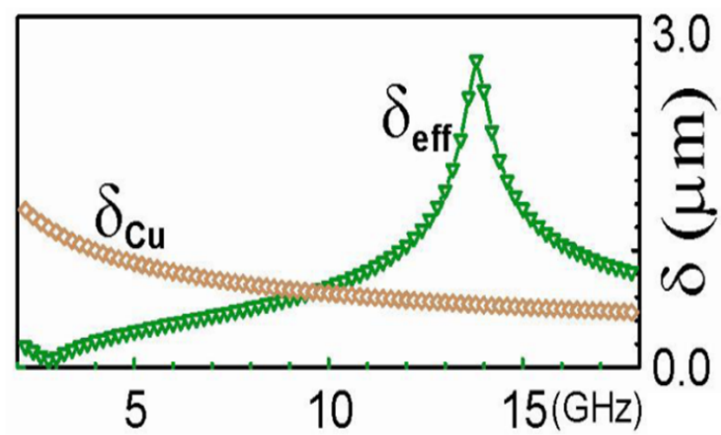

Figure 2.3: Plots of calculated effective skin depth versus frequency for low-loss (δ_{eff}) conductor and copper (δ_{Cu}) conductor.

The figure-(2.3) shows plot of calculated effective skin depth (δ_{eff}) versus frequency for low-loss conductor and reference copper (δ_{Cu}) conductor [12]. It can be noticed in figure-(2.3) that below 10GHz frequency the effective skin depth (δ_{eff}) in low-loss superlattice (green curve) is smaller than Copper (δ_{Cu}) conductor (brown curve) [12, 13, 14]. The lower skin depth in low-loss conductor is due to large effective permeability in ferromagnetic (FM) film which causes overall large permeability leading to small skin depth [12, 13, 14]. Therefore, small skin depth and large effective permeability in low-loss conductor ($\mu_{eff} < \mu_{Cu}$) is the main reason for higher conductor loss in low-loss superlattice conductor at low frequencies [12, 13, 14]. On the other hand, when frequency is increased then real part of effective permeability becomes less negative which causes the skin depth to increase [28]. It can be noticed in figure-(2.3) that at 10GHz frequency the skin depths in copper and low-loss conductor are nearly equal [12, 13, 14]. Further, as the frequency is increased to 14GHz then real part of effective permeability in low-loss conductor goes to zero leading to increased skin depth (δ_{eff}) (peak) [12, 13, 14]. The increase in skin depth for low-loss

conductor at 14GHz causes resistance to decrease due to uniform current distribution and skin effect suppression (figure-2.6) [12, 13, 14]. If frequency is increased beyond 14GHz then real part of permeability in low-loss conductor becomes positive (figure-2.2) which decreases skin depth [12, 13, 14]. Therefore, frequency at which skin effect suppression occurs depends on thickness ratio between copper (Cu) and ferromagnetic ($Ni_{80}Fe_{20}$) films in low-loss conductor [12, 13, 14].

The simulation results for current distribution across low-loss superlattice (ARLYM) conductor and reference copper (Cu) conductor are presented in figure-(2.4) [12, 13, 14]. The thickness of ferromagnetic ($Ni_{80}Fe_{20}$) layer was 100nm and thickness of copper (Cu) was 400nm. The low-loss superlattice (ARLYM) structure consisted of 16 periods ($Ni_{80}Fe_{20}$/Cu) [11]. The figure-(2.4) shows simulation results of current distribution across height of artificial layered (ARLYM) superlattice and reference copper conductors at frequencies 7, 10 and 14GHz [12, 13, 14]. It can be observed in figure-(2.4) that current in reference copper conductor is concentrated near top and bottom as shown in figure-(2.4) [12, 13, 14]. Whereas, the current distribution in low-loss conductor is dependent on frequency (d, e, f) [12, 13, 14].

At 7GHz frequency the current density in low-loss conductor is concentrated near top and bottom copper layers due to skin effect. Therefore, in figure-(2.4) at 7GHz frequency the current distribution in low-loss conductor shows non-uniformity when compared to reference copper (Cu) conductor (Figure-2.4 (a) and (d)) [12, 13, 14]. In low-loss (ARLYM) conductor the skin effect is minimized due to increased skin depth (figure-2.3) as frequency is increased which shows uniform current distribution across conductor.

At 10GHz frequency the current distribution in both low-loss conductor and reference copper are almost similar (Figure-2.4 (b) and (e)) as skin depth in low-loss superlattice is same as reference copper conductor due to skin effect suppression in low-loss conductor [12, 13, 14].

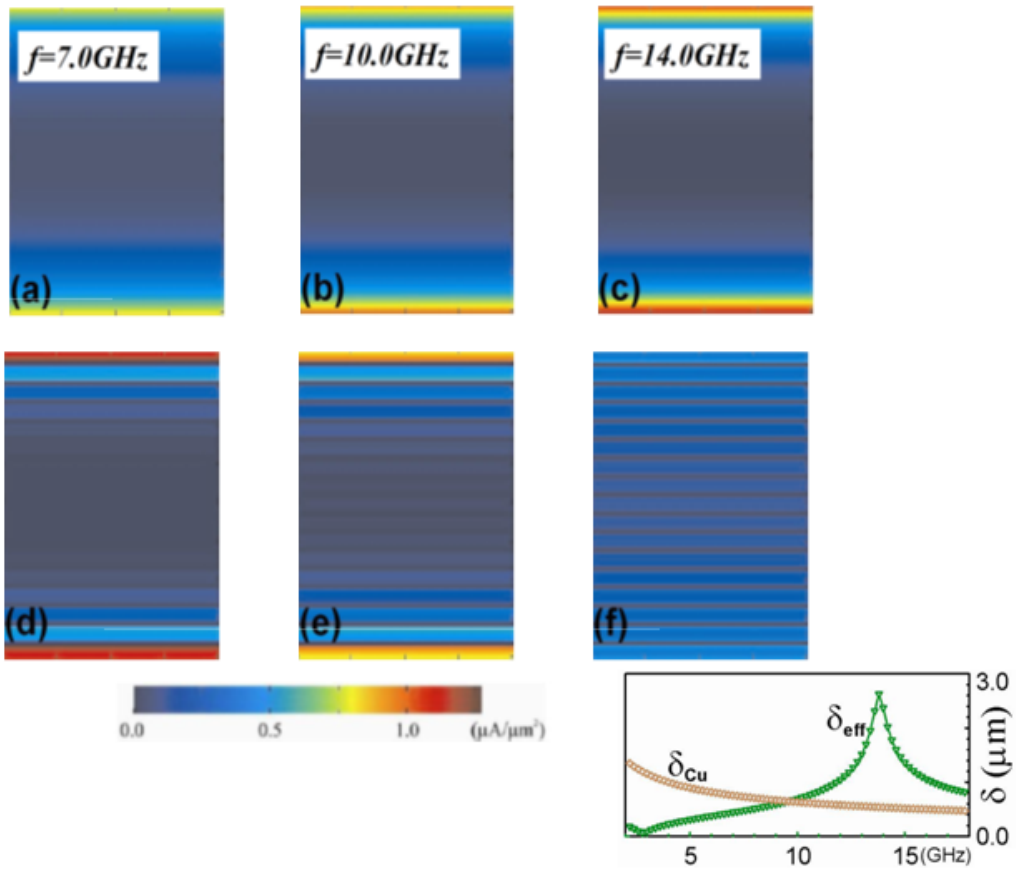

Figure 2.4: Simulation results showing current distribution across thickness of reference copper (Cu) conductor (a, b, c) and low-loss conductor (d, e, f) at 7, 10 and 14GHz frequency.

Whereas, at 14GHz, i.e., at anti-resonance frequency of ferromagnetic film the current spreads uniformly in all copper layers in low-loss superlattice structure (Figure-2.4 (f)) which indicates effective skin-effect suppression [12, 13, 14]. Therefore, overall current distribution in low-loss superlattice structure is uniform when compared to reference copper (Figure-2.4 (c)) [12, 13, 14].

2.4 Modeling and Calculation of Sheet Resistance

In order to understand the phenomenon of skin effect suppression in low-loss superlattice conductor the full wave simulations has been performed in this work by calculating the surface impedance (ζ_{surf}) of superlattice structure which is infinitely

extended in the x-y plane [42]. The sheet resistance (ρ_{sh}) is defined as the real part of surface impedance (ζ_{surf}). The surface impedance (ζ_{surf}) is calculated by considering solution of Maxwell equations in low-loss superlattice structure (figure-2.5) [11, 46].

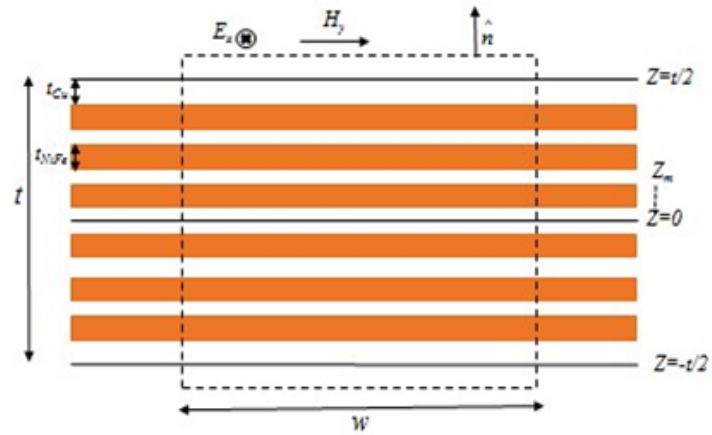

Figure 2.5: Cross-section of low-loss superlattice conductor with thickness (t). The total thickness (t) comprises of copper metal (t_{Cu}) and ferromagnetic (t_{NiFe}) layers.

The figure-(2.5) shows the cross-section of low-loss superlattice conductor having total thickness (t) and width (w). The thickness of copper and ferromagnetic layers are 't_{Cu}' and 't_{NiFe}'. The low-loss superlattice structure is considered symmetric across z-plane with respect to z=0 and 'z_m' is interface between 'm' and '$(m+1)^{th}$' layers [11, 42]. The Maxwells electromagnetic wave equations for electric and magnetic fields across low-loss superlattice structure are given by equations (2.11) and (2.12) [11].

$$\vec{E} = \hat{x}E_x(z) \tag{2.11}$$

$$\vec{H} = \hat{y}H_y(z) + \hat{z}H_z(z) \tag{2.12}$$

The above equations (2.11) and (2.12) indicate that electric field is along x-direction and direction of magnetic field is perpendicular to electric field. The unit vectors in equations (2.11) and (2.12) are given by $\hat{x}$, $\hat{y}$ and $\hat{z}$ which are along x, y and z directions [11].

The total power (P_{comp}) across low-loss superlattice structure with width (w) shown in figure-(2.5) is given by equation-(2.13) [11, 42].

$$P_{comp} = -\frac{1}{2} \oint_C \vec{E} \times \vec{H}^* \cdot \hat{n} dl \tag{2.13}$$

In above equation-(2.13), 'C' is contour and '$\hat{n}$' is unit vector normal to contour. By substituting equations (2.11) and (2.12) for total electric and magnetic fields across low-loss superlattice conductor in equation-(2.13) we obtain [11],

$$P_{comp} = -\frac{w}{2} \left(E_x H_y^* \mid_{z=t/2} - E_x H_y^* \mid_{z=-t/2} \right) \tag{2.14}$$

In equation-(2.14), 't' is total thickness of low-loss conductor [11, 42].
The surface impedance (ζ_{surf}) is calculated by equating equations (2.14) and (2.15) [11].

$$P_{comp} = \frac{1}{2} I * I Z_s \tag{2.15}$$

In equation-(2.15), 'Z_s' is surface impedance per unit length and 'I' is total current calculated using Ampere's law in equation-(2.16) [11].

$$I = \oint_C \vec{H} \cdot dl \tag{2.16}$$

$$I = \oint_C \vec{H} \cdot dl = w \left[H_y \left(-t/2 \right) - H_y \left(t/2 \right) \right] \tag{2.17}$$

The surface impedance of low-loss superlattice conductor is calculated by assuming no discontinuity in Maxwell's equations across low-loss conductor (equation-2.18) [11].

$$E_x \left(t/2 \right) = E_x \left(-t/2 \right) \tag{2.18}$$

The modeling results for sheet resistance as a function of frequency are obtained by considering vertically symmetric superlattice structure (i.e., with respect to z=0). Therefore, we obtain equations-(2.19) and (2.20) listed below [11].

$$E_x\left(-z\right) = E_x\left(z\right) \tag{2.19}$$

$$H_y\left(-z\right) = -H_y\left(z\right) \tag{2.20}$$

The equation for surface impedance (ζ_{surf}) is given by equation-(2.21) by using equations (2.14)-(2.17) [11, 46].

$$\zeta_{surf} = -\frac{1}{2}\frac{E_x}{H_y}\mid_{z=t/2} \tag{2.21}$$

The one-dimensional (1D) equations for low-loss superlattice copper layer are given by equations (2.22)-(2.25) [11].

$$\delta_z^2 E_x - \xi_{Cu}^2 E_x = 0 \tag{2.22}$$

$$H_y = -\frac{\delta_z E_x}{\left(i\omega\mu_0\mu_{Cu}\right)} \tag{2.23}$$

$$H_z = 0 \tag{2.24}$$

$$\xi_{Cu}^2 = -\omega^2\mu_0\left(\epsilon_{Cu} - i\sigma_{Cu}/\omega\right) \tag{2.25}$$

In above equations, 'σ_{Cu}' is conductivity of copper and 'ϵ_{Cu}' is dielectric constant of copper layer.

Similarly, the one-dimensional (1D) equations in low-loss superlattice conductor ferromagnetic layer are given by equations (2.26)-(2.29) [11, 12, 13, 14].

$$\delta_z^2 E_x - \xi_{NiFe}^2 E_x = 0 \tag{2.26}$$

$$H_y = -\frac{\delta_z E_x}{(i\omega\mu_0\mu_\perp)} \tag{2.27}$$

$$H_z = -\left(i\mu_a/\mu\right) H_y \tag{2.28}$$

$$\xi_{NiFe}^2 = -\omega^2\mu_0\mu_\perp\left(\epsilon_{NiFe} - i\sigma_{NiFe}/\omega\right) \tag{2.29}$$

In above equations, 'σ_{NiFe}' is conductivity of ferromagnetic layer and 'ϵ_{NiFe}' is dielectric constant of ferromagnetic film (figure-2.5) [11].

The solution for electric field (E_x) and magnetic field (H_y) inside each layer of low-loss superlattice conductor are given by equations (2.30) and (2.31) [11].

$$E_x\left(z\right) = A_m e^{(\xi_m z)} + B_m e^{(-\xi_m z)} \tag{2.30}$$

$$H_y\left(z\right) = -\frac{\xi_m}{i\omega\mu_0\mu_m}\left[A_m e^{(\xi_m z)} - B_m e^{(-\xi_m z)}\right] \tag{2.31}$$

In equations (2.30) and (2.31), 'm' is index corresponding to layer. Where, 'A_m' and 'B_m' are constants [11].

The surface impedance (ζ_{surf}) of low-loss superlattice conductor can be calculated as follows:

The calculation of surface impedance (ζ_{surf}) is considered for the upper half of z-plane i.e., ($z > 0$) due to symmetry of supperlattice structure shown in figure-(2.5) [11].

The modeling results are presented by numbering the layers in superlattice structure (figure-2.5) and impedance of each layer is calculated using equation-(2.32) [11].

$$\xi_m = -\frac{E_x\left(z_m\right)}{H_y\left(z_m\right)} \tag{2.32}$$

In equation-(2.32), 'z_m' represents interface between m^{th} and $(m+1)^{th}$ layer. The fields E_x and H_y are continuous across each interface in low-loss superlattice conductor

[11]. Therefore, by solving equations (2.30) and (2.31), we obtain,

$$\xi_m = \frac{\zeta_{m-1} + \eta_m tanh\left(\xi_m t_m\right)}{1 + \eta_m^{-1}\zeta_{m-1} tanh\left(\xi_m t_m\right)} \tag{2.33}$$

In equation-(2.33), 't_m' denotes thickness of mth layer, 'ξ_m' is surface impedance corresponding to m^{th} layer and 'η_m' is given by equation-(2.34)

$$\eta_m = \frac{i\omega\mu_0\mu_m}{\xi_m} \tag{2.34}$$

The impedances (ζ_m) at each superlattice interface (m=*1,2,3,*$\cdots$) are calculated based on equations (2.33) and (2.34) [11].

The surface impedance (ζ_{surf}) of low-loss superlattice conductor is given by equation-(2.35) [11].

$$\zeta_{surf} = \zeta_N/2 \tag{2.35}$$

In equation-(2.35), 'N' is index of top layer (z_N=t/2) [11].

The skin-effect suppression in low-loss superlattice conductor is modeled by using surface impedance equation and simulation modeling results are presented in the following section-(2.4.1) [11].

2.4.1 Skin Effect Suppression in Low-Loss Conductor

In this section (2.4.1) the simulation and modeling results for low-loss superlattice conductor are presented built using alternating layers of copper (Cu) and permalloy ($Ni_{80}Fe_{20}$) [11]. The results of low-loss (ARLYM) conductor are compared with reference copper (Cu) conductor for comparison. The thickness of copper and ferromagnetic layers in low-loss conductor are smaller than skin depth [11, 12].

The simulation results for artificial layered metamaterial superlattice (ARLYM) showed effective suppression of skin effect. In order to study the skin effect suppression

in low-loss superlattice structure the sheet resistance as a function of frequency is plotted as shown in figure-(2.6) [11]. The total thickness of low-loss superlattice conductor was considered as t= 6.7μm plotted for different number of layers 'N'. In addition, the ratio between copper and ferromagnetic layer (r) is constant [11].

The plot for reference copper conductor with same thickness (t= 6.7μm) as low-loss conductor are plotted for comparison [11, 12, 13, 14].

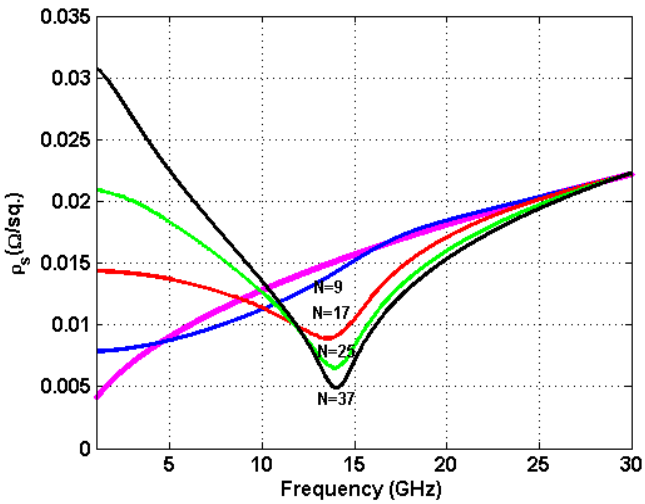

Figure 2.6: Plots of sheet resistance (ρ_s) versus frequency for low-loss superlattice conductor ($Ni_{80}Fe_{20}$/Cu) for different number of superlattice layers (N= 9, 17, 25 and 37) with constant thickness ratio (r=3). The total thickness of low-loss and copper conductors are 6.7μm.

It can be noticed in figure-(2.6) that a decrease in sheet resistance (ρ_s) is obtained at 15GHz frequency for different number of layers (N) in superlattice with same thickness ratio [11]. Since, the thickness ratio (r) was kept constant the only reason behind minimum loss at 15GHz frequency was due to average permeability (μ_{eff}) of superlattice conductor (equation-2.4) [11].

2.4.2 Modeling Anti-Magnetic Resonance Frequency

The figure-(2.7) shows the simulation result for sheet resistance versus frequency for anti-magnetic resonance frequency (f_{AR}) depending on thickness ratio 'r' [11, 12,

13, 14].

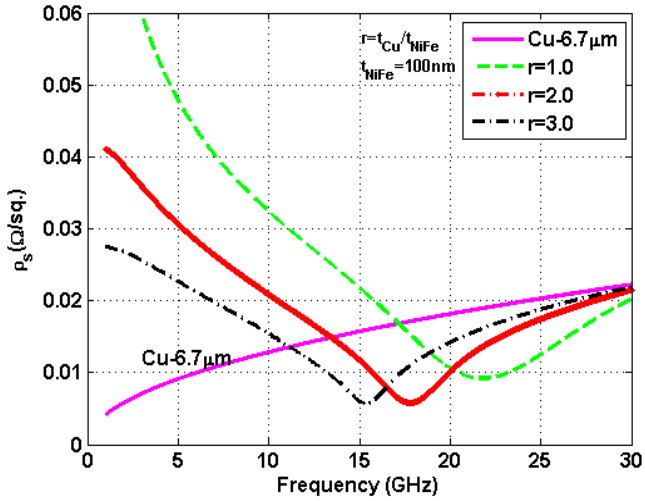

Figure 2.7: Plots of sheet resistance (ρ_s) versus frequency for superlattice (NiFe/Cu) conductor with total thickness 6.7μm and different thickness ratios (i) r=1.0, N=33 (ii) r=2.0, N=22 (iii) r=3.0, N=16. The thickness of Cu and NiFe are t_{Cu} and t_{NiFe}. 'N' is number of layers in superlattice.

It can be noticed in figure-(2.7) that low-loss is obtained at effective anti-resonance frequency (f_{EAR}) of superlattice conductor [11, 12]. In addition, the skin effect suppression in low-loss conductor is observed at a wide frequency range which can be applicable for wide bandwidth applications such as band pass filter [11, 12]. The effective anti-resonance frequency (f_{EAR}) of low-loss conductor can be modeled by changing the thickness ratio (t_{Cu}/t_{NiFe}) between copper (Cu) and the ferromagnetic (NiFe) layer.

In figure-(2.7), it can be observed that lower thickness ratio (r) causes higher anti-resonance frequency [11]. Therefore, by modeling the thickness ratio (r) the anti-resonance frequency can be modeled for suitable frequency applications [12, 13, 14]. The simulation results obtained by keeping the thickness ratio (r) constant are shown in figure-(2.8) [11, 12, 13, 14].

The applications of low-loss superlattice (ARLYM) conductor are limited for application frequency range between ferromagnetic resoance and anti-resonance frequency

where the real part of relative permeability ($\mu_\perp$) is negative ($f_{FMR} < f < f_{AR}$) [12]. Therefore, the application frequency range for low-loss conductor is depended on magnetic properties of ferromagnetic film. In general, the application frequency range for proposed low-loss (ARLYM) conductor is upto 30GHz frequency.

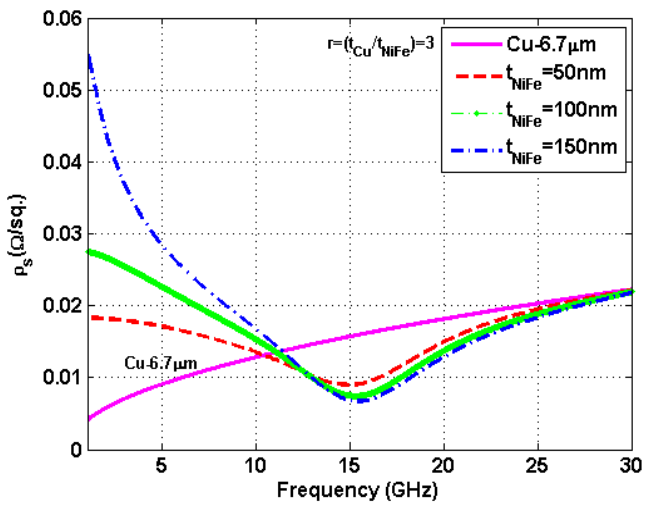

Figure 2.8: Plots of sheet resistance (ρ_s) versus frequency for low-loss superlattice (NiFe/Cu) conductor with constant thickness ratio (r=3) with varied NiFe thickness and number of layers (N) (i) t_{NiFe}=50nm, N=33 (ii) t_{NiFe}=100nm, N=16 (iii) t_{NiFe}=150nm, N=10. The total thickness of low-loss superlattice and copper conductors are 6.7μm.

In addition, simulation modeling results are performed by replacing ferromagnetic permalloy ($Ni_{80}Fe_{20}$) film with magnetic saturation value M_0=1.1T with other high saturation magnetization materials such as FeCo with magnetization M_0=2.4T.

Therefore, the anti-resonance frequency (f_{AR}) can be modeled to higher frequencies as shown in figure-(2.9) [12]. The anti-resonant frequency of 65GHz can be reached by using high magnetization materials which represents the upper frequency limit of skin-effect suppression [12, 13, 14].

The list of ferromagnetic materials with their corresponding saturation magnetization values and anti-resonance frequencies are listed in table-(2.2) [12, 13, 14].

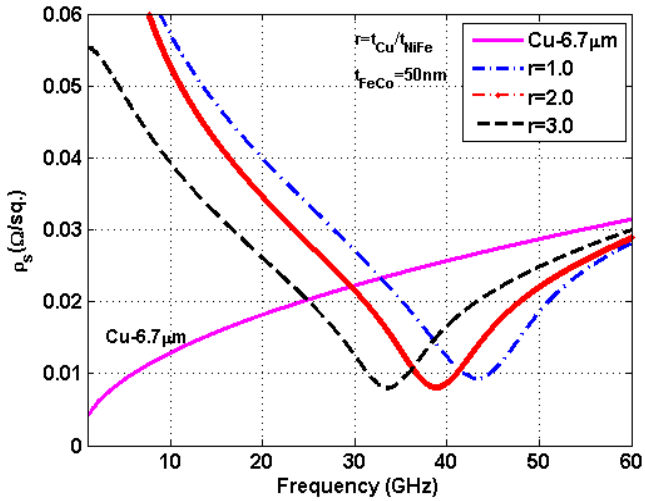

Figure 2.9: Plots of sheet resistance (ρ_s) versus frequency for low-loss superlattice (FeCo/Cu) with thickness 6.7μm. The thickness of FeCo is 50nm with varying thickness ratio and number of layers (N) (i) r=1.0, N=67 (ii) r=2.0, N=44 (iii) r=3.0, N=33.

Material	Magnetic saturation (Tesla)	Antiresonance frequency
$Ni_{80}Fe_{20}$ (Permalloy)	1.1	30
$Ni_{50}Fe_{50}$ (Deltamax)	1.6	45
$Co_{50}Fe_{50}$ (Permendur)	2.4	67
FeCoB	1.9	53
Fe	2.2	61
3% SiFe	2.0	56

Table 2.2: Anti-resonance frequency and magnetic saturation for magnetic materials.

2.5 Summary

The modeling simulation results for sheet resistance versus frequency for low-loss superlattice conductor and reference copper are illustrated in this chapter. The low-loss superlattice conductor consists of alternating layers of copper and ferromagnetic (permalloy) film. The modeling simulation results presented in this chapter showed significant skin effect suppression for low-loss (ARLYM) conductor when compared to

reference copper at r-f frequencies. The thickness of each layer in low-loss conductor was smaller than the skin depth for modeling average permeability of superlattice.

2.6 Conclusion

The high conductivity copper conductor used by semiconductor industry can be replaced by the proposed concept of low-loss (ARLYM) conductor for r-f applications. The property of negative permeability in ferromagnetic layer can be used for modeling overall (effective) permeability of low-loss superlattice structure which leads to effective skin effect suppression by increasing skin depth. Therefore, the proposed novel concept of artificial low-loss superlattice conductor can be applicable for various r-f passive components for improving device characteristics.

CHAPTER III

Experimental Results for Magnetic Multilayered Meta-Conductors

3.1 Introduction

The experimental results for integrated on-chip r-f passive components such as inductors and coplanar waveguides (CPWs) fabricated using concept of artificial layered metamaterial (ARLYM) low-loss conductor are presented in this chapter [12, 13, 14]. The structure of low-loss conductor (ARLYM) built using layers of ferromagnetic (FM) permalloy ($Ni_{80}Fe_{20}$) and copper (Cu) metal films are shown in figure-(2.1) [11, 12, 13, 14]. The average permeability of low-loss conductor is zero at anti-resonance frequency by modeling thickness of layers which leads to increased skin depth and skin effect suppression at r-f frequencies [12, 13, 14]. The increased skin depth in low-loss conductor causes uniform current distribution and skin effect suppression which leads to significant improvement in r-f device characteristics such as resistance, inductance, quality factor etc [11, 12, 13, 14].

3.2 Device Fabrication and Characterization

The sketch of low-loss conductor superlattice (ARLYM) fabricated using high conductivity metal (Cu) and thin ferromagnetic (FM) layer is shown in figure-(2.1) [12]. The fabricated low-loss superlattice ($Ni_{80}Fe_{20}$/Cu) conductor consisted of 8 periods with thikness of ferromagnetic layer (t_{NiFe}) as 50nm and thickness of copper t_{Cu} is 400nm [12, 13, 14]. The structure of low-loss superlattice (ARLYM) conductor was fabricated on top of low loss glass substrate (AF-45) to eliminate substrate loss

[12, 13, 14]. Therefore, the r-f device characteristics depended only on conductor loss fabricated using low-loss conductor ($Ni_{80}Fe_{20}$/Cu) [12, 13, 14]. The copper and ferromagnetic layers in low-loss superlattice conductor were deposited by sputtering at room temperature [12, 13, 14]. The entire fabrication procedure was performed at continuous gas flow (100 SCCM) to avoid oxidation [12, 13, 14]. The thickness of fabricated ferromagnetic ($Ni_{80}Fe_{20}$) and copper (Cu) layers is 8 inches with uniformity $\pm$ 2% [12, 13, 14]. The measured resistivity of ferromagnetic ($Ni_{80}Fe_{20}$) layer was 1.83$\mu\Omega$-cm and resistivity for copper was 16.3$\mu\Omega$-cm [12, 13, 14]. During fabrication of ferromagnetic ($Ni_{80}Fe_{20}$) layer an external magnetic (DC) field was applied to induce magnetic anisotropy [12, 13, 14]. A thin layer of benzocyclobutenes (BCB) was deposited between low-loss superlattice ($Ni_{80}Fe_{20}$/Cu) layers to minimize stress between adjacent layers [12, 13, 14]. The low-loss superlattice ($Ni_{80}Fe_{20}$/Cu) structure was depostied using wet chemical etching at room temperature. The wet-etching chemicals consists of HNO_3:CH_3COOH:H_2SO_4:H_2O in ratio of 2.5:2.6:1:8.8 [12, 13, 14]. The fabrication etching rate of low-loss (ARLYM) conductor was 300nm/min [12, 13, 14]. Therefore, cost effective low-loss superlattice (ARLYM) conductor has been fabricated in this work [12, 13, 14, 27].

3.2.1 Coplanar Waveguide Device

The structure of fabricated coplanar waveguide (CPW) device is shown in figure-(3.1) [12, 13, 14]. The design and structural parameters of fabricated coplanar waveguide (CPW) devices using artificial layered metamaterial (ARLYM) conductor are listed in table-(3.1) [12, 13, 14]. The figure-(3.1) shows the structure and design of coplanar waveguide (CPW) and surface morphology of fabricated device measured using atomic force microscopy (AFM) [12, 13, 14]. The figure shows significant undercut of 10μm due to wet-chemical etching procedure [12, 13, 14].

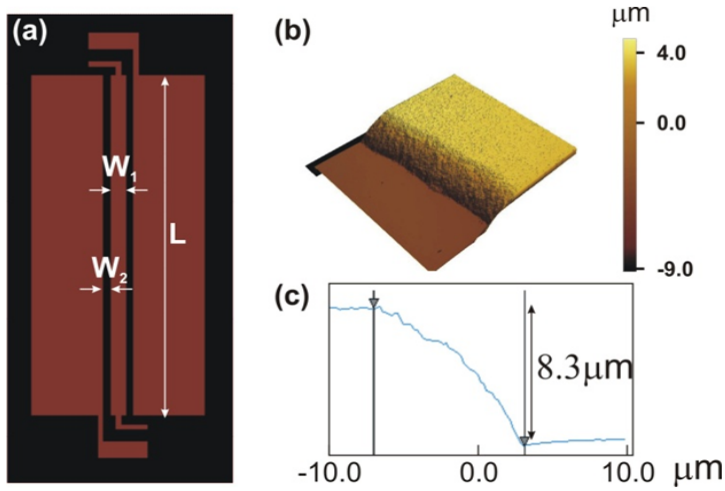

Figure 3.1: Coplanar waveguide (CPW) device (a) Structure and design in ADS, (b) Surface morphology, (c) Undercut measured using Atomic force microscopy (AFM).

Sample	**L(μm)**	**W$_1$(μm)**	**W$_2$(μm)**
#1	2000	30	20
#2	2000	30	40
#3	2000	50	30
#4	2000	50	40
#5	2000	70	20
#6	2000	70	30
#7	2000	70	40
#8	2000	90	30
#9	2000	90	40

Table 3.1: Design parameters of fabricated coplanar waveguides (CPWs) built using artificial layered metamaterial (ARLYM) low-loss conductor.

3.2.2 Inductor Device

The design of single-turn inductor fabricated using artificial layered meta-material (ARLYM) is shown in figure-(3.2) [12, 13, 14]. The single turn inductor devices were fabricated using low-loss multilayer superlattice ($Ni_{80}Fe_{20}$/Cu) and reference copper (Cu) with various structural device parameters such as width (W), length (L_E) and

spacing (W_D) listed in table-(3.2) [12, 13, 14].

The single-turn inductors were fabricated in this experimental work to eliminate additional metal layers required for building more number of turns in multiple turn inductors and also to avoid bridge connecting inner terminal to multiple turns [11, 12, 13, 14]. The fabrication procedure was simplified in this work by eliminating lithography fabrication step required for fabricating multiple turn inductors. In addition, single-turn inductors with same structural device parameters as low-loss conductor were fabricated using reference copper conductor for comparison [11, 12, 13, 14].

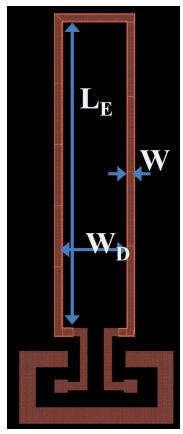

Figure 3.2: Structure of single-turn spiral inductor designed using Advanced design system (ADS).

Device	$\mathbf{W}_D$	$\mathbf{L}_E$	**W**	**Materials**
A22	300	1200	20	$Ni_{80}Fe_{20}/Cu$
A22-ref	300	1200	20	Copper

Table 3.2: Design parameters of fabricated single-turn inductors.

The structural parameters of fabricated single-turn inductors fabricated using artificial layered metamaterial (ARLYM) and reference copper are listed in table-(3.3) [12, 13, 14]. In addition, application of external DC magnetic field was eliminated in this work due to magnetic anisotropy in ferromagnetic layers of low-loss superlattice conductor [12, 13, 14]. Further, the influence of shape anisotropy in ferromagnetic (FM) films has been illustrated in this work by designing the coil line width (d) of

single-turn inductor smaller than length (L) and width (W) shown in table-(3.3) [12, 13, 14].

	L_{12}	L_{13}	L_{14}	L_{23}	L_{24}	L_{32}	L_{33}	L_{34}	L_{42}	L_{43}	L_{44}
W (μm)	300	300	300	300	300	400	400	400	200	200	200
L (μm)	600	600	600	1200	1200	800	800	800	1600	1600	600
d (μm)	20	30	40	30	40	20	30	40	20	30	40

Table 3.3: Fabricated single-turn inductors with various structural parameters width (W), length (L), and coil line width (d).

3.3 Experimental Results

3.3.1 RF Measurement Setup

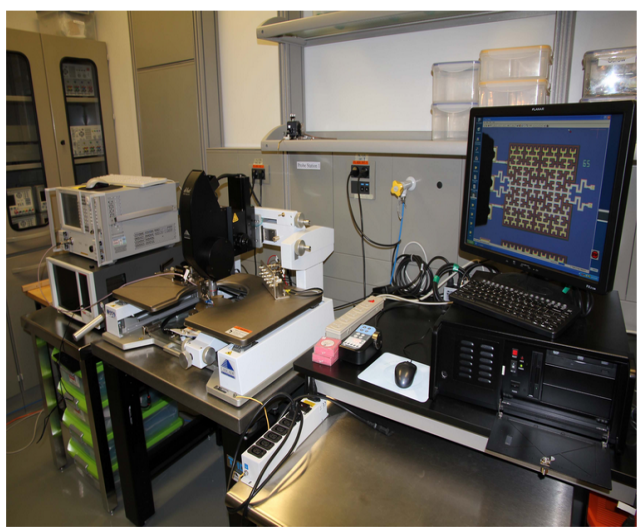

Figure 3.3: Measurement setup showing cascade r-f wafer probe station (M150), network analyzer and r-f probes connected using cables.

The experimental setup in this work consists of Cascade r-f wafer probe station (M150) and agilent network analyzer (PNA-N5230A) operating at 0.5-40GHz frequency used to measure scattering parameters (S-parameters) connected using r-f cables [12, 13, 14]. The r-f cables were used for connecting network analyzer and microprobes (Cascade ACP-40 or infinity GSG-100) as shown in figure-(3.3) [12, 13,

14]. The Cascade ACP-40 (or) infinity GSG (100) probes were used for performing ground-signal-ground (G-S-G) measurement. G-S-G probes are electrically better than Ground-Signal (GS) (or) Signal-Ground (SG) probe configuration. In addition, field lines are coupled to substrate on both sides of signal line in G-S and S-G configuration. The r-f probes were kept clean during the entire measurement procedure to avoid dust or metal particles which strongly influence the measurements by adding parasitic effects.

The measurement r-f probes were aligned and planarized using contact wafer before performing measurements. Planarizing r-f probes is very important to ensure that probes are in good contact with bond pads. The good contact was made by observing amount of skate observed on network analyzer (VNA).

The fabricated single-turn inductors and coplanar waveguide devices were characterized at Microwave research laboratory, Wright State University. The r-f impedance measurements were performed using Cascade r-f wafer probe station (M150) wafer using 2-port r-f ACP (or) infinity probes (G-S-G)(figure-3.3) [12, 13, 14]. The measured scattering parameters (S-parameters) were collected using Agilent network analyzer (PNA-L-N5230A), for frequency range 0.5-26GHz [11, 12, 13, 14]. The system was calibrated using standard short-open-load-thru (SOLT) calibration technique prior to measurements to obtain reliable measurement data [12]. An external DC magnetic field ($\sim$10mT) was applied during measurements along and perpendicular to signal to saturate ferromagnetic film [12, 13, 14]. In addition, to remove pad parasitic from measurement data a single thru de-embedding procedure was performed by measuring simple thru structure [12]. Therefore, actual impedance parameters of measured devices were obtained by subtracting pad parasitic from measured data [11, 12, 13, 14, 47, 48].

3.3.2 Materials Characterization

The magnetic hysteresis loop measurements were performed by using Princeton AGM-2900 [12, 13, 14]. The plot of measured permeability (μ) versus frequency for single ferromagnetic (FM) film is shown in figure-(3.4) [12].

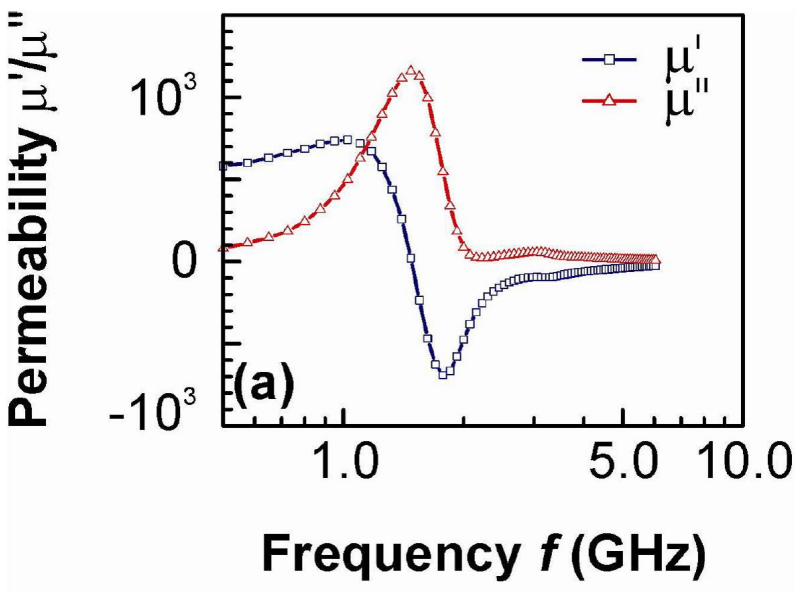

Figure 3.4: Plot of extracted magnetic permeability (μ) versus frequency for ferromagnetic permalloy ($Ni_{80}Fe_{20}$) film.

The permeability as a function of frequency was extracted using microstrip structure which consists of top signal line placed on ferromagnetic ($Ni_{80}Fe_{20}$) film on top of ground layer [12, 13, 14]. A thin dielectric layer (SiO_2) was used to separate ferromagnetic ($Ni_{80}Fe_{20}$) core from top and bottom conductors [12, 13, 14]. The scattering parameters (S-parameters) were measured using network analyzer and permeability was extracted based on quasi-TEM electromagnetic simulations [12, 13, 14]. The plot of measured permeability versus frequency (figure-3.4) shows accuracy upto 6GHz frequency and accuracy decreases at higher frequencies i.e., beyond 6GHz where both real and imaginary part of permeability are zero [12, 13, 14]. It can also be observed in figure-(3.4) that real part ($\mu^{'}$) of permeability is negative above 1GHz

frequency between ferromagnetic resonance and anti-resonance frequency [12, 13, 14, 49]. Whereas, the imaginary part (μ'') of permeability is positive over the entire frequency range [12, 13, 14].

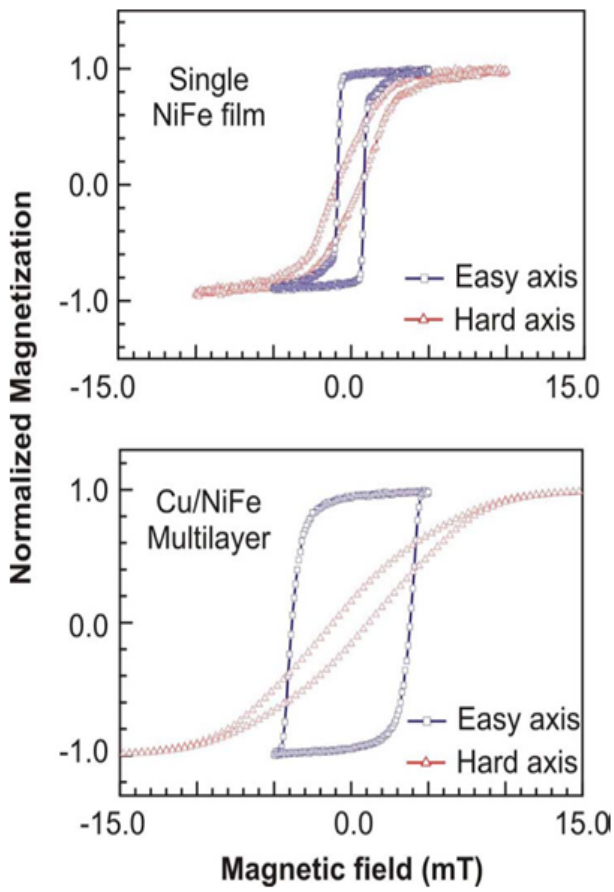

Figure 3.5: Plots of magnetic B-H loop for single ferromagnetic ($Ni_{80}Fe_{20}$) layer and low-loss multilayer superlattice (ARLYM) conductor.

The measurement results for magnetic B-H loop measurements are shown in figure-(3.5). The measurement was performed along parallel (blue curve) and perpendicular (red curve) direction of ferromagnetic (NiFe) stripe (i.e. along easy and hard axis) [11, 12, 13, 14]. The plot of measured single ferromagnetic ($Ni_{80}Fe_{20}$) layer and multilayer ($Ni_{80}Fe_{20}$/Cu) shows easy and hard axis magnetic loop [11, 12, 13, 14]. The coercivity in low-loss conductor ($Ni_{80}Fe_{20}$/Cu) was measured approximately 4-5 times higher than single ferromagnetic ($Ni_{80}Fe_{20}$) layer due to stress and strain caused

by sputtering procedure during low-loss conductor fabrication [12, 13, 14].

3.3.3 Measurement Results

3.3.4 Coplanar Waveguide Results

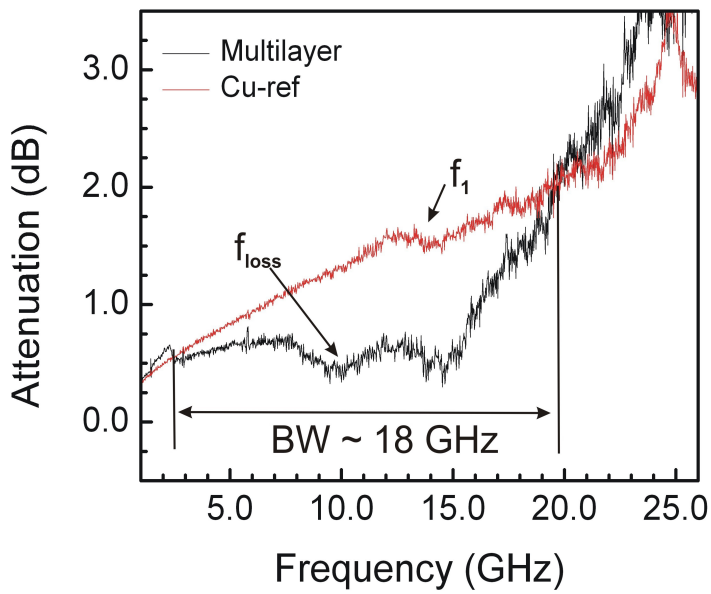

Figure 3.6: Measured attenuation per length as a function of frequency for CPW built using multilayer (#1) listed in table-(3.1) and reference copper (Cu).

The figure-(3.6) shows measured attenuation per length as function of frequency for device (#1) fabricated using multilayer low-loss conductor (black curve) listed in table-(3.1) and reference copper (red curve) [12, 13, 14]. The 'f_{Loss}' indicated in figure-(3.6) is frequency when the attenuation constant (α) is at frequency 'f_1' [12, 13, 14]. The figure-(3.7) shows the propagation wavelength as a function of frequency for multilayer (#1) device (table-3.1) and reference copper [11, 12, 13, 14]. It can be noticed in figure-(3.7) that propagation wavelength for multilayer (device #1) and reference copper are almost similar. In figure-(3.6), it can be noticed that loss in multilayer (black curve) coplanar waveguide (CPW) device shows decrease in attenuation between certain frequency range (2-20GHz) [11, 12, 13, 14]. On other hand for cop-

per conductor (red curve) the loss increases continuously with frequency (figure-3.6) [14]. The effective anti-resonance frequency for low-loss multilayer (ABMC) conductor is approximately around 10GHz frequency where average permeability of low-loss multilayer (ABMC) conductor becomes zero which causes skin-effect suppression and reduction in conductor losses [12, 13, 14].

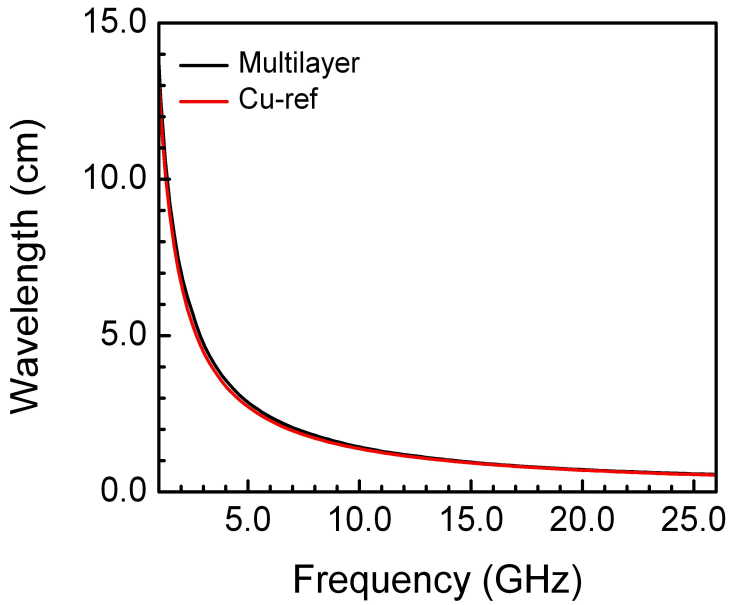

Figure 3.7: Propagation wavelength as a function of frequency for coplanar waveguide (CPW) built using multilayer low-loss superlattice (#1) listed in table-(3.1) and reference copper (Cu).

The second drop in attenuation curve shown in figure-(3.6) for low-loss (ABMC) conductor is around 15GHz frequency [12, 13, 14]. The second dip observed at 15GHz frequency is not observed in theoretical modeling results [14]. However, theoretical calculation and modeling results for full wave electromagnetic (EM) simulations presented in previous chapter (chapter-2) showed a single broad dip [12, 13, 14]. In addition, a drop near 15GHz frequency for reference copper device is observed in figure-(3.6) which explains the similar cause for both low-loss conductor device and reference copper device [12, 13, 14]. In order to further investigate the effects of the observed phenomenon a number of coplanar waveguide devices with various structural

parameters were measured (table-3.1) [12, 13, 14].

The measurement data for low-loss (ABMC) conductor devices and reference copper devices showed the similar phenomenon (i.e., drop in attenuation) at 15GHz frequency as shown in figure-(3.6) [12, 13, 14]. The main reason behind drop in attenuation observed for both multilayer low-loss conductor and reference copper devices was discontinuity due to tip-to-pad and pad-to-device [12, 13, 14, 47, 48, 50, 51, 52, 53].

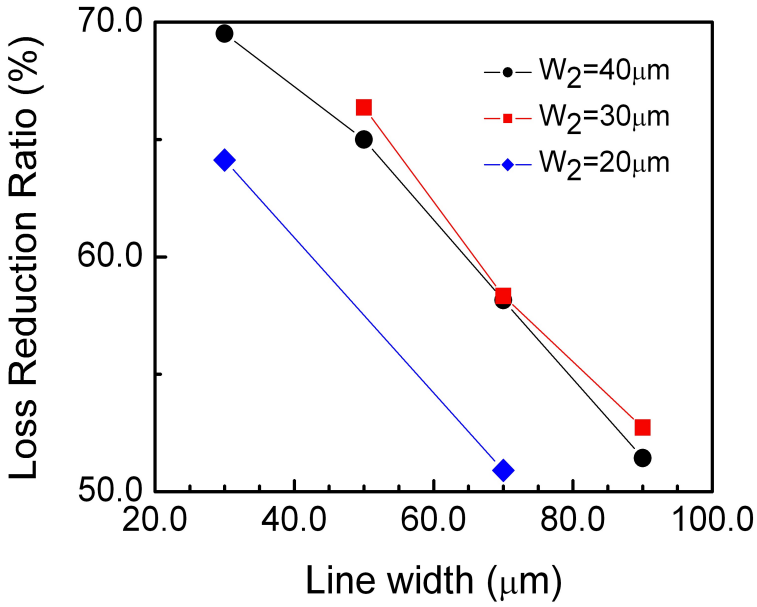

Figure 3.8: Loss reduction ratio (η) versus signal line width for coplanar waveguide (CPW) devices listed in table-(3.1).

The figure-(3.8) shows loss reduction ratio (η) versus signal line width for multilayer (ABMC) coplanar waveguide (CPW) devices listed in table-(3.1) at frequency 'f_{Loss}' shown in figure-(3.6) [12, 13, 14]. The loss reduction of 70% at 10GHz frequency without changing propagation wavelength has been obtained in this work [14]. In addition, it can be noticed in figure-(3.8) that as line width (W_2) increases the demagnetizing field in direction perpendicular to signal line of coplanar waveguide (CPW) becomes weak [14]. Therefore, weak demagnetizing field causes distortion of

magnetic moment alignment from easy axis [12, 13, 14]. In addition, problems related to etching during multilayer low-loss conductor fabrication caused fabricated line width to decrease when compared to the designed value which affected lower loss reduction value [12, 13, 14]. Otherwise, a significant increment in loss reduction value (>70%) for coplanar waveguides fabricated using multilayer low-loss (ABMC) conductor would be obtained similar to simulation results [14]. Therefore, loss reduction of 70% has been obtained in this work by using low-loss multilayer conductor at 10GHz frequency [12, 13, 14].

3.3.5 Single-turn Inductor Results

The measurement results for impedance versus frequency for single-turn inductors fabricated using artificial layered metamaterial (ARLYM) superlattice low-loss conductor and reference copper (table-3.2) are shown in figures (3.9)-(3.11) [12].

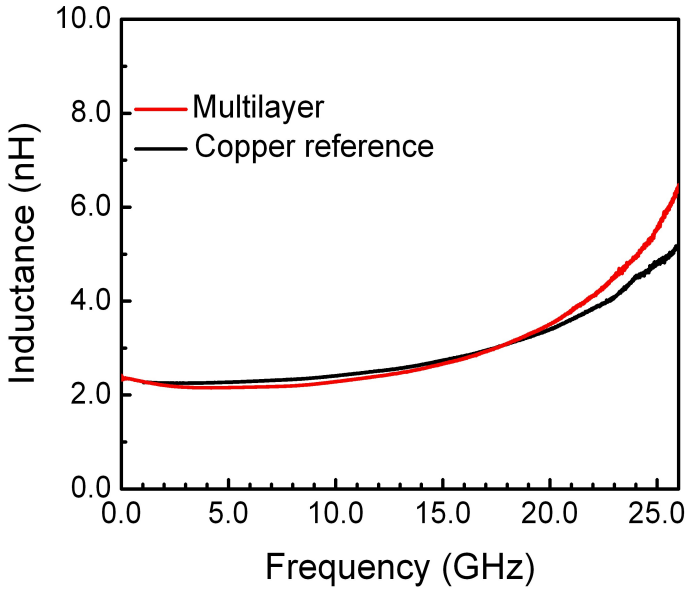

Figure 3.9: Plots of measured inductance (L) as a function of frequency for fabricated single-turn inductors.

The plot of inductance versus frequency for fabricated single-turn inductor such as multilayer (A22-ref) and reference copper (A22) are shown in figure-(3.9). In figure-(3.9), it can be noticed that inductance versus frequency for single-turn inductors fabricated using low-loss conductor (red curve) and reference copper (black curve) are almost similar [12, 13, 14]. In addition, above 18GHz frequency the inductance curve for multilayer (A22) superlattice (red curve) is higher than reference (A22-ref) copper (black curve) due to LC resonance phenomenon [12, 13, 14].

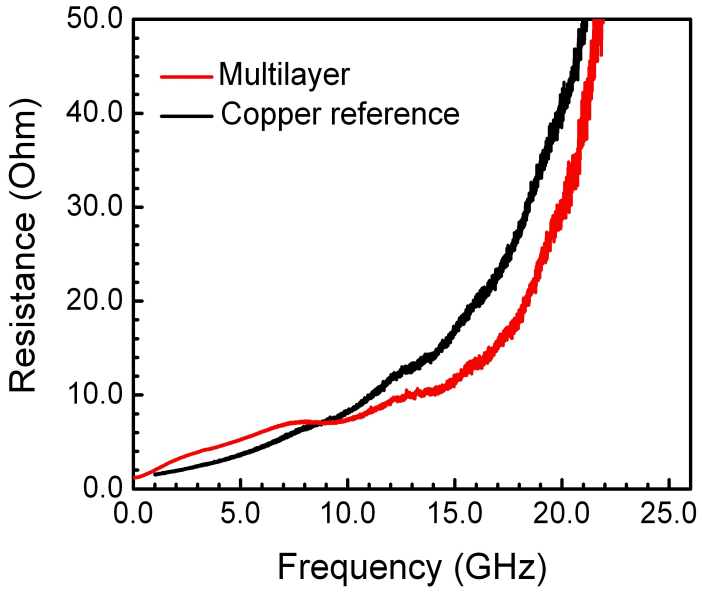

Figure 3.10: Plots of measured resistance (R) as a function of frequency for single-turn inductors.

The plot of measured resistance as a function of frequency for single turn spiral inductors fabricated using artificial layered metamaterial (ARLYM) superlattice A22 (red curve) and reference copper A22-ref (black curve) are shown in figure-(3.10) [12]. In general, the resistance curve increases continuously with frequency as shown in figure-(3.10) for pure copper A22-ref (black curve) [12, 13, 14]. The resistance (red curve) for single turn inductor made of multilayer superlattice (ARLYM) shows a decrease in resistance in certain (10-18GHz) frequency range [12]. The slope of re-

sistance curve for multilayer superlattice single-turn inductor is less when compared to reference copper ref-A22 (black curve) [12, 13, 14]. The single-turn inductor devices fabricated using low-loss multilayer (A22) and reference copper (ref-A22) are placed on low-loss glass substrate (AF-45) to remove substrate losses [12]. Therefore, skin effect suppression is the only main cause behind the decrease in resistance for multilayer single-turn inductor [12, 13, 14].

The skin effect is suppressed when effective permeability of low-loss superlattice structure becomes zero which resulted in constant inductance as a function of frequency (figure-3.9) and decrease in resistance (figure-3.10) [12, 13, 14]. The slower increase in resistance slope for low-loss conductor (red curve) in figure-(3.10) caused increased quality factor as function of frequency as shown in figure-(3.11) [12, 13, 14].

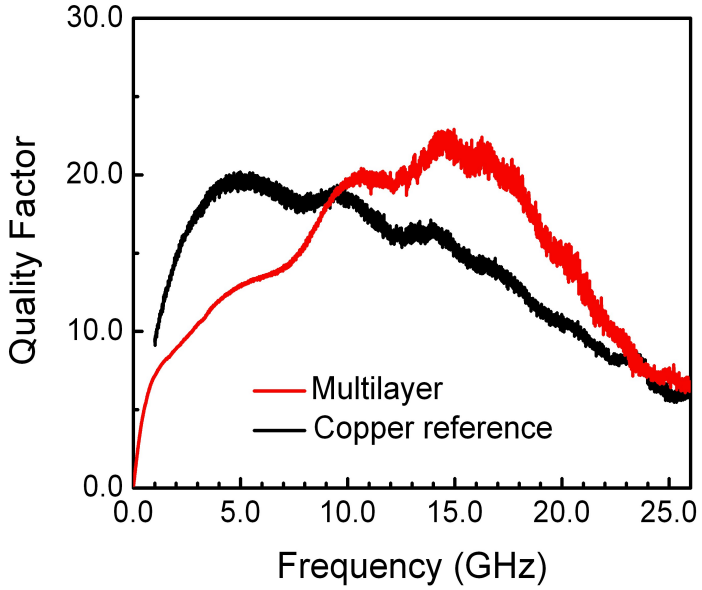

Figure 3.11: Plots of measured quality factor (Q) as a function of frequency for fabricated single-turn inductors.

In figure-(3.11), it can be observed that quality factor of low-loss multilayer device (A22) is higher than reference copper (A22-ref) [12]. The maximum quality factor

measured for single-turn inductor built using low-loss multilayer (A22) superlattice is around 23 [12]. At 14.5GHz frequency the resistance for multilayer device (A22) was minimum (30%) as shown in figure-(3.10) which lead to maximum quality factor (41%) [12, 13, 14]. The measured resistance for multilayer (ARLYM) single-turn inductor below 7GHz frequency was higher than simulated device with similar configuration [12, 13, 14]. Therefore, at low frequencies the low-loss (ARLYM) superlattice showed high magnetic permeability which caused high eddy currents in multilayer (ARLYM) inductor when compared to reference copper device [12, 13, 14].

In addition, above 18GHz frequency the phenomenon of LC resonance dominated the resistance and quality factor [12]. Therefore, bandwidth of skin effect suppression for low-loss multilayer (ARLYM) device is 7-18GHz frequency range [12, 13, 14].

The figure-(3.12) shows relative quality factor versus inductance for fabricated single-turn inductor devices listed in table-(3.3) for frequencies 10GHz, 12.5GHz and 15GHz [12, 13]. The frequencies 10GHz and 15GHz are chosen close to quality factor (Q) peak (figure-3.11) and 12.5GHz frequency is chosen near resistance plateau (figure-3.10) [12, 13, 14]. Therefore, increase in quality factor of 85% has been achieved for inductor (L_{13}) listed in table-(3.3) at 15GHz frequency when compared to reference copper inductor [12, 13]. In this experimental work even high quality factor would be obtained if problems due to fabrication etching were eliminated [54].

The fabrication etching caused 10μm undercut as shown in figure-(3.1) which affected measured quality factor (Q). Therefore, substrate coupling and loss can be reduced in this work by using 10μm insulating (SiO_2) layer between silicon and metal layers [12, 13, 14]. In addition, concept of using low-loss conductor for single-turn inductors can be extended to multiple turn inductors for improving r-f device characteristics in future experiments [12, 13, 14].

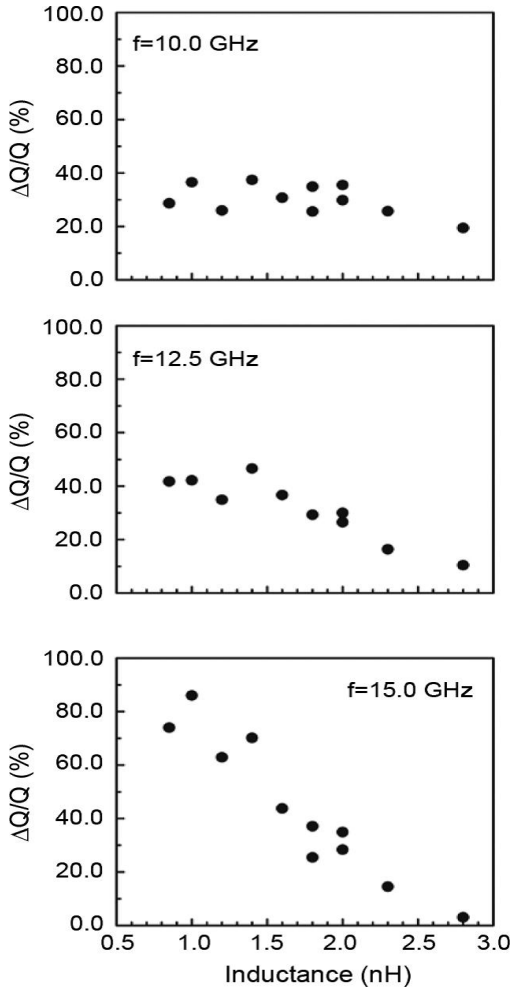

Figure 3.12: Relative quality factor versus inductance at different frequencies (a) 10GHz (b) 12.5GHz (c) 15GHz for fabricated single-turn inductors.

3.4 Summary

The experimental results for integrated on-chip inductors and coplanar waveguides (CPWs) fabricated using artificial low-loss conductor are demonstrated in this chapter [12, 13, 14]. The quality factor improvement of approximately 40% percent for single-turn inductor (2-nH) at 14.5GHz frequency has been obtained when compared to the reference copper device [12, 13, 14]. The bandwidth of skin-effect suppression obtained in this work is between 10-18GHz frequency range [12, 13]. In addition, loss reduction of 70% has been achieved using multilayer low-loss conductor based coplanar wave guide (CPW) device at 10GHz frequency [14]. Therefore, an overall

increase of 85% quality factor for single-turn inductors has been achieved in this work when compared the reference copper devices operating at microwave frequencies.

3.5 Conclusion

The proposed concept of low-loss (ARLYM) conductor superlattice for r-f components showed significant decrease in ohmic loss and increase in device characteristics such as quality factor (>30) at 15GHz frequency [12, 13, 14]. Therefore, newly developed novel concept of low-loss conductor in this work can be implemented to solve current issues in r-f (or) semiconductor industry and provides new path for advancement in high speed electronics causing numerous breakthroughs in semiconductor industry for various r-f components such as inductors, transformers, transmission lines, coplanar waveguides etc, [12]. Additionally, low-loss conductor concept can be applicable for improving clock frequency, system speed, power etc, in microprocessor and r-f integrated circuits [12].

CHAPTER IV

Theoretical Study of Magneto-Dynamics in Thin Ferromagnetic Films

The theoretical analysis and simulation results of r-f single-turn solenoid inductors built using thin ferromagnetic film are presented in this chapter. The impedance of single-turn inductor is calculated by using magneto-static approximation of Green's function [42]. The impedance characteristics such as inductance and resistance as a function of frequency are calculated by using magneto-static modes of the core [42]. The susceptibility matrix depended on demagnetization factors related to magnetic modes [42]. Therefore, demagnetization factors and magnetic resonance modes in magnetic core are demonstrated in form of magnetic resonance peaks shown in simulation and experimental results [42]. Additionally, the modeling results obtained by varying device parameters such as width and magnetic loss on impedance characteristics of single-turn inductor are analyzed in this work [42].

4.1 Introduction

The r-f passive components such as inductors, transmission lines, coplanar waveguides (CPWs) etc, form basic building blocks in r-f integrated circuits such as r-f matching networks, filters, low-noise amplifiers (LNAs) etc [42, 55]. The r-f integrated devices can be scaled by utilizing thin ferromagnetic films with high permeability.

The various r-f inductor devices such as spiral type inductors [30, 31, 56], sandwiched stripe [42, 28] and solenoid type inductors [42, 57, 58] has been studied by various researchers for scaling r-f components size built using thin magnetic films [42]. Among all types of inductor devices the sandwiched stripe and planar solenoid induc-

tors provides more advantages by utilizing thin magnetic films due to application of external magnetic (d-c) field [42, 54]. The theoretical simulations and experimental results are presented in this chapter for single-turn solenoid inductors utilizing thin magnetic core [42].

The derived r-f susceptibility of thin magnetic film has been used for theoretical simulations and experimental analysis [42]. In general, r-f susceptibility for non-ellipsoidal sample with uniform magnetic field can be determined by averaging demagnetization factors [42, 59, 60, 61, 62, 63]. However, this method cannot be applicable to scaled magnetic components due to non-uniform current generated by magnetic coil [42]. The effects of magneto-static excitation in inductor core on electrical characteristics such as resistance and inductance versus frequency cannot be measured in case of non-uniform magnetic field [42, 64, 65, 66]. In this work, a new concept has been proposed based on theoretical calculations and modeling results which provided high frequency r-f impedance of single-turn solenoid inductor [42]. The results of theoretical simulations and experimental analysis for single-turn inductors presented in this chapter were performed using thin magnetic film approximation and Greens function [42, 57, 58, 67]. Therefore, high frequency (or) r-f impedance characteristics related to magnetic core of inductor are described using magneto-static eigen modes [42]. The magnetic response in single-turn inductor corresponding to each magnetic mode is determined based on susceptibility matrix [42]. The magneto-static excitation in inductor core are illustrated in form of magnetic resonances shown in theoretical and experimental results [42]. In addition, effect of varying device parameters such as width and magnetic loss of single-turn inductor are also presented in this chapter [42].

4.2 RF susceptibility in thin ferromagnetic film

The figure-(4.1) shows structure of single-turn solenoid inductor consisting thin magnetic coil [42]. The coil is separated from inductor core by dielectric layers [42]. It can be observed in figure-(4.1) bottom that length (l) of solenoid inductor is along z-axis and width (w) is along x-axis [42].

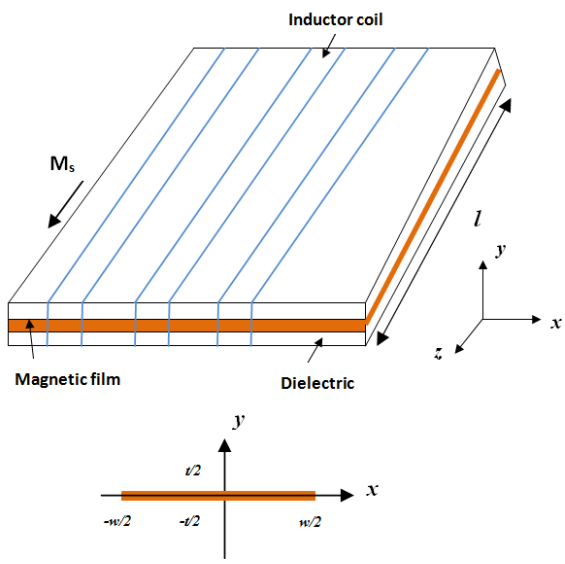

Figure 4.1: Solenoid inductor built using thin ferromagnetic film and magnetic coil separated by dielectric layers (top). The cross-section of thin ferromagnetic stripe across x-y plane (bottom).

The magnetic stripe is saturated along z-axis with magnetization field ($M_s\hat{z}$) by applying external magnetic (d-c) field ($H_o\hat{z}$) along z-direction [42]. The r-f current flowing in inductor coil winding is generated due to time harmonic r-f field (i.e., external field) [42]. In simulation modeling the length of single-turn inductor is along z-axis which is assumed greater than width along x-axis ($l >> w$). By utilizing small signal condition assumption the magnitude of r-f magnetization field ($\vec{m}$) is much smaller than saturation magnetization field (M_s) ($\vec{m} << M_s$) [42]. In addition, longitudinal component of r-f magnetization vector has been neglected ($\vec{m} = m_x\hat{x} + m_y\hat{y}$) since, $m_z = 0$ [10, 24, 42, 65].

The effect of magnetization in ferromagnetic thin stripe is calculated using Greens function [10, 24, 42, 67, 68]. The r-f magnetization vector ($\vec{m}$) and applied r-f field ($\vec{h}$) are given by expression (equation-4.1) [10, 42].

$$\vec{m} = \check{\chi} \cdot \vec{h} \tag{4.1}$$

In equation-(4.1), '$\check{\chi}$' is susceptibility tensor derived in Appendix-(A) given by (A.21) [10, 42]. Where, '$\vec{h}$' is applied total (r-f) magnetic field [42].

$$\check{\chi} = \frac{\omega_M}{\left(\omega_H^2 - \omega^2\right)} \begin{bmatrix} \omega_H & j\omega \\ -j\omega & \omega_H \end{bmatrix}$$

The magneto-static approximation of Maxwell's equation can be derived as follows [10, 24, 42]. The total magnetic (r-f) field is given by equation-(4.2) [42].

$$\vec{h} = \vec{h_e} + \vec{h_m} \tag{4.2}$$

In equation-(4.2), the external (r-f) magnetic field is given by $\vec{h_e} = h_{e,x}\hat{x} + h_{e,y}\hat{y}$ and demagnetization field is '$\vec{h_m}$' [42].

In order to derive magneto-static approximation the a-c form of Maxwells equation (Amperes law) is considered (equation-4.3) [10, 24]

$$\bigtriangledown \times \vec{h} = \vec{j} + \frac{\partial \vec{d}}{\partial t} \tag{4.3}$$

In static case, the quantities which are function of time can be neglected in the Maxwell's equation i.e., $\left(\frac{\partial}{\partial t} = 0\right)$ [10].

In addition, ferromagnetic film is considered as non-conductive (i.e. the current density $\vec{j} = 0$). Therefore, a-c form of Maxwells equation (equation-4.3) is given by

equation-(4.4) known as magneto-static Maxwells equation [42].

$$\bigtriangledown \times \vec{h} = 0 \tag{4.4}$$

Stoke's Theorem: The line integral of vector '$\vec{h}$' along a closed contour 'C' is equal to integral of dot product of curl of vector ($\vec{h}$) normal to the surface 'S' which has contour 'C' as its boundary [42, 69].

The Stokes theorem is given by equation-(4.5) [42, 69]

$$\oint_C \vec{h} \cdot d\vec{l} = \iint_S \left(\bigtriangledown \times \vec{h} \right) \cdot d\vec{S} \tag{4.5}$$

By using magneto-static form of Maxwell's equation (equation-4.4) in Stoke's theorem (equation-4.5) we obtain (equation-4.6) [10, 24, 69].

$$\oint_C \vec{h} \cdot d\vec{l} = 0 \tag{4.6}$$

The solution of equation-(4.6) is given by [10, 24]

$$\vec{h} = - \bigtriangledown \phi_m \tag{4.7}$$

In equation-(4.7), '$\bigtriangledown \phi_m$' is gradient of magnetic potential.

In magneto-statics there are no magnetic monopoles [10]. Therefore, the magnetic induction ($\vec{b}$) is given by Gauss Law (i.e., no fundamental source charge) [10]. Consider Maxwell's equation (equation-4.8) [10, 24]

$$\vec{\bigtriangledown} \cdot \vec{b} = 0 \tag{4.8}$$

$$\vec{b} = \vec{\mu} \left(\vec{h} + \vec{m} \right) \tag{4.9}$$

By multiplying '$\bigtriangledown$' on both sides of equation-(4.9) we obtain (equation-4.10) [10, 24],

$$\bigtriangledown \cdot \vec{b} = \bigtriangledown \cdot \vec{\mu} \left(\vec{h} + \vec{m} \right) \tag{4.10}$$

By using magnetic Gauss Law (equation-4.8) in above relation (equation-4.10) we obtain [10],

$$\bigtriangledown \cdot \breve{\mu} \left(\vec{h} + \vec{m} \right) = 0$$

Where, '$\breve{\mu}$' is permeability tensor.

The permeability tensor derived in Appendix-(A) is given by [10, 24]

$$\breve{\mu} = \begin{bmatrix} \mu_{xx} & \mu_{xy} & 0 \\ \mu_{yx} & \mu_{yy} & 0 \\ 0 & 0 & 0 \end{bmatrix}$$

$$\breve{\mu} \bigtriangledown \cdot \left(\vec{h} + \vec{m} \right) = 0 \tag{4.11}$$

The equation for divergence-free ($\vec{b}$) can be obtained by rearranging equation-(4.11) as follows [10].

$$\left(\bigtriangledown \cdot \vec{h} \right) = - \left(\bigtriangledown \cdot \vec{m} \right) \tag{4.12}$$

The magnetic field ($\vec{h}$) generated by effective magnetic charge density is given by (equation-4.13) [10, 24]

$$\rho_m = - \bigtriangledown \cdot \vec{m} \tag{4.13}$$

When there are no free currents ($\vec{j} = 0$), the magnetic field can be calculated using magnetic potential as shown in equation-(4.14) [10, 24]

$$\vec{h} = - \bigtriangledown \phi_m \tag{4.14}$$

By substituting equation-(4.14) in (equation-4.12) the Poisson's equation is given by (equation-4.16) [10, 24].

$$\bigtriangledown \cdot (- \bigtriangledown \phi_m) = - (\bigtriangledown \cdot \vec{m})$$

$$\bigtriangledown^2 \phi_m = - \bigtriangledown \cdot \vec{m} = \rho_m \tag{4.15}$$

$$\bigtriangledown^2 \phi_m = \rho_m \tag{4.16}$$

In equation-(4.16), 'ρ_m' is total magnetic volume charge density and 'ϕ_m' is scalar magnetic potential.

The general solution of magneto-static Poisson's equation is given by [10, 24, 70]

$$\phi_m (\vec{r}) = \int_{S'} \bigtriangledown' G \left(\vec{r}, \vec{r'}\right) \cdot \vec{m} \left(\vec{r'}\right) dS' \tag{4.17}$$

In equation-(4.17), $\vec{r} = (x, y)$ is location of observation point, $\vec{r'} = \left(x', y'\right)$ is location of point source, $\bigtriangledown = (\partial_x, \partial_y)$ is gradient at observation point and $\bigtriangledown' = \left(\partial_{x'}, \partial_{y'}\right)$ is gradient of point source [42, 70].

By using equation-(4.14) in equation-(4.17) we obtain [10, 42, 70],

$$\vec{h_m} (\vec{r}) = - \bigtriangledown \int_{S'} \bigtriangledown' G \left(\vec{r}, \vec{r'}\right) \cdot \vec{m} \left(\vec{r'}\right) dS' \tag{4.18}$$

In equation-(4.18), $G\left(r, r'\right)$ is Greens function given by $G\left(r, r'\right) = -\frac{1}{2\pi} ln \left|r - r'\right|$ [42].

The free space scalar Green's function in equation-(4.18) for two dimensional (2-D) and three dimensional (3-D) can be derived from one of the following cases listed in Appendix-(C) [70].

In single-turn inductors fabricated using thin ferromagnetic film the spatial variation of r-f magnetic field generated by inductor magnetic core and induced magnetization can be neglected [42]. Therefore, the field quantities can be replaced by averaging over thickness of ferromagnetic film [42]. The r-f magnetization vector $\vec{m} (\vec{r})$

is averaged by thickness 't' to obtain '$\tilde{m}(x)$' listed in equation-(4.19) [42, 70]

$$\vec{m}(\vec{r}) \rightarrow \tilde{m}(x) = \frac{1}{t} \int_{-t/2}^{t/2} \vec{m}(\vec{r})\, dy \tag{4.19}$$

Similarly, the external (r-f) magnetic field $\vec{h_e}(\vec{r})$ and demagnetization field $\vec{h_m}(\vec{r})$ can be replaced by '$\tilde{h_e}(x)$' and '$\tilde{h_m}(x)$' by averaging over thickness (t) of ferromagnetic film as shown in equations-(4.20) and (4.21) [42].

$$\vec{h_e}(\vec{r}) \rightarrow \tilde{h_e}(x) = \frac{1}{t} \int_{-t/2}^{t/2} \vec{h_e}(\vec{r})\, dy \tag{4.20}$$

$$\vec{h_m}(\vec{r}) \rightarrow \tilde{h_m}(x) = \frac{1}{t} \int_{-t/2}^{t/2} \vec{h_m}(\vec{r})\, dy \tag{4.21}$$

The total magnetic field ($\vec{h}$) is given by equation-(4.2). The external (r-f) magnetic field $\vec{h_e}(\vec{r})$ can be calculated by subtracting demagnetization field from total magnetic field $\vec{h}(\vec{r})$ as shown in equation-(4.22) [70].

$$\vec{h_e}(\vec{r}) = \vec{h}(\vec{r}) - \vec{h_m}(\vec{r}) \tag{4.22}$$

By averaging equation-(4.22) on both sides with respect to thickness (t) of thin ferromagnetic film we obtain equation-(4.23) [70],

$$\frac{1}{t} \int_{-t/2}^{t/2} \vec{h_e}(\vec{r})\, dy = \frac{1}{t} \int_{-t/2}^{t/2} \vec{h}(\vec{r})\, dy - \frac{1}{t} \int_{-t/2}^{t/2} \vec{h_m}(\vec{r})\, dy \tag{4.23}$$

By using equations-(4.20) & (4.21) in equation-(4.23) we obtain, [42]

$$\tilde{h_e}(x) = \tilde{h}(x) - \frac{1}{t}\int_{-t/2}^{t/2} \vec{h_m}(\vec{r})\, dy \tag{4.24}$$

The total magnetic field averaged over thickness ($\tilde{h}(x)$) can be calculated using relation in equation-(4.1) as follows [42]

$$\vec{m}(\vec{r}) = \check{\chi} \cdot \vec{h}(\vec{r}) \tag{4.25}$$

By averaging equation-(4.25) over thickness (t) of ferromagnetic film on both sides we obtain [42],

$$\tfrac{1}{t}\int_{-t/2}^{t/2} \vec{m}(\vec{r})\, dy = \check{\chi} \cdot \tfrac{1}{t}\int_{-t/2}^{t/2} \vec{h}(\vec{r})\, dy$$

$$\tilde{m}(x) = \check{\chi} \cdot \tilde{h}(x)$$

$$\tilde{h}(x) = \tfrac{\tilde{m}(x)}{\check{\chi}}$$

$$\tilde{h}(x) = \check{T} \cdot \tilde{m}(x) \tag{4.26}$$

Where,

$$\check{T} = \tfrac{1}{\check{\chi}}$$

By using susceptibility tensor ($\check{\chi}$) in above expression we obtain [42],

$$\check{T} = \frac{1}{\frac{\omega_M}{\left(\omega_H^2 - \omega^2\right)}\begin{bmatrix} \omega_H & j\omega \\ -j\omega & \omega_H \end{bmatrix}}$$

$$\check{T} = \frac{\left(\omega_H^2 - \omega^2\right)}{\omega_M} * \frac{1}{\left(\omega_H^2 - \omega^2\right)}\begin{bmatrix} \omega_H & -j\omega \\ j\omega & \omega_H \end{bmatrix}$$

$$\check{T} = \frac{1}{\omega_M} \begin{bmatrix} \omega_H & -j\omega \\ j\omega & \omega_H \end{bmatrix} \tag{4.27}$$

By using equation-(4.26) in equation-(4.24) we obtain,

$$\tilde{h_e}(x) = \check{T} \cdot \tilde{m}(x) - \frac{1}{t} \int_{-t/2}^{t/2} \vec{h_m}(\vec{r})\, dy \tag{4.28}$$

The demagnetization field $\vec{h_m}(\vec{r})$ from equation-(4.18) is given by

$$\vec{h_m}(\vec{r}) = - \bigtriangledown \int_{S'} \bigtriangledown' G\left(\vec{r}, \vec{r'}\right) \cdot \vec{m}\left(\vec{r'}\right) dS'$$

Where, $\vec{r} = (x, y)$, $\bigtriangledown = (\partial_x, \partial_y)$, $\bigtriangledown' = \left(\partial_{x'}, \partial_{y'}\right)$ and S' is cross-section of thin ferromagnetic film [42].

By substituting equation-(4.18) in equation-(4.28) we obtain [42]

$$\tilde{h_e}(x) = \check{T} \cdot \tilde{m}(x) + \check{\Sigma}_3 \int_{-w/2}^{w/2} \check{G}\left(x, x'\right) \cdot \tilde{m}\left(x'\right) dx' \tag{4.29}$$

In equation-(4.29), $\check{G}\left(x, x'\right)$ is Green's function given by [42]

$$\check{G}\left(x, x'\right) = \tfrac{1}{t} \int_{-t/2}^{t/2} \int_{-t/2}^{t/2} \tfrac{\partial}{\partial y} \tfrac{\partial}{\partial y'} G\left(\vec{r}, \vec{r'}\right) dy dy'$$

The 2-Dimensional (2D) free-space Greens function derived in appendix-(C) is given by [42, 70]

$$G\left(\vec{r}, \vec{r'}\right) = -\tfrac{1}{2\pi} ln \left|\vec{r} - \vec{r'}\right|$$

Where, $\vec{r} = (x, y)$ and $\vec{r'} = \left(x', y'\right)$

Therefore, we obtain [42],

$$G\left(x, x'\right) = -\frac{1}{2\pi t} ln \left(\frac{\left(x - x'\right)^2}{\left(x - x'\right)^2 + t^2} \right) \tag{4.30}$$

The r-f susceptibility of thin ferromagnetic film is obtained by solving equation-(4.29) for external magnetic field $\tilde{h}_e\left(x^{'}\right)$ [42, 71, 72]. The r-f susceptibility of magnetic film in terms of magneto-static modes can be calculated using equation-(4.31) [42, 71, 72, 73].

$$\int_{-w/2}^{w/2} G\left(x, x^{'}\right) \psi_q\left(x^{'}\right) dx^{'} = \lambda_q \psi_q\left(x\right) \tag{4.31}$$

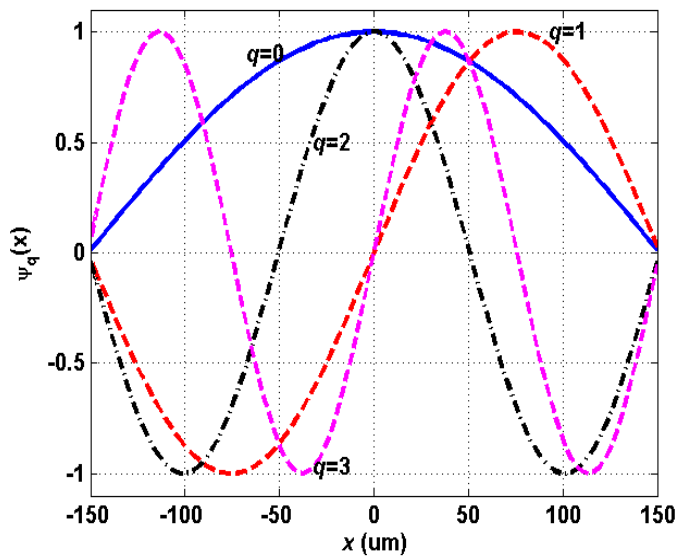

Figure 4.2: Plots of eigen functions $\psi_k\left(x\right)$ for different modes across width (300μm) and thickness (0.3μm) of thin ferromagnetic film.

The figure-(4.2) shows the plots of eigenmodes $\psi_q\left(x^{'}\right)$ for thin ferromagnetic film having width 300μm and thickness 0.3μm [42]. The eigen modes are obtained by numerically solving equation-(4.31) [42]. The function $\psi_q\left(x^{'}\right)$ in equation-(4.31) is either even or odd function of 'x' for even or odd values of integer 'q' [42, 71, 72, 73]. The numerically calculated eigen values for first four modes are $\lambda_0 = -0.9976$, $\lambda_1 = -0.9944$, $\lambda_2 = -0.9913$ and $\lambda_3 = -0.9881$ [42].

The solution of equation-(4.29) is obtained by solving magnetization in terms of

eigen modes of thin magnetic stripe [42, 71, 72, 73],

$$\tilde{m}\left(x\right)=\sum_{q=0}^{\infty}\tilde{m}^{q}\psi_{q}\left(x\right) \tag{4.32}$$

$$\tilde{m}^{q}=\int_{-w/2}^{w/2}\tilde{m}\left(x\right)\psi_{q}\left(x\right) \tag{4.33}$$

In equation-(4.33), '$\tilde{m}^{q}$' is constant vector. By substituting equations (4.32) and (4.33) in equation-(4.29) we obtain [42],

$$\tilde{h_{e}}\left(x\right)=\frac{1}{\omega_{M}}\begin{bmatrix}\omega_{H}+\omega_{M} & -j\omega\\ j\omega & \omega_{H}\end{bmatrix}\cdot\sum_{q=0}^{\infty}\tilde{m}^{q}\psi_{q}\left(x\right)+\begin{bmatrix}1 & 0\\ 0 & -1\end{bmatrix}\cdot\int_{-w/2}^{w/2}\check{G}\left(x,x'\right)\cdot\tilde{m}\left(x'\right)dx'$$

Where,

$$\check{T}=\frac{1}{\omega_{M}}\begin{bmatrix}\omega_{H} & -j\omega\\ j\omega & \omega_{H}\end{bmatrix}$$

$$\check{\Sigma}=\begin{bmatrix}1 & 0\\ 0 & -1\end{bmatrix}$$

By using equation-(4.31) in above expression we obtain,

$$\tilde{m}^{q}=\begin{bmatrix}\frac{\omega_{H}+\omega_{M}}{\omega_{M}}+\lambda_{q} & \frac{-j\omega}{\omega_{M}}\\ \frac{j\omega}{\omega_{M}} & \frac{\omega_{H}}{\omega_{M}}-\lambda_{q}\end{bmatrix}^{-1}\cdot\tilde{h_{e}}^{q}$$

$$\tilde{m}^{q}=\check{\chi}^{q}\cdot\tilde{h_{e}}^{q} \tag{4.34}$$

The mode dependent susceptibility matrix is given by [42],

$$\check{\chi}^{q}=\begin{bmatrix}\frac{\omega_{H}+\omega_{M}}{\omega_{M}}+\lambda_{q} & \frac{-j\omega}{\omega_{M}}\\ \frac{j\omega}{\omega_{M}} & \frac{\omega_{H}}{\omega_{M}}-\lambda_{q}\end{bmatrix}^{-1}$$

The amplitude of magnetic field in q^{th} mode is '$\tilde{h_{e}}^{q}$' [42].

The mode-dependent susceptibility matrix '$\check{\chi}^{q}$' is given by [42]

$$\check{\chi}^q = \begin{bmatrix} \frac{\omega_H+\omega_M}{\omega_M} + \lambda_q & \frac{-j\omega}{\omega_M} \\ \frac{j\omega}{\omega_M} & \frac{\omega_H}{\omega_M} - \lambda_q \end{bmatrix}^{-1} = \begin{bmatrix} \chi^q_{xx} & j\chi^q_a \\ -j\chi^q_a & \chi^q_{yy} \end{bmatrix}$$

By using $N^q_x = (1+\lambda_q)$ and $N^q_y = -\lambda_q$ we obtain,

$$\check{\chi}^q = \frac{\omega_M}{\omega_q^2 - \omega^2} \begin{bmatrix} \omega_H + N^q_y & j\omega \\ -j\omega & \omega_H + N^q_x \omega_M \end{bmatrix} \tag{4.35}$$

In equation-(4.35), 'ω_q' is magneto-static resonance frequency (equation-4.36) [42].

$$\omega_q^2 = (\omega_H + N^q_x \omega_M)\left(\omega_H + N^q_y \omega_M\right) \tag{4.36}$$

The effect of magnetic loss is considered in the modeling results by using $\omega_H \rightarrow \omega_H - i\alpha\omega$ in equations-(4.35) and (4.36) [42]. Where, 'α' is Gilbert damping factor [10, 42].

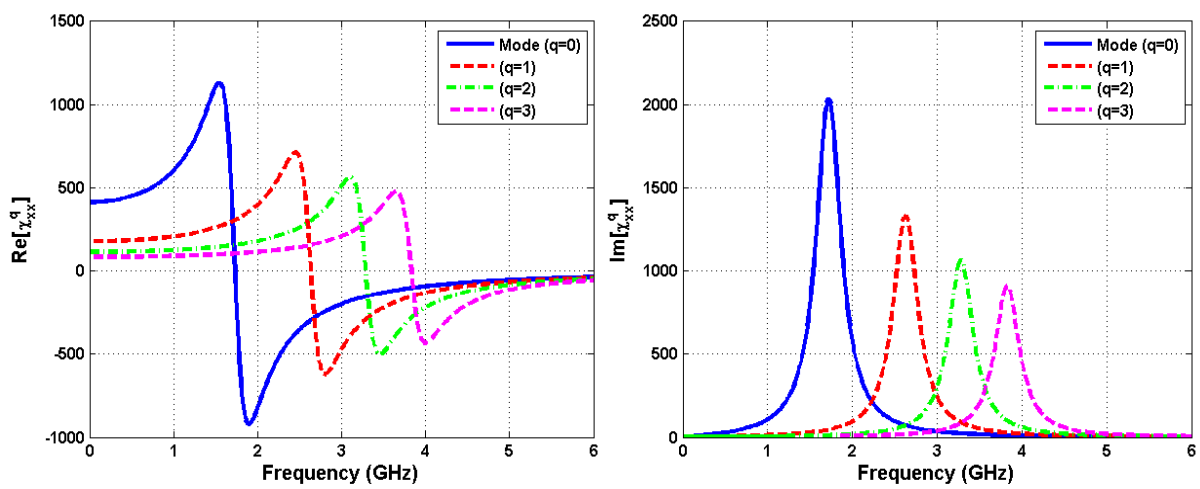

Figure 4.3: Real and imaginary part of susceptibility (χ^q_{xx}) versus frequency for thin ferromagnetic film for four eigen modes. The width and thickness of ferromagnetic stripe are $300\mu m$ and $0.3\mu m$

The figure-(4.3) shows plot of susceptibility (χ^q_{xx}) versus frequency for different modes (q=0,1,2,3) of thin ferromagnetic film with width (300μm) and thickness

(0.3μm) [42]. The magnetic properties of ferromagnetic film are M_s=1T, H_a=200Oe and α=0.01 [42, 74]. In figure-(4.3), each mode $\mathrm{Im}[\chi^q_{xx}]$ peaks at $\omega = \omega_q$, i.e., magneto-static resonance frequency [42, 74]. It can be observed in figure-(4.3) that modes with large demagnetizing factors ($N^q_x = 1 + \lambda_q$) have higher magneto-static resonance frequency [42].

4.3 Impedance of single-turn inductor utilizing thin ferromagnetic core

The impedance of single-turn solenoid inductor can be calculated by considering the effect of current generated by external magnetic field ($\vec{h_e}$) [42].

The total power delivered to single-turn inductor is given by equation-(4.37) [42],

$$P = \frac{i\omega l}{2} \int \vec{h}\left(\vec{r}\right) \cdot \vec{b}^*\left(\vec{r}\right) d\vec{S} \tag{4.37}$$

In equation-(4.37), 'l' is length of single-turn inductor and magnetic induction is given by '$\vec{b} = \mu_0 \left(\vec{h} + \vec{m}\right)$' [42]. By integrating equation-(4.37) across x-y plane the impedance of single-turn inductor is given by (equation-4.38) [42].

$$Z = \frac{2P}{|I_t^2|} + R_s \tag{4.38}$$

In equation-(4.38), 'I_t' is total current and 'R_s' is series resistance of single-turn inductor [42].

By substituting total magnetic field ($\vec{h} = \vec{h_e} + \vec{h_m}$) from equation-(4.2) and expression for magnetic induction $\vec{b} = \mu_0 \left(\vec{h} + \vec{m}\right)$ in equation-(4.37) we obtain [42, 75],

$$P = \frac{i\omega l}{2} \int \left(\vec{h_e}\left(\vec{r}\right) + \vec{h_m}\left(\vec{r}\right)\right) \bullet \mu_0 \left(\vec{h}\left(\vec{r}\right) + \vec{m}\left(\vec{r}\right)\right)^* d\vec{S} \tag{4.39}$$

By expanding equation-(4.39) and considering $\int_V \vec{h_m}\left(\vec{r}\right) \bullet \left(\vec{h}\left(\vec{r}\right) + \vec{m}\left(\vec{r}\right)\right) dV$.

Where, $\vec{h_m}(\vec{r}) = -\bigtriangledown \phi_m$

Therefore, we obtain,

$$\int_V \bigtriangledown\phi_m \bullet \left(\vec{h}(\vec{r}) + \vec{m}(\vec{r})\right) dV = \int_V \bigtriangledown\phi_m \bullet \left(\vec{h}(\vec{r}) + \vec{m}(\vec{r})\right) dS + \int_V \phi_m \bigtriangledown \bullet \left(\vec{h}(\vec{r}) + \vec{m}(\vec{r})\right) dV$$

By using Divergence theorem in above expression we obtain,

$$\int_V h_m \bullet \left(\vec{h}(\vec{r}) + \vec{m}(\vec{r})\right) dV = \int_S \bigtriangledown\phi_m \bullet \left(\vec{h}(\vec{r}) + \vec{m}(\vec{r})\right) dS + \int_V \phi_m \bigtriangledown \bullet \vec{b}(\vec{r})\, dV$$

Therefore, magnetic Gauss law is given by

$$\bigtriangledown \bullet \vec{b}(\vec{r}) = \bigtriangledown \bullet \left(\vec{h}(\vec{r}) + \vec{m}(\vec{r})\right) = 0$$

The second integral and first integral on right-hand side of above expression are zero because the r-f magnetic induction $\left(\vec{h}(\vec{r}) + \vec{m}(\vec{r})\right)$ must be parallel to coupling conductors which defines the surface 'S' [42].

Therefore, we obtain equation-(4.40)

$$\int_V h_m \bullet \left(\vec{h}(\vec{r}) + \vec{m}(\vec{r})\right) dV = 0 \tag{4.40}$$

By integrating equation-(4.40) along length (l) of single-turn inductor (z-axis) we obtain

$$\int_0^l dz \int_S h_m \bullet \left(\vec{h}(\vec{r}) + \vec{m}(\vec{r})\right) dxdy = 0$$

$$\int_S h_m \bullet \left(\vec{h}(\vec{r}) + \vec{m}(\vec{r})\right) dS = 0 \tag{4.41}$$

By using equation-(4.41) we obtain,

$$P = \frac{i\omega l \mu_0}{2} \int \left(\left|\vec{h_e}(\vec{r})\right|^2 + \vec{h_e}(\vec{r}) \bullet \vec{m}^*(\vec{r})\right) d\vec{S} + \frac{i\omega l \mu_0}{2} \int \left(\vec{h_e}(\vec{r}) \bullet \vec{h_m}^*(\vec{r})\right) d\vec{S} \tag{4.42}$$

By considering expression $\int_V \left(\vec{h_e}(\vec{r}) \bullet \vec{h_m}(\vec{r})\right) dV$ and $\vec{h_m}(\vec{r}) = -\bigtriangledown \phi_m$ we obtain

$$-\int_V \bigtriangledown\phi_m \bullet \vec{h_e}(\vec{r})\, dV = -\int_S \phi_m \bullet \vec{h_e}(\vec{r})\, dS$$

By considering that r-f magnetic inductor is parallel to conductors which define the surface 'S' we obtain [42].

$$\int_V \left(\vec{h_e}\left(\vec{r}\right) \bullet \vec{h_m}\left(\vec{r}\right)\right) dV = 0 \tag{4.43}$$

By integrating equation-(4.43) along length (l) of single-turn inductor we obtain,

$$\int_0^l dz \int_S \left(\vec{h_e}\left(\vec{r}\right) \bullet \vec{h_m}\left(\vec{r}\right)\right) dxdy = 0$$

$$\int_S \left(\vec{h_e}\left(\vec{r}\right) \bullet \vec{h_m}\left(\vec{r}\right)\right) dS = 0 \tag{4.44}$$

By substituting above expression (equation-4.44) in equation-(4.42) we get,

$$P = \frac{i\omega l}{2}\left[\int\left(\left|\vec{h_e}\left(\vec{r}\right)\right|^2 dS + \int_S \vec{h_e}\left(\vec{r}\right) \bullet \vec{m}\left(\vec{r}\right)^*\right) d\vec{S}\right] \tag{4.45}$$

By using equation-(4.45) in equation-(4.38) the impedance of single-turn solenoid inductor (Z) is given by equation-(4.46)

$$Z = \frac{i\omega\mu_0 l\left[\int\left(\left|\vec{h_e}\left(\vec{r}\right)\right|^2 dS + \int_S \vec{h_e}\left(\vec{r}\right) \bullet \vec{m}\left(\vec{r}\right)^*\right) d\vec{S}\right]}{|I_t^2|} + R_s \tag{4.46}$$

$$Z = R_s + Z_0 + Z_m$$

Where,

$$Z_0 = \frac{i\omega\mu_0 l}{|I_t^2|}\int\left|\vec{h_e}\left(\vec{r}\right)\right|^2 dS \tag{4.47}$$

$$Z_m = \frac{i\omega\mu_0 l}{|I_t^2|}\int \vec{h_e}\left(\vec{r}\right) \bullet \vec{m}^*\left(\vec{r}\right) dS \tag{4.48}$$

The impedance of single-turn inductor without ferromagnetic core is given by $Z = R_s + Z_0$ [42]. Where, impedance corresponding to ferromagnetic film is given by 'Z_m' [42].

The expressions for average field are given by equations-(4.19), (4.20) and (4.21). By substituting equation-(4.32) in equation-(4.48) we obtain,

$$Z_m = \frac{i\omega\mu_0 l}{|I_t^2|} \int_{-w/2}^{w/2} \sum_{q=0}^{\infty} \tilde{h_e^q} \psi_q(x) \bullet \tilde{m}^*(x)$$

$$Z_m = \frac{i\omega\mu_0 l}{|I_t^2|} \tilde{h_e^q} \bullet \tilde{m^q}^* \tag{4.49}$$

Since, $Z_m = \sum_{q=0}^{\infty} Z_q$ and using equation-(4.34) in equation-(4.49) we obtain

$$Z_q = \frac{i\omega\mu_0 tl}{|I_t^2|} \tilde{h_e^q} \bullet \left(\check{\chi}^q \bullet \tilde{h_e}^q\right)^* \tag{4.50}$$

The impedance of magnetic core (Z_m) is sum of partial difference (Z_q) which depends on amplitude ($\tilde{h_e}^q$) of external magnetic field and susceptibility matrix ($\check{\chi}^q$) in magneto-static modes [42].

By neglecting the propagation of electromagnetic waves in equation-(4.50) and assuming that 'x' and 'y' components of external magnetic field have same phase [42]. The non-diagonal elements of '$\check{\chi}^q$' are eliminated from 'Z_q' [42].

$$Z_q = \frac{i\omega\mu_0 tl}{|I_t|^2} \tilde{h_e^q} \bullet \left(\begin{bmatrix} \chi_{xx}^q & 0 \\ 0 & \chi_{yy}^q \end{bmatrix} \bullet \tilde{h_e}^q \right)^*$$

$$Z_q = \frac{i\omega\mu_0 tl}{|I_t|^2} \left(\chi_{xx}^q \left| \tilde{h_{e,x}}^q \right|^2 + \chi_{yy}^q \left| \tilde{h_{e,y}^q} \right|^2 \right) \tag{4.51}$$

Where, components $\tilde{h_{e,x}}^q$ and $\tilde{h_{e,y}}^q$ in above equation-(4.51) are 'x' and 'y' components of amplitude $\tilde{h_e}^q$ [42].

4.4 Simulation Results

The impedance of single-turn inductor versus frequency depends on magnetic field induced by ferromagnetic coil which depends on ferromagnetic resonance modes of inductor core [42]. The impedance of single-turn solenoid inductor can be calculated by using the derived equations-(4.47), (4.48) and (4.51) [42]. The magneto-static eigen

values and eigen functions are calculated by numerically solving equation-(4.31) [42]. The numerical calculations of single-turn inductor are performed by assuming that dielectric layers separating the coil have same thickness [42]. In addition, by considering that cross-section of single-turn inductor structure is with respect to y=0 plane, and electrical current is flowing in opposite directions in top and bottom conductors [42]. The average vertical component of external magnetic field are eliminated (i.e., $\tilde{h_{e,y}} = 0$) [42]. Therefore, only $\tilde{h_{e,x}}$ contributes to impedance 'Z_q' in equation-(4.51) [42].

$$Z_q = \frac{i\omega\mu_0 tl}{|I_t|^2}\left(\chi^q_{xx}\left|\tilde{h^q_{e,x}}\right|^2\right) \tag{4.52}$$

The plots of resistance ($R = Re\,[Z]$) and inductance ($L = \frac{Im[Z]}{\omega}$) as a function of frequency for single-turn solenoid inductor are shown in figure-(4.4) [42].

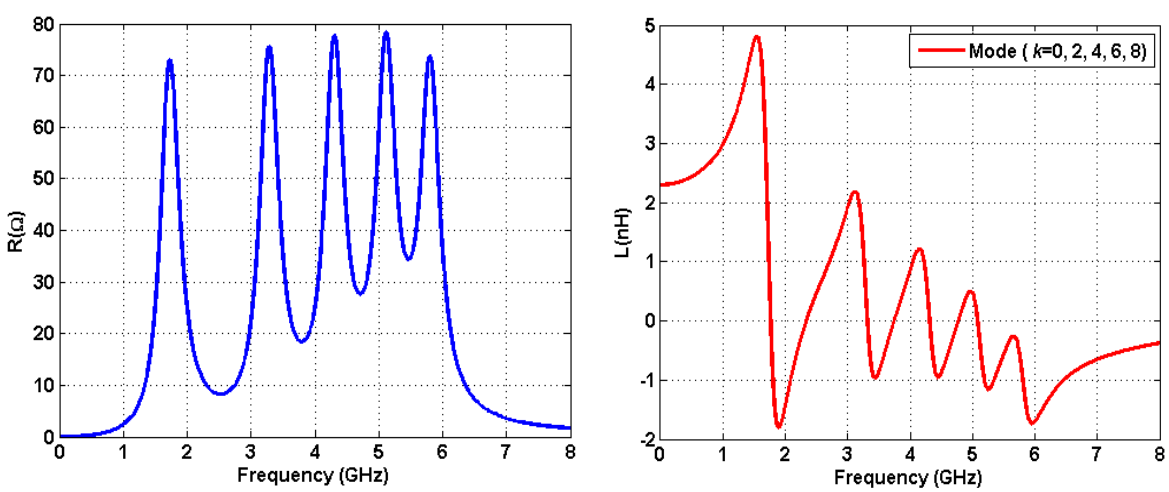

Figure 4.4: Plots of resistance (R) and inductance (L) versus frequency for single-turn inductor with length 1mm. The thin ferromagnetic film inductor core with width $300\mu m$ and thickness $0.3\mu m$.

In figure-(4.4), it can be noticed that only even resonance modes of thin ferromagnetic film are observed because the single-turn inductor coil is placed around the center of the stripe (i.e., x=0) [42]. Therefore, '$\tilde{h_{e,x}}$' is even function with respect to 'x' [42]. The odd-resonance modes can be observed by turning the coil at center of

the ferromagnetic stripe [42, 59, 60, 61].

The simulation results for inductance and resistance as a function of frequency for single-turn inductor obtained by increasing width (w) of ferromagnetic film are shown in figure-(4.5) [42].

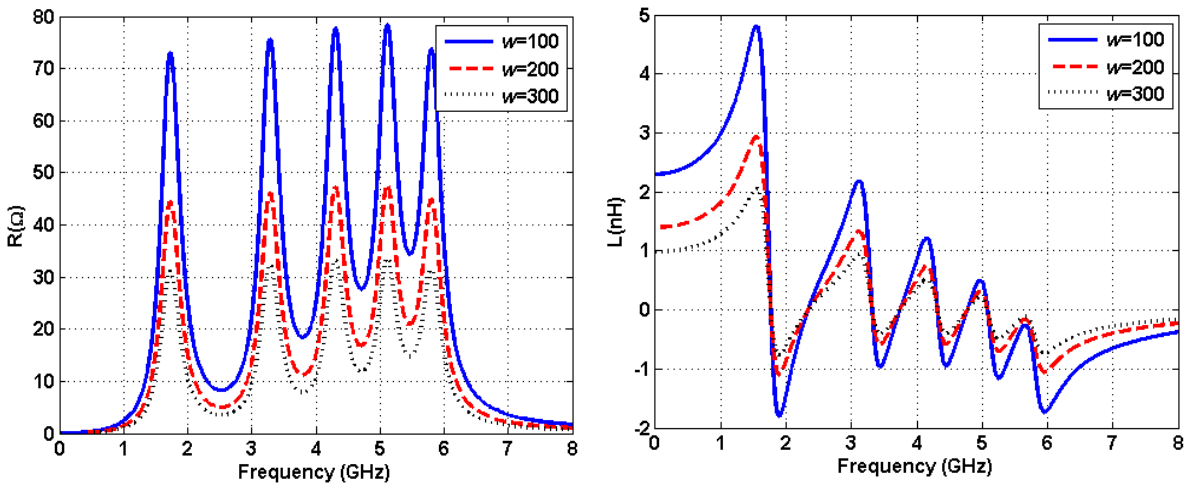

Figure 4.5: Plots of resistance (R) and inductance (L) versus frequency for single-turn inductor with length 1mm and various ferromagnetic film widths.

In figure-(4.5), it can be noticed that increasing width (w) caused the eigenvalues (λ_q) to reduce which reduced the gap between the adjacent eigenvalues [42].

The figure-(4.6) shows the plots of impedance of single-turn solenoid inductor for variations of magnetic loss in inductor core or damping constant (α) [42]. It can be noticed in figure-(4.6) that large damping constant (α) causes wide resonance peak in resistance versus frequency [42]. Whereas, plot of inductance versus frequency shows decrease in inductance around zero [42, 57]. In addition, the effect of increasing the thickness (t) of ferromagnetic film caused the eigen values (λ_q) to increase which increased the resonance frequency [42].

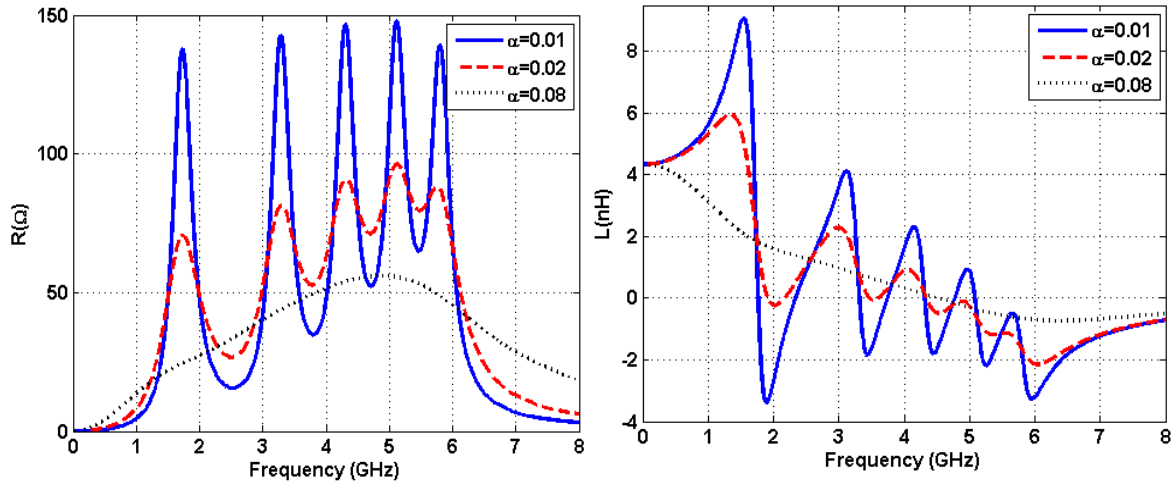

Figure 4.6: Plots of resistance (R) and inductance (L) versus frequency for single-turn inductor with length 1mm and variations in damping constant.

4.5 Solenoid Inductor Device Configuration and Fabrication

The single-turn inductors were fabricated with various device parameters such as signal line width, device length, ferromagnetic (NiFe) film thickness and pattern spacing etc, [8]. The structure of single-turn inductor designed using Advanced Design System (ADS) is demonstrated in figure-(4.7). The figure-(4.7), illustrates the variations in single-turn inductor structural device parameters such as signal line width (W_1), device position, Magnetic (NiFe) pattern spacing (μm), NiFe thickness (μm) etc, listed in table-(4.1).

Row/Dev	Line Width 'W_1'	Device Position	NiFe Pattern	NiFe thickness
x/y	5/10/20/50	Edge/Center	Solid/3/5/10	0.2/0.3/0.4

Table 4.1: Single-turn inductor configuration with ferromagnetic (NiFe) pattern width (300μm), insulating layer (SiO_2) thickness (0.5μm), NiFe pattern length 1000/2000 (μm) and total device length 1200/2200 (μm).

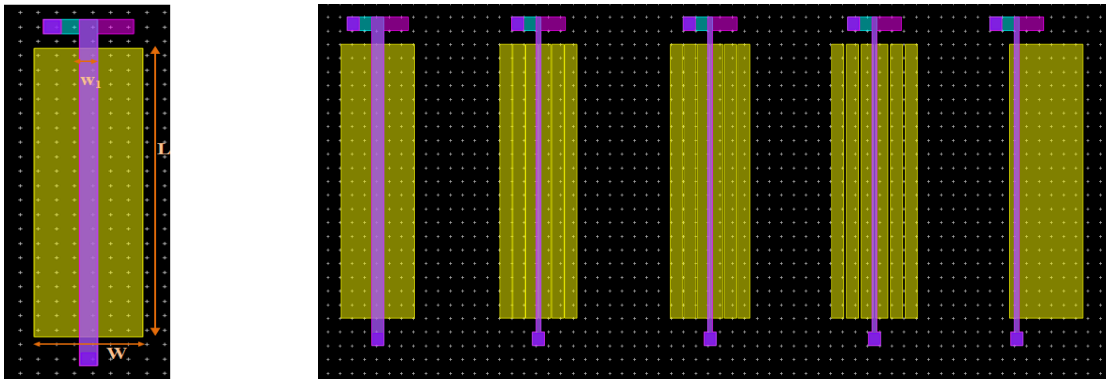

Figure 4.7: Single-turn inductors designed in Advanced design system (ADS).

The fabricated single-turn inductors were arranged in four rows with each row consisting ten devices. The fabricated devices were characterized in Microwave research laboratory at Wright State University. A permanent external magnetic (d-c) field of nearly 100-200 Oersted strength was applied during measurement for even distribution of magnetization across ferromagnetic (NiFe) film. The phenomenon of magnetic-dynamics in thin ferromagnetic (NiFe) films has been verified theoretically by performing modeling simulations and verified experimentally by measuring fabricated single-turn inductors. The magnetic dynamics of single-turn inductor magnetic thin film are observed as magnetic resonance peaks in measured impedance versus frequency results demonstrated in later section of chapter [42].

The r-f impedance measurements on a number of fabricated single-turn inductors were performed using Cascade r-f wafer probe station (M150) and 1-port ground-signal (G-S) probe [12]. The one-port measurement results were measured using Agilent network analyzer (PNA-N5230A) in form of scattering parameters (S-parameters) at 0.5-10GHz frequency range [12]. The system was calibrated using 1-port standard (Short-Open-Load) calibration technique prior to performing any measurements using impedance standard calibration substrate (Cascade S-G 103-726B). The calibration is necessary prior to performing any measurements to remove uncertainties during

measurements and to obtain accurate measurement data.

4.6 RF Characterization and Measurement

A large number of single-turn solenoid inductors with various structural parameters demonstrated in table-(4.1) were fabricated on wafers-2, 4a and 5 with various ferromagnetic (NiFe) thickness. The wafer-4a had magnetic film thickness of 0.4μm which yielded 40 devices out of which 30 devices were functioning. The wafer-5 with film thickness of 0.3μm yielded only five good devices. The measurement results obtained for measured single-turn inductors on wafers-2 and 5 are not listed in this chapter as they showed lower magnetic resonant peaks caused by lower thickness deposition of ferromagnetic film.

Device Image	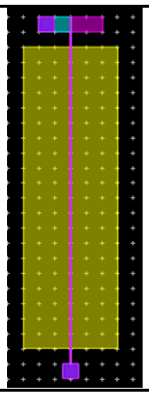	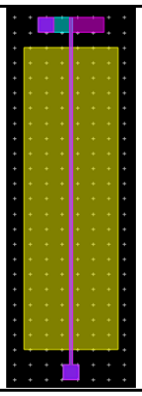	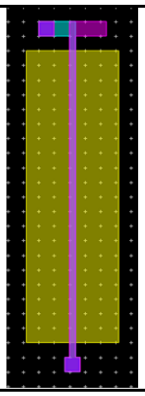	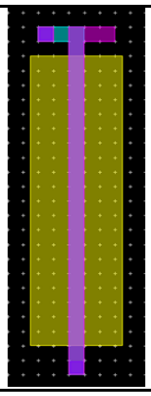	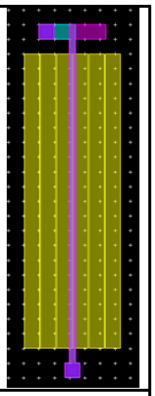
Row/Dev	**1/1**	**1/2**	**1/3**	**1/4**	**1/5**
Signal Line width (µm)	**5**	**10**	**20**	**50**	**20**
Position	**Center**	**Center**	**Center**	**Center**	**Center**
NiFe pattern	**Solid**	**Solid**	**Solid**	**Solid**	**3**

Figure 4.8: ADS layout of single-turn solenoid inductors with various structural parameters.

Additionally, it has been observed under microscope (M150) that most devices had over etched vias which shorted the signal lines and some devices had issues with top metal layer. However, out of 40 patterned devices on each wafer, 30 devices were functioning on wafer-4a with NiFe thickness of 0.4μm which provided sufficient mea-

surement data for r-f characterization and measurement analysis. The configuration of fabricated single-turn solenoid inductors are shown in figure-(4.8).

4.7 Experimental Results and Analysis

The experimental results for single-turn solenoid inductors for measured resistance and inductance versus frequency fabricated on wafer-4a with NiFe thickness of 0.4μm are listed in this section of chapter.

The measurement results for single-turn inductors on wafers-2 and 5 with NiFe thickness of 0.2μm and 0.3μm at frequency range 0.5-10GHz did not show any significant magnetic resonant peaks due to lower NiFe film deposition thickness. The single-turn inductor devices measured on wafer-4a had thicker NiFe film (0.4μm) which showed enhanced magnetic resonance peaks similar to modeling simulation results.

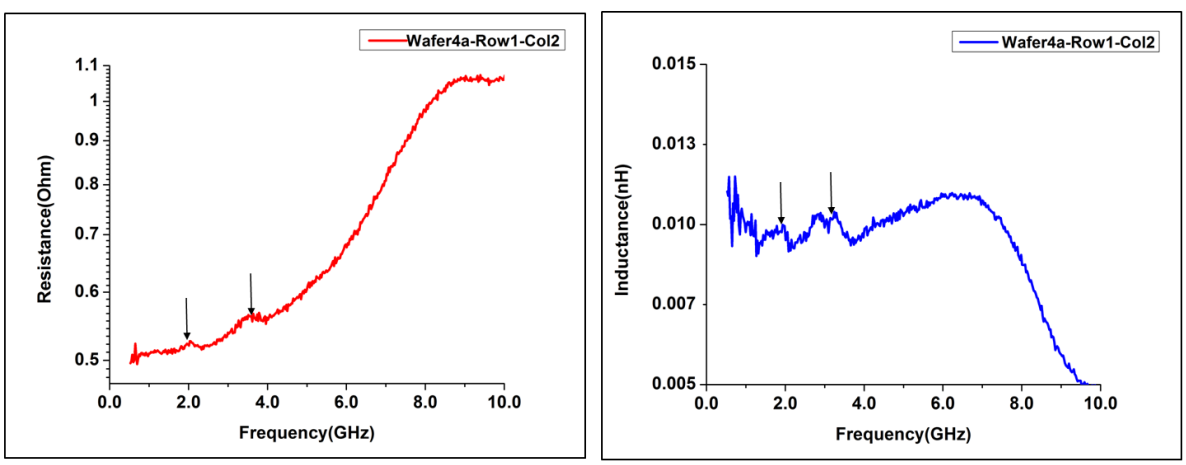

Figure 4.9: Plots of measured resistance (R) and inductance (L) versus frequency for single-turn inductor (Row1-Column2) with signal line width (W_1) 10μm, NiFe pattern width (W) 300μm, NiFe pattern length (L) 1000μm, NiFe Pattern (Solid), Device position (Center), Total device length 1200μm.

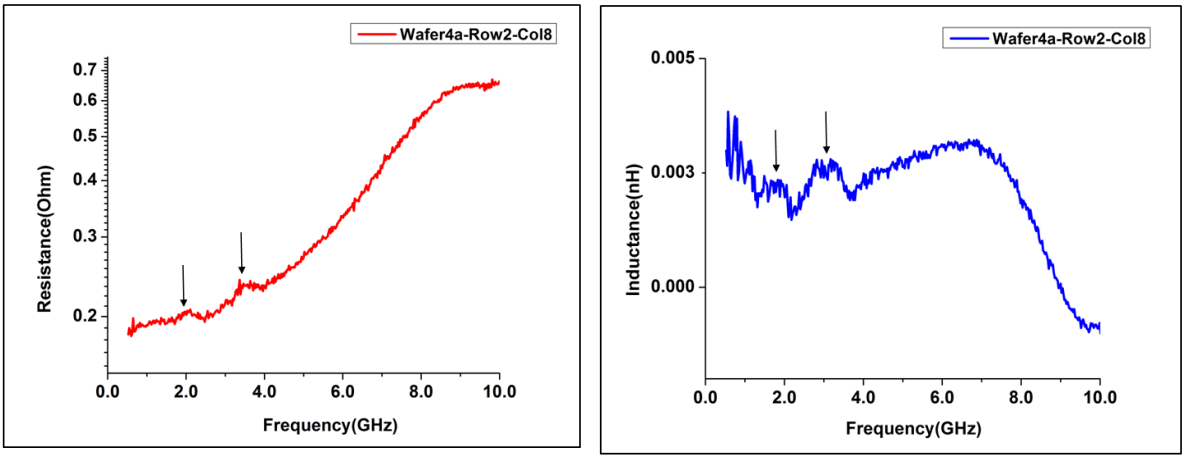

Figure 4.10: Plots of measured resistance (R) and inductance (L) versus frequency for single-turn inductor (Row2-Column8) with signal line width (W_1) 20μm, NiFe pattern width (W) 300μm, NiFe pattern length (L) 1000μm, NiFe Pattern (Solid), Device position (edge-1), Total device length 1200μm.

The measurement results for single-turn inductors are presented in figures-(4.9) and (4.10) which shows existence of magnetic resonance peaks at 2GHz and 4GHz frequencies similar to theoretical simulations. However, the resonance peaks observed in the measurement results are weak due to lower NiFe film thickness which resulted in weak magneto-static excitations in inductor magnetic core [42].

The fabricated single-turn inductor measurement results presented in figures-(4.9) and (4.10) shows that measured resistance and inductance as a function of frequency shows preliminary effects and some proof of existence of magnetic resonant peaks close to 2GHz and 4GHz frequency. The existence of magnetic resonant peaks for measured single-turn inductors corresponds to magneto-static excitations in core observed as magnetic resonance modes [42]. In order to observe the effect of enhanced magnetic resonance peaks corresponding to thin magnetic film future work is needed. In addition, the effect of variations in signal line width (W_1), device length (L), ferromagnetic (NiFe) pattern spacing, device position etc, also needs to be investigated in future work. The effect of magnetic resonance peaks being not so significant in measure-

ment results can be related to a number of reasons such as lower NiFe film thickness, strength of applied external (DC) magnetic field, device fabrication imperfections etc. Additionally, the fabricated single-turn solenoid inductor devices showed roughness along the edges of the fabricated device caused due to imperfections in fabrication etching procedure which significantly affected the single-turn inductor device performance. Therefore, in order to further understand the effects of variations in device length, signal line width and pattern spacing three dimensional (3D) electromagnetic simulations needs to be performed in future to verify the observed phenomenon.

4.8 Conclusions

The theoretical analysis and experimental results for calculating r-f impedance of single-turn solenoid inductor built using thin ferromagnetic film are presented in this chapter [42]. The magneto-static approximation and Greens function was applied to calculate impedance of single-turn inductor in terms of magneto-static eigen modes of thin ferromagnetic film [42]. The electrical device characteristics of single-turn inductor such as resistance and inductance versus frequency has been measured and analyzed in this work which depended on induced magnetic field in inductor coil [42]. The experimental results showed existence of magneto-static modes in thin ferromagnetic stripe [42]. Therefore, the developed theoretical concept for calculating impedance of single-turn inductor can be used for modeling the effect of width, length and thickness of ferromagnetic stripe [42]. In addition, the effect of magnetic loss on resistance and inductance versus frequency for single-turn solenoid inductor has been verified in modeling results [42].

CHAPTER V

Recommendations for Future Work

5.1 Conclusions

The r-f integrated components such as inductors, transformers, transmission lines, coplanar waveguides etc., utilized in r-f integrated circuits (RFICs) suffer from major drawbacks such as large component size, low quality factor and RC delay. The application of thin ferromagnetic (FM) films for scaling r-f integrated components based on proposed low-loss conductor technology for improving device characteristics has been investigated in this work. The main motivation and goal of this work has been to reduce RC delay and improve r-f device characteristics such as inductance, quality factor, attenuation etc, for r-f components operating at high frequencies [12, 13, 14]. Various parameters such as types of devices, magnetic materials, fabrication procedure etc, has been investigated in this work. The main results and observations of this work are summarized below which are followed by recommendations for future work.

• The new concept of artificial low-loss technology has been introduced in this work (chapter-2) based on artificial layered metamaterial (ARLYM). The low-loss conductor consists of $Ni_{80}Fe_{20}$/Cu superlattice which provided significant skin-effect suppression and increased skin depth at r-f frequencies [12, 13, 14]. The effective permeability of low-loss conductor becomes zero at anti-resonance frequency by modeling thickness between metal (Copper) and ferromagnetic (NiFe) layers [12, 13, 14].

• The experimental results for low-loss conductor showed increase in quality factor (41%) for single-turn (2nH) inductor at 14.5GHz frequency [12]. In addition, increase of (86%) quality factor for single-turn spiral inductors has been obtained in this work

when compared to reference copper inductors [13]. The loss reduction of 70% for coplanar waveguide devices has been achieved at 10GHz frequency [12, 13, 14]. The bandwidth for skin effect suppression obtained is 10-18GHz frequency range [12].

• The application of external magnetic (d-c) field was not required in this work due to magnetic anisotropy property in ferromagnetic (FM) layers [14]. Therefore, the newly developed concept of artificial low-loss conductor (ARLYM) in this work can be used for improving clock frequency, output power, system speed etc, in r-f integrated circuits [12, 13, 14].

• In addition, second part of this work consisted of theoretical and experimental analysis for r-f single-turn solenoid inductors built using thin ferromagnetic (FM) films (chapter-4) [42]. The main motivation for carrying out this research work is related to studying magnetic properties in thin ferromagnetic (FM) films which are required for scaling r-f components size at microwave frequencies.

• The r-f impedance modeling has been performed using single-turn inductors built using thin ferromagnetic film based on magneto-static thin film approximation [42]. The magneto-static approximation and Greens function was used for calculating impedance versus frequency for single-turn inductor at r-f frequencies. The magneto-static excitations in inductor are observed in form of magnetic resonance modes in simulation results [42]. Therefore, the effect of magneto-static excitations in inductor magnetic core on electrical characteristics such as inductance and resistance versus frequency are analyzed [42].

• The experimental analysis consisted of single-turn solenoid inductors fabricated with variations in device parameters such as signal line width, device length, ferromagnetic (NiFe) film with varied thickness and pattern spacing etc, (Chapter-4). The experimental analysis of single-turn inductors was performed in this work for verifying the theoretical calculations. The measurement results for devices on wafer-4a with thicker ferromagnetic (NiFe) film deposition (0.4μm) provided effcient measurement

data for analysis showing existence of magnetic resonance modes similar to modeling results.

5.2 Future work

The problems associated with fabricating thin ferromagnetic film deposition in low-loss superlattice conductor is biggest challenge in this work. In future, it is necessary to continue further investigations for fabricating uniform NiFe film deposition. In addition, cost effective solution needs to be developed for fabricating low-loss conductor.

The fabrication of single-turn solenoid inductors had some major issues which needs to be overcome in future such as devices had over-etched vias which shorted signal lines and problems with top metal layer. In addition, fabricated devices had surface roughness along the edges which significantly impacted the measurement results. In future, sharp etching procedure needs to be developed in order to overcome this problem. Also great care and caution is required for handling wet chemical etching during fabrication procedure which was the most critical step during fabrication.

The r-f experimental results presented for single turn solenoid inductors (chapter-4) provided a proof concept of magnetic resonance peaks in thin NiFe films. However, further investigations and measurements needs to be performed in future to observe enhanced magnetic resonance peaks similar to modeling results. The thickness of patterned NiFe film for single-turn inductor devices was much lower which caused difficulty in observing magnetic resonance peak in experiments. Therefore, NiFe films with higher deposition thickness ($>0.4\mu$m) are required to direct future experimental work. The strength of external magnetic field applied during measurements for single-turn inductors was greater (100-200Oe) which significantly impacted measurement data. Therefore, the effect of changing magnetic field strength also needs to be investigated. Lastly, variations in device parameters such as magnetic film pattern, width

and lengths also needs to be measured and compared to full wave electromagnetic (EM) simulation results in future experiments.

APPENDICES

APPENDIX A

Permeability tensor in thin ferromagnetic films

The structure of low-loss superlattice built by placing alternating layers of metal (Cu) and ferromagnetic (NiFe) film is demonstrated in figure-(2.5) (chapter-2). As illustrated in figure-(2.5) 'w' is width of the strip along y-axis and 't' is thickness of the strip directed along z-axis [11, 42, 70].

It is assumed that ferromagnetic (FM) film is magnetized along strip in x-direction with uniform static magnetization ($M_s\vec{x}$) by applying the external magnetic (d-c) field ($H_0\vec{x}$) [11, 42]. The r-f current flow generates a time harmonic r-f field known as external field [10, 24]. It is assumed that the length (l) of the strip along x-axis is much longer than width (w) along the y-axis ($l >> w$) [42]. By assuming the small signal condition the magnitude of induced r-f magnetization ('$\vec{m}$') is much smaller than the magnetic saturation (M_s) ($\vec{m} << M_s$). Also considering that longitudinal component of r-f magnetization vector can be neglected ($\vec{m} = m_y\hat{y} + m_z\hat{z}$) as the strip is magnetized along x-direction, m_x=0 [42].

In order to investigate the application of magnetic materials for r-f device applications the dynamics of magnetization under the influence of externally applied magnetic (d-c) field is considered. In general, the r-f field is generated by the current carrying conductor placed close to the magnetic sample. The macroscopic equation of motion of the magnetization vector is given by the equation-(A.1) [10, 24].

$$\frac{d\vec{M}}{dt} = -\gamma\left(\vec{M} \times \vec{H}\right) \tag{A.1}$$

The minus sign in equation-(A.1) is due to the negative charge of electron [10,

24]. If the absolute value of the electron charge is considered then the Landau-Lifshitz equation is given by [10, 24],

$$\frac{d\vec{M}}{dt} = \gamma \left(\vec{M} \times \vec{H} \right) \tag{A.2}$$

In the above equation-(A.2), 'γ' is the gyromagnetic constant given by $\gamma = \frac{ge}{2mc} = 1.75882 \times 10^7 Oe^{-1}s^{-1}$ [24]. Where, 'e' is the absolute value of the electron charge, 'm' is mass of the electron, 'c' is the velocity of light and 'g' is spectroscopic splitting factor ($\cong 2$) [10, 24].

The value of Lande' spectroscopic splitting factor (g) is influenced by degree of coupling between the magnetic moments of spin and orbital motion [24]. When the coupling is zero, the value of 'g' for spin alone is ($\cong 2$) , and for orbital motion is g=1 [10, 24]. When the coupling effect between the spin and orbital moments is considered then the value associated with 'g' is assumed to be larger than 2 [10, 24].

The total effective magnetic field vector is given by [24],

$$\vec{H} = \vec{H_0} + \vec{h}e^{j\omega t} \tag{A.3}$$

Where, '$\vec{H_0}$' is the vector sum of all DC fields within the magnetic material which includes externally applied DC magnetic field, internal magnetocrystalline anisotropy field and demagnetization field (shape anisotropy) [10, 11, 24].

In ideal case the medium is considered to be infinite and the anisotropy associated with the crystal lattice or magnetostriction is zero [24]. Therefore, only the externally applied field contributes to '$\vec{H_0}$' [10, 24].

The r-f term in equation-(A.3) consists of amplitude '$\vec{h}$' and microwave frequency 'ω'

The total magnetization field is given by equation-(A.4) [10, 24]

$$\vec{M} = \vec{M_0} + \vec{m}e^{j\omega t} \tag{A.4}$$

Where, '$\vec{M_0}$' is DC magnetization vector and '$\vec{m}$' is the r-f magnetization vector [10, 24].

Therefore, $\vec{M_0} >> \vec{m}$ and $\vec{H_0} >> \vec{h}$

Derivation of r-f magnetization vector

In order to derive the r-f magnetization vector '$\vec{m}$' the equations-(A.3) and (A.4) for effective magnetic field '$\vec{H}$' and magnetization field '$\vec{M}$' are substituted in the macroscopic equation (equation-A.2) and expanded in terms of exponential components of time as shown below [24]

$$\frac{d}{dt}\left(\vec{M_0} + \vec{m}e^{j\omega t}\right) = \gamma\left[\left(\vec{M_0} + \vec{m}e^{j\omega t}\right) \times \left(\vec{H_0} + \vec{h}e^{j\omega t}\right)\right]$$

$$\vec{m}e^{j\omega t}\left(j\omega\right) = \gamma\left[\left(\vec{M_0} \times \vec{H_i}\right) + \left(\vec{M_0} \times \vec{h}e^{j\omega t}\right) + \left(\vec{m}e^{j\omega t} \times \vec{H_0}\right) + \left(\vec{m}e^{j\omega t} \times \vec{h}e^{j\omega t}\right)\right]$$

By neglecting the non-linear terms in the above listed expression and making use of the linear approximation the DC equation is obtained as follows [24]

$$\gamma\left(M_0 \overset{\rightarrow}{\times} \vec{H_0}\right) = 0 \tag{A.5}$$

The above equation-(A.5) states that the DC magnetic field vector $\vec{H_0}$ and magnetization vector $\vec{M_0}$ are along the same direction [24]. Similarly, the a-c equation is obtained by equating all non-linear coefficients of the first power in '$j\omega t$' as follows [24].

$$\frac{d}{dt}\left[\vec{M_0} + \vec{m}\ e^{j\omega t}\right] = \gamma\left[\left(\vec{M_0} + \vec{m}e^{j\omega t}\right) \times \left(\vec{H_0} + \vec{h}e^{j\omega t}\right)\right]$$

$$\vec{m}e^{j\omega t}\left(j\omega\right) = \gamma\left[\left(\vec{M_0} \times \vec{H_i}\right) + \left(\vec{M_0} \times \vec{h}e^{j\omega t}\right) + \left(\vec{m}e^{j\omega t} \times \vec{H_0}\right) + \left(\vec{m}e^{j\omega t} \times \vec{h}e^{j\omega t}\right)\right]$$

$$\vec{m}\left(j\omega\right) = \gamma\left[\left(\vec{M}_0 \times \vec{h}\right) + \left(\vec{m} \times \vec{H}_0\right)\right] \tag{A.6}$$

The above equation-(A.6) is used for calculating the Susceptibility tensor $\check{\chi}$ [24].

Therefore, by cross-multiplying equation-(A.6) by '$\vec{H}_0$' on both sides from right and expanding the cross product by using the relation $\vec{A} \times \left(\vec{B} \times \vec{C}\right) = \left(\vec{A} \cdot \vec{C}\right)\vec{B} - \left(\vec{A} \cdot \vec{B}\right)\vec{C}$ we obtain [24]

$$j\omega\vec{m} \times \vec{H}_0 = \gamma\left(\vec{M}_0 \times \vec{h}\right) \times \vec{H}_0 + \gamma\left(\vec{m} \times \vec{H}_0\right) \times \vec{H}_0$$

$$j\omega\vec{m} \times \vec{H}_0 = \gamma\left[\left(\vec{H}_0 \cdot \vec{M}_0\right)\vec{h} - \left(\vec{H}_0 \cdot \vec{h}\right)\vec{M}_0\right] + \gamma\left[\left(\vec{H}_0 \cdot \vec{m}\right)\vec{H}_0 - \left(\vec{H}_0 \cdot \vec{H}_0\right)\vec{m}\right]$$

$$j\omega\vec{m} \times \vec{H}_0 = \gamma\left(\vec{H}_0 \cdot \vec{M}_0\right)\vec{h} - \gamma\left(\vec{H}_0 \cdot \vec{h}\right)\vec{M}_0 + \gamma\left(\vec{H}_0 \cdot \vec{m}\right)\vec{H}_0 - \gamma\left(\vec{H}_0 \cdot \vec{H}_0\right)\vec{m} \tag{A.7}$$

The scalar product can be obtained in the similar way by multiplying equation-(A.7) by '$\cdot\vec{H}_0$' on both sides and using $\gamma\left(\vec{M}_0 \times \vec{H}_0\right) = 0$ [24].

Therefore, we obtain [24]

$$j\omega\vec{m} \cdot \vec{H}_0 = \gamma\left(\vec{M}_0 \times \vec{h}\right) \cdot \vec{H}_0 + \gamma\left(\vec{m} \times \vec{H}_0\right) \cdot \vec{H}_0$$

By making use of the relation $\left(\vec{A} \times \vec{B}\right) \cdot \vec{C} = \left(\vec{C} \times \vec{A}\right) \cdot \vec{B} = \left(\vec{B} \times \vec{C}\right) \cdot \vec{A}$ in the above expression we obtain [24]

$$j\omega\vec{m} \cdot \vec{H}_0 = \gamma\left(\vec{H}_0 \times \vec{M}_0\right) \cdot \vec{h} + \gamma\left(\vec{H}_0 \times \vec{H}_0\right) \cdot \vec{m} \tag{A.8}$$

By using $\gamma\left(\vec{M}_0 \times \vec{H}_0\right) = 0$ from equation-(A.5) in equation-(A.8) we obtain [24]

$$j\omega\vec{m} \cdot \vec{H}_0 = 0 \tag{A.9}$$

Therefore, we obtain $\vec{m} \cdot \vec{H}_0 = 0$ in the above relation (equation-A.9) which shows that the r-f magnetization vector '$\vec{m}$' is perpendicular to the applied field $\vec{H}_0$ [24].

By substituting equation-(A.9) in equation-(A.7) we obtain equation-(A.10) as follows [24]

$$j\omega\vec{m} \times \vec{H}_0 = \gamma\left(\vec{H}_0 \cdot \vec{M}_0\right)\vec{h} - \gamma\left(\vec{H}_0 \cdot \vec{h}\right)\vec{M}_0 - \gamma\left(\vec{H}_0 \cdot \vec{H}_0\right)\vec{m} \tag{A.10}$$

Now multiplying by 'γ' on both sides of equation-(A.10) we get,

$$j\omega\vec{m} \times \vec{H}_0 = \gamma^2\left(\vec{H}_0 \cdot \vec{M}_0\right)\vec{h} - \gamma^2\left(\vec{H}_0 \cdot \vec{h}\right)\vec{M}_0 - \gamma^2\left(\vec{H}_0 \cdot \vec{H}_0\right)\vec{m}$$

$$j\omega\vec{m} \times \vec{H}_0 = \gamma^2\left(\vec{H}_0 \cdot \vec{M}_0\right)\vec{h} - \gamma^2\left(\vec{H}_0 \cdot \vec{h}\right)\vec{M}_0 - \gamma^2 H_0^2\vec{m}$$

$$j\omega\vec{m} \times \vec{H}_0 + \gamma^2 H_0^2\vec{m} = \gamma^2\left(\vec{H}_0 \cdot \vec{M}_0\right)\vec{h} - \gamma^2\left(\vec{H}_0 \cdot \vec{h}\right)\vec{M}_0$$

By using the relation $\omega_H = \gamma H_0$ in the above expression, we obtain [24]

$$\gamma j\omega\vec{m} \times \vec{H}_0 + \omega_H^2\vec{m} = \gamma^2\left(\vec{H}_0 \cdot \vec{M}_0\right)\vec{h} - \gamma^2\left(\vec{H}_0 \cdot \vec{h}\right)\vec{M}_0 \tag{A.11}$$

By adding '$j\omega\gamma\left(\vec{M}_0 \times \vec{h}\right)$' on both sides of equation-(A.11) we obtain,

$$\gamma j\omega\vec{m}\times\vec{H}_0+\omega_H^2\vec{m}+j\omega\gamma\left(\vec{M}_0 \times \vec{h}\right) = \gamma^2\left(\vec{H}_0 \cdot \vec{M}_0\right)\vec{h}-\gamma^2\left(\vec{H}_0 \cdot \vec{h}\right)\vec{M}_0+j\omega\gamma\left(\vec{M}_0 \times \vec{h}\right)$$

$$\omega_H^2\vec{m} + j\omega\gamma\left[\left(\vec{m} \times \vec{H}_0\right) + \left(\vec{M}_0 \times \vec{h}\right)\right] = \left[\gamma^2\left(\vec{H}_0 \cdot \vec{M}_0\right)\vec{h} - \gamma^2\left(\vec{H}_0 \cdot \vec{h}\right)\vec{M}_0 + j\omega\gamma\left(\vec{M}_0 \times \vec{h}\right)\right]$$

By using equation-(A.6) in the above expression we have

$$\omega_H^2\vec{m} + j\omega\left(j\omega\vec{m}\right) = j\omega\gamma\left(\vec{M}_0 \times \vec{h}\right) + \gamma^2\left(\vec{H}_0 \cdot \vec{M}_0\right)\vec{h} - \gamma^2\left(\vec{H}_0 \cdot \vec{h}\right)\vec{M}_0$$

$$\vec{m}\left(\omega_H^2 - \omega^2\right) = j\omega\gamma\left(\vec{M}_0 \times \vec{h}\right) + \gamma^2\left(\vec{H}_0 \cdot \vec{M}_0\right)\vec{h} - \gamma^2\left(\vec{H}_0 \cdot \vec{h}\right)\vec{M}_0$$

Thus, the magnetization vector '$\vec{m}$' is given by (equation-A.12)

$$\vec{m} = \frac{1}{\left(\omega_H^2 - \omega^2\right)}\left[j\omega\gamma\left(\vec{M}_0 \times \vec{h}\right) + \gamma^2\left(\vec{H}_0 \cdot \vec{M}_0\right)\vec{h} - \gamma^2\left(\vec{H}_0 \cdot \vec{h}\right)\vec{M}_0\right] \tag{A.12}$$

The magnetization vector '$\vec{m}$' has singularity when $\omega = \omega_H = \gamma H_0$ [24].

Susceptibility Tensor

In order to extract the individual components of magnetization vector ($\vec{m} = m_y\hat{y} + m_z\hat{z}$) i.e., '$m_y$' and '$m_z$' from equation-(A.12) we consider '$\vec{H}_0$' and '$\vec{M}_0$' along the x-axis as they are along the same direction (equation-A.5) and the applied r-f field is given by $\vec{h} = i_x h_x + i_y h_y + i_z h_z$ [13, 20, 24].

Thus, the magnetization components 'm_y' and 'm_z' are obtained as follows [10, 24]

$$m_y = \tfrac{1}{\omega_H^2 - \omega^2}\left[-j\omega\gamma\vec{M}_0 h_z + \gamma^2\vec{H}_0\vec{M}_0 h_y\right]$$

$$m_y = \frac{\gamma\vec{M}_0}{\omega_H^2 - \omega^2}\left[-j\omega h_z + \omega_H h_y\right] \tag{A.13}$$

Since, $\omega_H = \gamma H_0$

$$m_z = \tfrac{1}{\omega_H^2 - \omega^2}\left[j\omega\gamma\vec{M}_0 h_y + \gamma^2\vec{H}_0\vec{M}_0 h_z\right]$$

$$m_z = \frac{\gamma\vec{M}_0}{\omega_H^2 - \omega^2}\left[j\omega h_y + \omega_H h_z\right] \tag{A.14}$$

Similarly we obtain,

$$m_x = \tfrac{1}{\omega_H^2 - \omega^2}\left[\gamma^2\vec{M}_0\vec{H}_0 h_x - \gamma^2\vec{H}_0\vec{M}_0 h_x\right] = 0$$

$$m_x = 0 \tag{A.15}$$

In the above equations '$\vec{M}_0$' is the saturation magnetization [24]. The r-f magnetization vector '$\vec{m}$' and applied r-f field '$\vec{h}$' are related by the expression [10, 24, 42]

$$\vec{m} = \check{\chi} \cdot \vec{h} \tag{A.16}$$

From the above equation-(A.16), '$\check{\chi}$' is the susceptibility tensor and '$\vec{h}$' is applied total r-f magnetic field.

The susceptibility tensor is given by [10, 24]

$$\check{\chi} = \begin{bmatrix} 0 & 0 & 0 \\ 0 & \chi_{yy} & \chi_{yz} \\ 0 & \chi_{zy} & \chi_{zz} \end{bmatrix} \tag{A.17}$$

In order to extract each of the individual components of susceptibility tensor '$\check{\chi}$' the relation in equation-(A.17) can be used as listed below:

$$\begin{bmatrix} m_x \\ m_y \\ m_z \end{bmatrix} = \begin{bmatrix} 0 & 0 & 0 \\ 0 & \chi_{yy} & \chi_{yz} \\ 0 & \chi_{zy} & \chi_{zz} \end{bmatrix} \begin{bmatrix} h_x \\ h_y \\ h_z \end{bmatrix}$$

$$\begin{bmatrix} m_x \\ m_y \\ m_z \end{bmatrix} = \begin{bmatrix} 0 \\ \chi_{yy}h_y + \chi_{yz}h_z \\ \chi_{zy}h_y + \chi_{zz}h_z \end{bmatrix}$$

$$m_x = 0 \tag{A.18}$$

$$m_y = \chi_{yy}h_y + \chi_{yz}h_z \tag{A.19}$$

$$\frac{\gamma M_0}{\left(\omega_H^2 - \omega^2\right)}\left(-j\omega h_z + \omega_H h_y\right) = \chi_{yy}h_y + \chi_{yz}h_z$$

$$\chi_{yy} = \frac{\gamma \vec{M}_0 \omega_H}{\left(\omega_H^2 - \omega^2\right)};\ \chi_{yz} = \frac{-j\omega\gamma\vec{M}_0}{\left(\omega_H^2 - \omega^2\right)}$$

$$m_z = \chi_{zy}h_y + \chi_{zz}h_z \tag{A.20}$$

$$\frac{\gamma M_0}{\left(\omega_H^2 - \omega^2\right)}\left(j\omega h_y + \omega_H h_z\right) = \chi_{zy}h_y + \chi_{zz}h_z$$

$$\chi_{zy} = \frac{j\omega\gamma\vec{M}_0}{\left(\omega_H^2 - \omega^2\right)};\ \chi_{zz} = \frac{\gamma \vec{M}_0 \omega_H}{\left(\omega_H^2 - \omega^2\right)}$$

Thus,

$$-\chi_{yz} = \chi_{zy} = \frac{j\omega\gamma\vec{M}_0}{\left(\omega_H^2 - \omega^2\right)} = \frac{j\omega\omega_M}{\left(\omega_H^2 - \omega^2\right)}$$

$$\chi_{yy} = \chi_{zz} = \frac{\gamma \vec{M_0} \omega_H}{\left(\omega_H^2 - \omega^2\right)} = \frac{\omega_M \omega_H}{\left(\omega_H^2 - \omega^2\right)}$$

Where,

$$\omega_M = \gamma 4\pi M_0$$

Therefore, the 3×3 Susceptibility tensor is given by [24],

$$\check{\chi} = \begin{bmatrix} 0 & 0 & 0 \\ 0 & \chi_{yy} & \chi_{yz} \\ 0 & \chi_{zy} & \chi_{zz} \end{bmatrix}$$

$$\check{\chi} = \begin{bmatrix} 0 & 0 & 0 \\ 0 & \frac{\omega_H \omega_M}{\left(\omega_H^2 - \omega^2\right)} & \frac{-j\omega\omega_M}{\left(\omega_H^2 - \omega^2\right)} \\ 0 & \frac{j\omega\omega_M}{\left(\omega_H^2 - \omega^2\right)} & \frac{\omega_H \omega_M}{\left(\omega_H^2 - \omega^2\right)} \end{bmatrix}$$

$$\check{\chi} = \frac{\omega_M}{(\omega_H^2 - \omega^2)} \begin{bmatrix} 0 & 0 & 0 \\ 0 & \omega_H & -j\omega \\ 0 & j\omega & \omega_H \end{bmatrix} \tag{A.21}$$

Where, $\omega_M = \gamma M_s$, $\omega_H = \gamma H_0$ and 'γ' is the gyromagnetic constant [10, 24]

The permeability tensor is given by (equation-A.22) [10, 24]

$$\check{\mu} = \begin{bmatrix} 0 & 0 & 0 \\ 0 & \mu_{yy} & \mu_{yz} \\ 0 & \mu_{zy} & \mu_{zz} \end{bmatrix} \tag{A.22}$$

The relationship between the permeability and susceptibility tensor is given by [24]

$$\check{\mu} = \left[\check{1} + \check{\chi}\right] \tag{A.23}$$

Where, $\check{1}$ is the three-dimensional unit tensor given by,

$$\check{1} = \begin{bmatrix} 1 & 0 & 0 \\ 0 & 1 & 0 \\ 0 & 0 & 1 \end{bmatrix}$$

$$\check{\mu} = \begin{bmatrix} 1 & 0 & 0 \\ 0 & 1 + \frac{\omega_H \omega_M}{\left(\omega_H^2 - \omega^2\right)} & \frac{-j\omega\omega_M}{\left(\omega_H^2 - \omega^2\right)} \\ 0 & \frac{j\omega\omega_M}{\left(\omega_H^2 - \omega^2\right)} & 1 + \frac{\omega_H \omega_M}{\left(\omega_H^2 - \omega^2\right)} \end{bmatrix}$$

Therefore, the relative permeability tensor inside the magnetic film is given by [10, 11, 24]

$$\check{\mu} = \begin{bmatrix} 1 & 0 & 0 \\ 0 & \mu & -j\mu_a \\ 0 & j\mu_a & \mu \end{bmatrix} \tag{A.24}$$

Where,

$$\mu = 1 + \frac{\omega_H \omega_M}{\omega_H^2 - \omega^2} \tag{A.25}$$

$$\mu_a = \frac{\omega\omega_M}{\omega_H^2 - \omega^2} \tag{A.26}$$

$$\omega_M = \gamma M_s, \omega_H = \gamma H_0$$

APPENDIX B

Calibration, Scattering Parameters and De-embedding

The experimental setup, calibration and measurement procedure performed using standard Short-Open-Load-Thru (SOLT), extraction of scattering parameters (S-parameters) and de-embedding are demonstrated in this appendix.

Calibration Measurement

The calibration needs to be performed prior to performing any measurements to remove uncertainities and obtain accurate measurement data. In general, the standard 2-port calibration techniques used are Short-Open-Load-Thru (SOLT) (or) Line-Reflect-Reflect-Match (LRRM) etc,.

The Short-Open-Load-Thru (SOLT) calibration procedure was utilized in this work by using impedance calibration substrate (Cascade 101-190C). The calibration results were verified on network analyzer (VNA) using smith chart. The calibration results has also been verified mathematically using 12-error term model demonstrated in later section of this appendix.

Short-Open-Load-Thru (SOLT)

The Short-Open-Load-Thru (SOLT) calibration technique utilizes four independent structures namely Short, Open, Load and Thru using Cascade (101-190C) r-f calibration substrate shown in figure-(B.1).

The calibration measurement for each impedance standard are extracted using vector network analyzer and verified on smith chart and log-magnitude (dB) over desired frequency range.

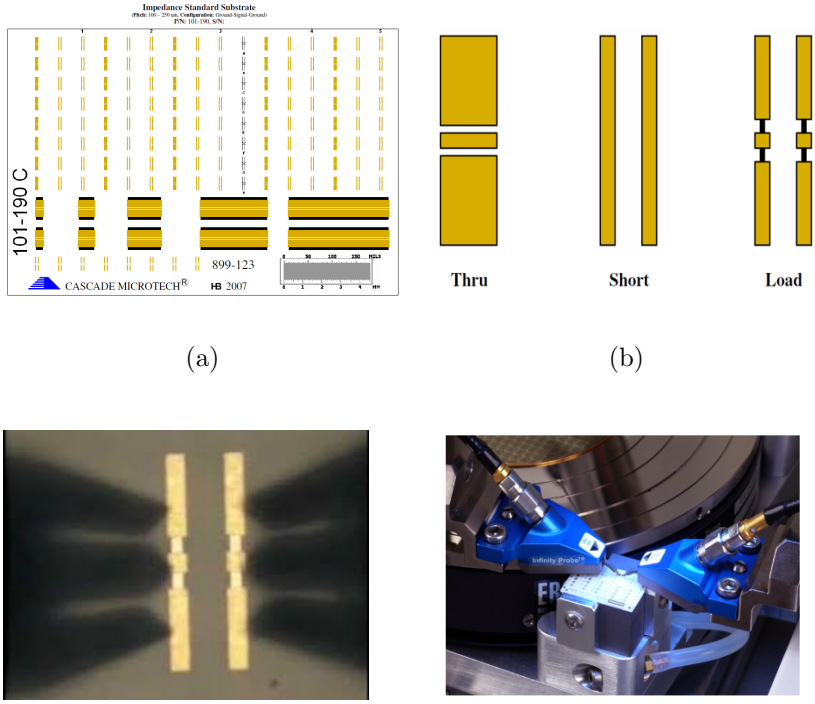

(a) (b)

(c) (d)

Figure B.1: Figures showing (a) Impedance standard calibration substrate, (b) Short-Open-Load-Thru (SOLT) (c) r-f probe contact on load structure, (d) r-f infinity probes.

SHORT: The calibration for short is performed by placing ground-signal-ground (G-S-G) probes on top of short structure and ensuring that the two ports are shorted i.e., S_{12}=S_{21}=0 indicating that there is no interference between ports 1 and 2. The result for short calibration (smith chart) is shown in figure-B.3 (c) which indicates that result is concentrated towards left edge on smith chart indicating zero impedance. On the other hand magnitude (dB) plot for short calibration is shown in figure-(B.2) (C) which indicates the magnitude range is around ±0.15 dB at 0.5-4GHz calibration frequency range.

OPEN: The calibration for open is performed by lifting the r-f probe above the substrate (>200μm) in air. The probe is lifted in air to eliminate parasitic effects caused by the adjacent structures.

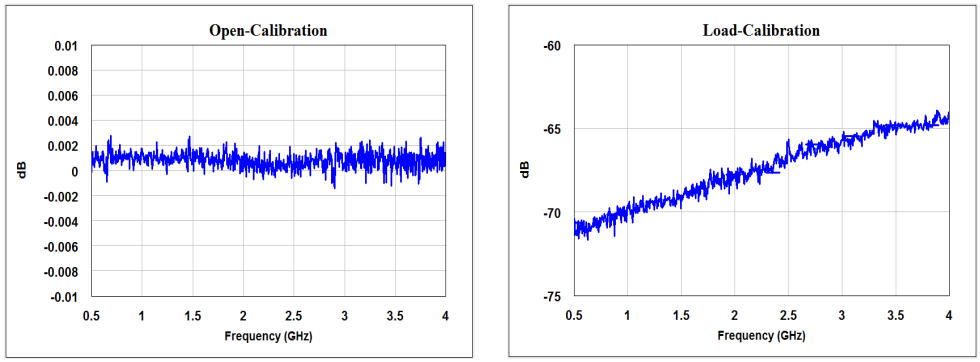

(a)

(b)

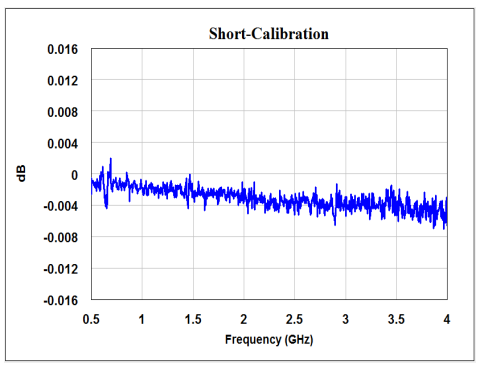

(c)

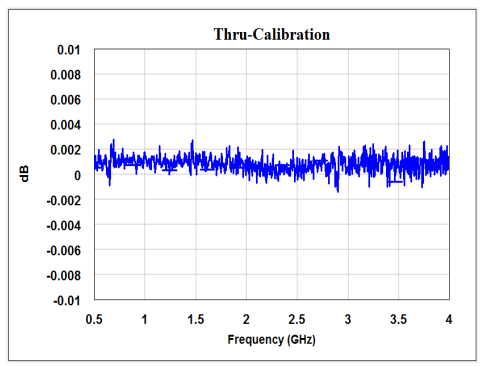

(d)

Figure B.2: Calibration measurement results in magnitude (dB) versus frequency for (a) Open, (b) Load, (c) Short and (d) Thru.

The smith chart graph obtained on network analyzer for Open is shown in figure-(B.3) (a) indicating the result is concentrated towards right edge of smith chart i,e., infinite impedance. The magnitude (dB) versus frequency result for Open is shown in figure-(B.2) (a) which shows the magnitude range is approximately ± 0.05 dB.

LOAD: The calibration for Load is performed by placing G-S-G r-f probes on Load structure. The contact indicates impedance equal to system characteristic impedance i.e., 50Ω. The smith chart result for Short calibration measurement is shown in figure-(B.3) (b) indicating the result is located at the center of the smith chart. On the other hand the magnitude (dB) plot shown in figure-(B.2) (b) illustrates that the magnitude is less than -40 dB for 0.5-4GHz calibration frequency range.

The smith chart results for Short-Open-Load-Thru measurement are listed in figure-(B.3).

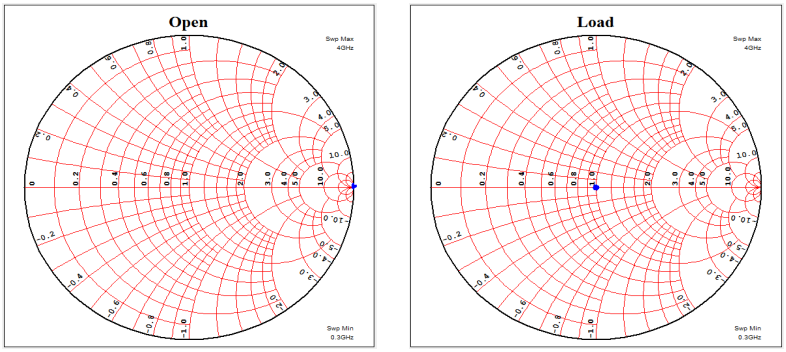

(a)

(b)

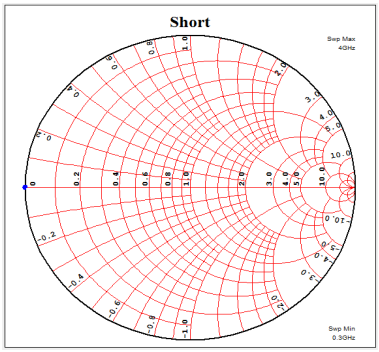

(c)

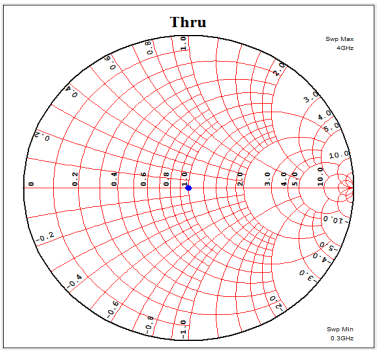

(d)

Figure B.3: Calibration measurement results on Smith chart for (a) Open, (b) Load, (c) Short and (d) Thru.

THRU: The calibration for Thru is performed by making contact on Thru structure using ground-signal-ground (G-S-G) r-f probes. The smith chart result for Thru calibration is shown in figure-(B.3) (d) indicating that the result is located at center of the smith chart (i.e., S_{12}=S_{21}=1; S_{11}=S_{22}=0). On the other hand the magnitude (dB) plot shown in figure-(B.2) (d) indicates the magnitude range is between ±0.05 dB for 0.5-4GHz calibration frequency range.

12 error-term model

This appendix section demonstrates 12-term error model used for calculating cal-

ibration error terms associated with 2-port measurements. The 12 error-term model signal flow graph (SFG) consists of two individual models i.e., forward model used for calculating forward error terms and reverse model for reverse error terms associated with network analyzer. The signal flow graphs for forward and reverse error models are shown in figures-(B.4) and (B.5). The forward model calculates the forward error terms and reverse model calculates reverse error terms. Thus, a total of 12-error terms are calculated by using both forward and reverse models. In final step, the calculated 12-error terms are removed from the measured data.

The other errors associated with model are directivity and cross-talk errors. The directivity error is caused by length of cables used and uncertainity between measurement ports. The directivity error causes limitation in dynamic range for reflection measurements and cross-talk error causes limitations in transmission measurement. The errors related to source and load mismatch are due to signal reflections. The source mismatch error is caused due to interactions between input and source match for device under test (DUT). The errors related to reflection and transmission tracking are due to frequency responses and imperfections at receiver system.

The signal flow graph (SFG) related to the forward and reverse models is shown in figures-(B.4) and (B.5). The error terms associated with both models are calculated by applying Masons rule. The Masons rule is applied to determine the relation between each individual nodes in calculating the error terms. The signal flow graph and equations related to forward and reverse error models by applying Masons rule are listed below [76].

Forward Model

The figure-(B.4) shows the signal flow graph related to 12-error term model which consists of six forward error terms [76]. The forward error terms associated with signal flow graph (SFG) are listed below:

e_{00}=Directivity error

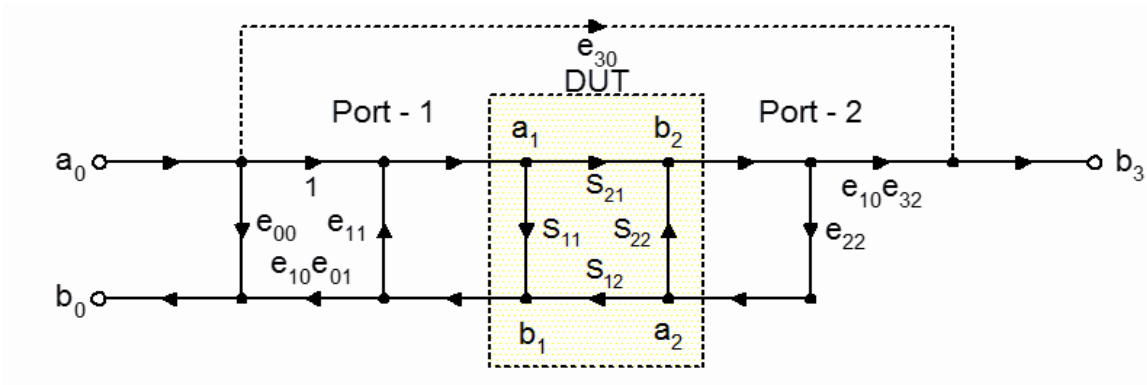

Figure B.4: Signal flow graph (SFG) for forward model associated with 12 error-terms to calculate forward error terms.

e_{11}=Error related to port-1 match

$e_{10}e_{01}$=Reflection tracking error

$e_{10}e_{32}$=Transmission tracking error

e_{22}=Error related to port-2 match

e_{30}=Leakage error

The Masons rule in equation-(B.1) is used to obtain the relationship between any two nodes in the signal flow graph (SFG) [76].

$$T = \frac{P_1\left[1 - \Sigma L_{(1)}^{(1)} + \Sigma L_{(2)}^{(1)} \cdots\right] + P_2\left[1 - L_{(1)}^{(2)} + \Sigma L_{(2)}^{(2)} \cdots\right]}{1 - \Sigma L_{(1)} + \Sigma L_{(2)}} \tag{B.1}$$

In the above equation-(B.1), 'P_1' and 'P_2' are different paths connecting the variables, $\Sigma L_{(1)}$, $\Sigma L_{(2)}$ which represents the 1st and 2nd order loops. Whereas, $\Sigma L_{(1)}{}^{(P)}$, is sum of all first order loops not touching path 'P'.

By applying Masons rule (equation-B.1) to the signal flow graph (forward model) the measurement S-parameters S_{11M} and S_{21M} are determined which contains the error terms and actual S-parameters (S_{11}, S_{21}).

At port-1 in signal flow graph (figure-B.4) it can be observed that S_{11M} provides

the relation between the incoming signal (a_0) and outgoing signal (b_0). Where, S_{11M} is the measured S-parameter realted to port-1. Therefore, we obtain

$$S_{11M}=\begin{pmatrix} b_0 \\ a_0 \end{pmatrix}$$

By applying Masons rule (equation-B.1) the relation between the two nodes a_0 and b_0 can be solved which provides the forward error terms.

In figure-(B.4) there are three paths namely P_1, P_2 and P_3 in between the nodes a_0 and b_0 described as follows.

$P_1=e_{00}$, $P_2=S_{11}e_{10}e_{01}$, $P_3=S_{21}e_{22}S_{12}e_{10}e_{01}$;

The product of 1st order loops $\Sigma L_{(1)}$ is given by

$$\Sigma L_{(1)} = S_{11}e_{11} + S_{22}e_{22} + S_{21}e_{22}S_{12}e_{11}$$

Similarly, the product of 2nd order loops $\Sigma L_{(2)}$ is given by

$$\Sigma L_{(2)} = S_{11}e_{11}S_{22}e_{22}$$

The product of First order loops not touching path-1 is given by

$$\Sigma L_{(1)}^{(1)} = S_{11}e_{11} + S_{22}e_{22} + S_{21}e_{22}S_{12}e_{11}$$

The product of first and second order loops not touching path-2 and path-3 are listed as follows.

$\Sigma\ L_{(1)}{}^{(2)}=S_{22}e_{22}$

$\Sigma\ L_{(2)}{}^{(2)}=0$

$\Sigma\ L_{(1)}{}^{(3)}=0$

$\Sigma\ L_{(2)}{}^{(3)}=0$

$\Sigma\ L_{(2)}{}^{(1)}=S_{11}e_{11}S_{22}e_{22}$

Finally, by substituting each term in equation-(B.1) for Mason's rule the measurement S-parameter (S_{11M}) can be obtained as shown below (equation-B.2).

$$S_{11M} = \frac{b_0}{a_0} = e_{00} + (e_{10}e_{01})\,\frac{S_{11} - e_{22}\Delta_s}{1 - e_{11}S_{11} - e_{22}S_{22} + e_{11}e_{22}\Delta_s} \tag{B.2}$$

Therefore, by following the same procedure the measured S-parameter S_{21M} can be derived as listed below (equation-B.3),

$$S_{21M} = \frac{b_3}{a_0} = e_{30} + (e_{10}e_{32})\,\frac{S_{21}}{1 - e_{11}S_{11} - e_{22}S_{22} + e_{11}e_{22}\Delta_s} \tag{B.3}$$

In equations (B.2) and (B.3), Δ_s=$S_{11}S_{22}$-$S_{21}S_{12}$

Reverse Model

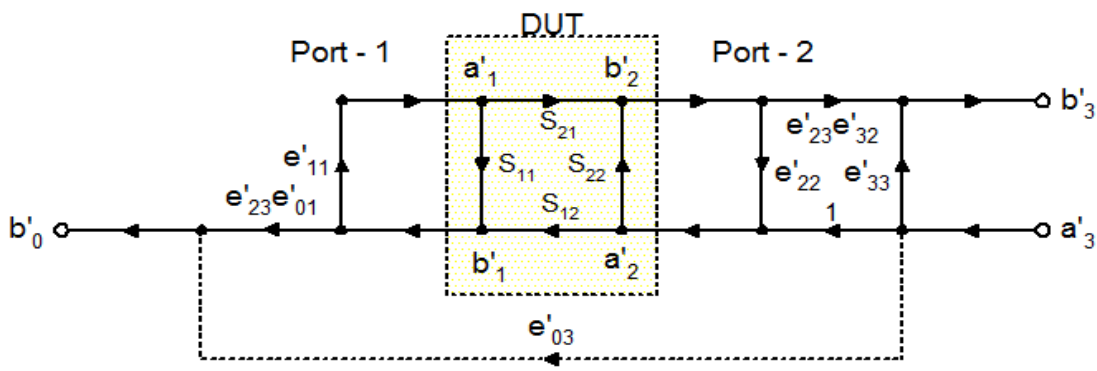

Figure B.5: Signal flow graph (SFG) for reverse model associated with 12 error-terms to calculate reverse error terms.

The signal flow graph (SFG) for the reverse model associated with reverse error terms is shown in figure-(B.5) [76]. The reverse error terms associated with reverse model are described as listed below.

e_{33}'=Directivity

$e_{23}'e_{01}'$=Transmission Tracking

e_{11}'=Port-1 Match

e_{22}'=Port-2 Match

$e_{23}'e_{32}'$=Reflection Tracking

e_{03}'=Leakage

Similarly, the measurement parameters associated with reverse model are obtained

by applying Masons rule (equation-B.1) [76]. Thus, the measurement parameters S_{22M} and S_{12M} are described as listed below.

$$S_{22M} = \frac{b_3^{'}}{a_3^{'}} = e_{33}^{'} + \left(e_{23}^{'} e_{32}^{'}\right) \frac{S_{22} - e_{11}^{'}\Delta_s}{1 - e_{11}^{'} S_{11} - e_{22}^{'} S_{22} + e_{11}^{'} e_{22}^{'} \Delta_s} \tag{B.4}$$

$$S_{12M} = \frac{b_0^{'}}{a_3^{'}} = e_{03}^{'} + \left(e_{23}^{'} e_{01}^{'}\right) \frac{S_{12}}{1 - e_{11}^{'} S_{11} - e_{22}^{'} S_{22} + e_{11}^{'} e_{22}^{'} \Delta_s} \tag{B.5}$$

In equations (B.4) and (B.5), Δ_s=$S_{11}S_{22}$-$S_{21}S_{12}$

The equations obtained for forward and reverse models contains actual S-parameters along with error terms. Therefore, a total of four equations and twelve error terms are obtained from forward and reverse models.

Thus, twelve error terms and actual device parameters can be determined by solving four equations related to S-parameter measurement obtained from forward and reverse models. In order to calculate the 12-error terms the three step procedure is followed as described below.

- **Step-1**: Calibrate port-1 using Open, Short and Load in order to obtain the error terms e_{00}, $e_{10}e_{01}$ and e_{11}.

S_{12}=S_{21}=0; for Open, Short, Load

- **Step-2**: In order to calculate the leakage current we match the load (Z_0) to port-1 which provides the leakage error terms.

S_{12}=S_{21}=S_{11}=S_{22}=0;

e_{22}=$\frac{S_{11M} - e_{00}}{S_{11M} e_{11} - \Delta_e}$

$e_{10}e_{32}$=$(S_{21M-e_{00}})\,(1 - e_{11}e_{22})$

- **Step-3**: In last step the ports 1 and 2 are connected together for Thru measurement in order to determine the remaining error terms.

S_{12}=S_{21}=1;

S_{11}=S_{22}=0

Thus, the error terms associated with both forward and reverse models can be obtained as described below.

Forward model error terms

$$e_{00} = S_{11ML} \tag{B.6}$$

$$e_{11} = \left[\frac{S_{11MO} + S_{11MS} - 2S_{11ML}}{S_{11MO} - S_{11MS}}\right] \tag{B.7}$$

$$e_{10}e_{01} = \left[\frac{2\left(S_{11ML} - S_{11MS}\right)\left(S_{11MO} - S_{11ML}\right)}{\left(S_{11MO} - S_{11MS}\right)}\right] \tag{B.8}$$

$$e_{10}e_{32} = \left[\frac{S_{11MO}^2\left(1 - S_{11M}\right)\left(S_{21M} - S_{21ML}\right)}{R}\right] + \left(\frac{2T\left(S_{11MO} - S_{11MS}\right)\left(S_{21M} - S_{21ML}\right)}{R}\right) \tag{B.9}$$

In equation-(B.9),

$$T = \left(S_{11ML}\left(S_{11MO} - S_{11MS}\right) + S_{11MS}\left(S_{11ML} - S_{11MO}\right) + S_{11ML}\left(S_{11M} - S_{11ML}\right)\right)$$

$$R = \left(S_{11MO} - S_{11MS}\right)\left(S_{11M} + S_{11ML}\right)\left(S_{11MO} + S_{11MS}\right) - 2S_{11MS}S_{11ML} - 2S_{11M}S_{11MO}$$

$$e_{22} = \left[\frac{2\left(S_{11M} - S_{11ML}\right)\left(S_{11MO} - S_{11MS}\right)}{\left(S_{11M} + S_{11ML}\right)\left(S_{11MO} + S_{11MS}\right) - 2S_{11M}S_{11ML} - 2S_{11M}S_{11MO}}\right] \tag{B.10}$$

In the above listed equations (B.6)-(B.10) the forward error terms corresponding to forward model we have, S_{11MS} as S_{11M} Short, S_{11MO} as S_{11M} Open and S_{11ML} as S_{11M} Load.

In last step we substitute all error terms in equations to determine the actual device parameters. Therefore, the actual S-parameters are described as listed in equations (B.11)-(B.14).

$$S_{11} = \frac{\left(\frac{S_{11M} - e_{00}}{e_{10}e_{01}}\right)\left[1 + \left(\frac{S_{22M} - e_{33}^{'}}{e_{23}^{'}e_{32}^{'}}\right)e_{22}^{'}\right] - e_{22}\left(\frac{S_{21M} - e_{30}}{e_{10}e_{32}}\right)\left(\frac{S_{21M} - e_{03}^{'}}{e_{23}^{'}e_{01}^{'}}\right)}{D} \tag{B.11}$$

$$S_{21} = \frac{\left(\frac{S_{21M} - e_{30}}{e_{10}e_{32}}\right)\left[1 + \left(\frac{S_{22M} - e_{33}^{'}}{e_{23}^{'}e_{32}^{'}}\right)\left(e_{22}^{'} - e_{22}\right)\right]}{D} \tag{B.12}$$

$$S_{22} = \frac{\left(\frac{S_{22M}-e_{33}^{'}}{e_{23}^{'}e_{32}^{'}}\right)\left[1+\left(\frac{S_{11M}-e_{00}}{e_{10}e_{01}}\right)e_{11}\right] - e_{11}^{'}\left(\frac{S_{21M}-e_{30}}{e_{10}e_{32}}\right)\left(\frac{S_{21M}-e_{03}^{'}}{e_{23}^{'}e_{01}^{'}}\right)}{D} \tag{B.13}$$

$$S_{12} = \frac{\left(\frac{S_{21M}-e_{03}^{'}}{e_{23}^{'}e_{01}^{'}}\right)\left[1+\left(\frac{S_{11M}-e_{00}}{e_{10}e_{01}}\right)\left(e_{11}-e_{11}^{'}\right)\right]}{D} \tag{B.14}$$

In the above equations (B.11)-(B.14), we have

$$D = \left[1+\left(\frac{S_{11M}-e_{00}}{e_{10}e_{01}}\right)e_{11}\right]\left[1+\left(\frac{S_{22M}-e_{33}^{'}}{e_{23}^{'}e_{32}^{'}}\right)e_{22}^{'}\right] - \left(\frac{S_{21M}-e_{30}}{e_{10}e_{32}}\right)\left(\frac{S_{12M}-e_{03}^{'}}{e_{23}^{'}e_{01}^{'}}\right)e_{22}e_{11}^{'}$$

In measurements the actual parameters of the DUT are obtained by considering four independent measurement structures such as Short, Open, Load and Thru on the impedance calibration substrate. During performing each individual measurement for Open, Short and Load the interference's from port-2 (S_{12}=S_{21}=0) are avoided while calculating the error terms for port-1. Similarly, while performing the measurement for Load calibration, the Load (Z_0) is set equal to characteristic impedance of the system i.e., 50Ω. In addition, the condition S_{11}=S_{22}=0 is applied in order to calculate the leakage error term. The measurement for Thru structure is performed by combining both ports 1 and 2 as S_{12}=S_{21}=1 which gives all the remaining error terms. Thus, the 12-term error model described in this section of appendix can be used for calculating the error terms theoretically and also to obtain actual measured (DUT) parameters. Thus, the described 12-error term model can be used for calculating error terms and extracting the actual device parameters mathematically which are related to practical measurements.

Scattering Parameters

At r-f or high frequencies the Kirchoff laws for calculating the currents and voltages cannot be applicable as they do not consider the influence of electric and magnetic fields. Based on boundary condition the wavelength (λ) is much smaller than the device dimensions. Thus, the difficulty arises during 2-port measurement which effects the measurement accuracy due to influence of r-f probes and bi-directional path of waves. Therefore, measurement of scattering (S-parameters) parameters provides

solution to this problem. The S-parameters provides information related to gain, reflection and loss corresponding to incident and reflected waves. The information related to S-parameters data can be recorded on network analyzer and can be verified using smith chart or magnitude (dB) and phase plots.

The S-parameter matrix corresponding to 2-port measurement system is described as follows.

$$S = \begin{bmatrix} S_{11} & S_{12} \\ S_{21} & S_{22} \end{bmatrix}$$

The information stated in S-parameter matrix can be measured using vector network analyzer (VNA) and verified using smith chart results. The signal flow graph corresponding to 2-port network is shown in figure-(B.6).

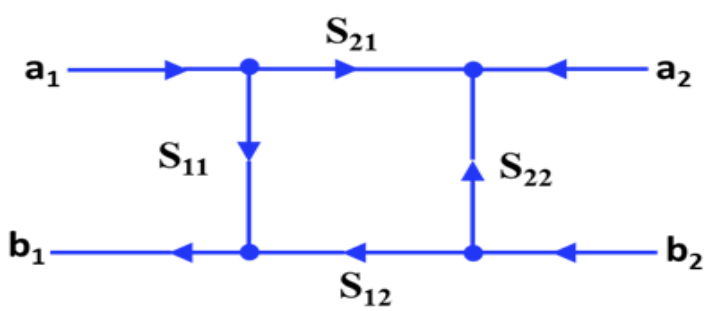

Figure B.6: Signal flow graph (SFG) of S-parameter 2-port network.

$$\begin{pmatrix} b_1 \\ b_2 \end{pmatrix} = \begin{pmatrix} S_{11} & S_{12} \\ S_{21} & S_{22} \end{pmatrix} = \begin{pmatrix} a_1 \\ a_2 \end{pmatrix}$$

De-embedding

The de-embedding procedure is applied following the calibration and device measurements in order to obtain accurate and reliable measurement data. In general, the most widely used de-embedding methods are Open and Short which uses Open or Short structure. In this work a simple Thru de-embedding method is used which

makes use of Thru device structure. The main purpose of carrying out de-embedding procedure is it removes measurement uncertainities and parasitic effects at high frequencies caused by bond pads and interconnects between bond pads and device (DUT).

The Open-Short de-embedding method is most accurate when dealing with low frequencies but at high frequencies (r-f) a simple Thru de-embdedding structure is highly recommended to avoid complexities. The Thru de-embedding is most desirable method at high frequencies because it takes into account contact resistance between r-f probes and contact pads. In addition, the contact pads on wafer makes use of different materials for layers which adds extra contact resistance. Thus, the resistance and reactance losses between interconnects needs to be considered and removed at r-f frequency measurements.

The de-embedding method is used to extract the actual device (DUT) characteristics from measurements. The de-embedding method for Thru structure is carried out by considering the reflection symmetry on Thru pattern i.e., left and right sides of the DUT. Therefore, Thru structure can be split into two symmetrical halves known as error boxes shown in figure-(B.7). By obtaining the scattering matrices for each error boxes the effects related to bond pads and probes can be eliminated from the measurements. Thus, the results of actual device parameter (DUT) can be extracted.

The de-embedding procedure described in this section can be applicable at r-f (or) high frequencies for device characterization on-chip. The results obtained from Thru de-embedding method are consistent with Open-Short de-embedding procedure. Therefore, parasitic effects related to bond pads and interconnects on device can be removed by means of de-embedding. Thus, thru de-embedding method is proved to be accurate and simple to implement by inserting a device under test (DUT) in between the error boxes. The error boxes shown in figure-(B.7) are assumed to be symmetrical. In addition, simple Thru de-embedding technique can be mathematically verified and

preferred when dealing with lumped elements at high frequecies.

The signal flow graph (SFG) for Thru de-embedding is shown in figure-(B.7). The Masons rule (equation-B.1) is applied to obtain S-parameters for each error box. Lastly, the obtained scattering parameters are subtracted from the combined S-parameters to extract the actual device parameters (DUT).

The Thru de-embedding procedure can be described as follows.

$$S_{Meas}=S_A S_{DUT} S_B$$

$$S_{Thru}=S_A S_B$$

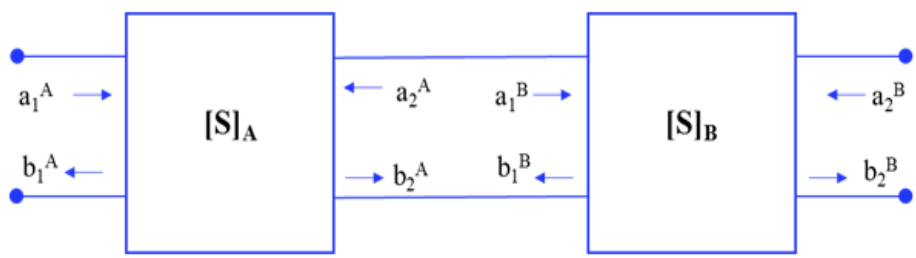

Figure B.7: Signal flow graph (SFG) for Thru de-embedding structure.

From the above signal flow graph (SFG) for Thru de-embedding method we have,

$$a_2=b_3;\ b_2=a_3$$

$$\begin{pmatrix} b_1 \\ b_2 \end{pmatrix} = \begin{pmatrix} S_{11}^A & S_{12}^A \\ S_{21}^A & S_{22}^A \end{pmatrix} = \begin{pmatrix} a_1 \\ a_2 \end{pmatrix}$$

$$\begin{pmatrix} b_3 \\ b_4 \end{pmatrix} = \begin{pmatrix} S_{11}^B & S_{12}^B \\ S_{21}^B & S_{22}^B \end{pmatrix} = \begin{pmatrix} a_1 \\ a_2 \end{pmatrix}$$

$$\begin{pmatrix} b_1 \\ b_4 \end{pmatrix} = \begin{pmatrix} S_{11} & S_{12} \\ S_{21} & S_{22} \end{pmatrix} = \begin{pmatrix} a_1 \\ a_4 \end{pmatrix}$$

By solving matrices described above we have,

$$S_{11} = \left[\frac{S_{11}^{A} + S_{11}^{B}\Delta_{A}}{1 - S_{11}^{B}S_{22}^{A}}\right] \tag{B.15}$$

$$S_{21} = \left[\frac{S_{21}^{A}S_{21}^{B}}{1 - S_{11}^{B}S_{22}^{A}}\right] \tag{B.16}$$

$$S_{22} = \left[\frac{S_{22}^{B} + S_{22}^{B}\Delta_{B}}{1 - S_{11}^{B}S_{22}^{A}}\right] \tag{B.17}$$

$$S_{12} = \left[\frac{1 - S_{11}^{A^2}}{S_{11}^{A^2}}\right] \tag{B.18}$$

It is assumed that $[S]_A$ and $[S]_B$ are symmetrical therefore we obtain,

$$\mathrm{S}_{11}{}^{A}{=}\mathrm{S}_{22}{}^{A},\ \ \mathrm{S}_{12}{}^{A}{=}\mathrm{S}_{21}{}^{A},\ \ \mathrm{S}_{11}{}^{B}{=}\mathrm{S}_{22}{}^{B},\ \S_{12}{}^{B}{=}\mathrm{S}_{21}{}^{B}$$

It is also assumed that $[S]_A$ and $[S]_B$ are bi-sectional symmetrical to each other regarding $[S]_B$, and then port-1 is $\begin{pmatrix} b_4 \\ b_3 \end{pmatrix}$ while port-2 is $\begin{pmatrix} b_3 \\ a_3 \end{pmatrix}$.

$$\begin{pmatrix} b_4 \\ b_3 \end{pmatrix} = \begin{pmatrix} S_{22}^{B} & S_{21}^{B} \\ S_{12}^{B} & S_{11}^{B} \end{pmatrix} = \begin{pmatrix} a_4 \\ a_3 \end{pmatrix}$$

Therefore, we obtain

$$S_{12} = S_{21} = \left[\frac{S_{21}^{A^2}}{1 - S_{11}^{A^2}}\right] \tag{B.19}$$

$$S_{22} = S_{11} = \left[\frac{S_{11}^{A} + S_{11}^{A}\Delta_{A}}{1 - S_{11}^{A^2}}\right] \tag{B.20}$$

Thus, the actual Scattering parameters for device (DUT) can be extracted by following the described de-embedding procedure.

APPENDIX C

Introduction to Green's function

The Green's function is named after physicist George Green (1793-1841) for solving boundary problems [70]. The general method for solving Poisson's equation and total potential was developed by Green [70]. By considering theory of electricity the potential of point charge located at '$\vec{r}$' is given by (equation-C.1) [70]

$$\vec{\phi_1}\left(\vec{r}\right) = \frac{q_1}{4\pi\epsilon\left|\vec{r} - \vec{r_1}\right|} \tag{C.1}$$

In equation-(C.1), $|\vec{r} - \vec{r_1}|$ is distance between points '$\vec{r}$' and '$\vec{r_1}$'. Where, 'ϵ' is permittivity of medium.

If point charge (q_2) is placed at location '$\vec{r_2}$', then potential calculated by this point charge 'q_2' is given by (equation-C.2) [64, 70]

$$\vec{\phi_2}\left(\vec{r}\right) = \frac{q_2}{4\pi\epsilon\left|\vec{r} - \vec{r_2}\right|} \tag{C.2}$$

Therefore, total potential of point charges 'q_1' and 'q_2' given by potentials 'ϕ_1' and 'ϕ_2' is described in equation-(C.3) [70].

$$\phi\left(\vec{r}\right) = \vec{\phi_1}\left(\vec{r}\right) + \vec{\phi_1}\left(\vec{r}\right) = \frac{q_1}{4\pi\epsilon\left|\vec{r} - \vec{r_1}\right|} + \frac{q_2}{4\pi\epsilon\left|\vec{r} - \vec{r_2}\right|} \tag{C.3}$$

In case, if there are 'N' point charges located in space, then total potential '$\phi\left(\vec{r}\right)$'

can be calculated by equation-(C.4) [70].

$$\phi\left(\vec{r}\right) = \sum_{i=1}^{N} \phi_i\left(\vec{r}\right) = \sum_{i=1}^{N} \frac{q_i}{4\pi\epsilon\left|\vec{r} - \vec{r_i}\right|} \tag{C.4}$$

In equation-(C.4), 'Σ' is sum of all point charges and 'ϕ_i' is potential of ith point charge located at '$\vec{r_i}$' [70].

The electric potential of volume charge with charge density $\rho\left(\vec{r}\right)$ [70]. The potential is calculated by dividing volume charge into cubes and charge in each cube is given by (equation-C.5) [70]

$$q_i \approx \rho\left(\vec{r_i}\right) \triangle V_i \tag{C.5}$$

In equation-(C.5), '$\vec{r_i}$' is center of cube and $\triangle V_i$ is volume of cube [70]. The size of cube is small therefore, it is approximated as point charge given by [70].

$$\phi_i\left(\vec{r}\right) \approx \frac{q_i}{4\pi\epsilon\left|\vec{r} - \vec{r_i}\right|} \approx \frac{\rho\left(\vec{r_i}\right) \triangle V_i}{4\pi\epsilon\left|\vec{r} - \vec{r_i}\right|} \tag{C.6}$$

By using principle of superposition the total potential is given by (equation-C.7) [70].

$$\phi_i\left(\vec{r}\right) = \sum_{i=1}^{N} \phi_i\left(\vec{r}\right) \approx \sum_{i=1}^{N} \frac{\rho\left(\vec{r_i}\right) \triangle V_i}{4\pi\epsilon\left|\vec{r} - \vec{r_i}\right|} \tag{C.7}$$

The limit when $\triangle V_i \to 0$ the above expression (equation-C.7) becomes exact [70]. Therefore, we obtain (equation-C.8) [70],

$$\phi_i\left(\vec{r}\right) = \lim_{\triangle V_i \to 0} \sum_{i=1}^{\infty} \frac{\rho\left(\vec{r_i}\right) \triangle V_i}{4\pi\epsilon\left|\vec{r} - \vec{r_i}\right|} \tag{C.8}$$

The expression equation-(C.8) in integral form is given by equation-(C.9) [70]

$$\phi\left(\vec{r}\right) = \iiint_V \frac{\rho\left(\vec{r_i}\right) dV'}{4\pi\epsilon\left|\vec{r} - \vec{r'}\right|} \tag{C.9}$$

In equation-(C.9), 'V' is volume of charge [70].

The potential produced by unit point source of unit strength is called Green's function [70]. The Green's function is given by equation-(C.10) [70],

$$G\left(\vec{r},\vec{r'}\right)=\frac{1}{4\pi\epsilon\left|\vec{r}-\vec{r'}\right|} \tag{C.10}$$

In equation-(C.10), '$\vec{r}$' is location of point where potential is calculated based on point charge located at position $\vec{r'}$ and observation point $\vec{r}$ [70].

The total potential is given by equation-(C.11) [70]

$$\phi\left(\vec{r}\right)=\iiint\limits_{V}\rho\left(\vec{r'}\right)G\left(\vec{r},\vec{r'}\right)dV' \tag{C.11}$$

Mathematical Representation of Point Source

The Green's function $G\left(\vec{r},\vec{r'}\right)$ in mathematical form is described as follows [70].

Consider charge of unit strength located at point '$\vec{r'}$' [70]. When volume of charge is zero then charge density can be described by function [70]

$$\delta\left(\vec{r}-\vec{r'}\right)=\begin{matrix}\infty & \vec{r}=\vec{r'}\\ 0 & \vec{r}\neq\vec{r'}\end{matrix}$$

If total charge is at unity [69], we obtain

$$\iiint_V\delta\left(\vec{r}-\vec{r'}\right)dV=\begin{matrix}1 & \vec{r}=\vec{r'}\\ 0 & \vec{r}\neq\vec{r'}\end{matrix}$$

The function $\delta\left(\vec{r}-\vec{r'}\right)$ in above expression is known as Dirac delta function [70].

The magneto-static Poisson's equation is given by [70]

$$\nabla^2\phi_m=\rho_m$$

The solution of Poisson's equation using Green's function is as follows (equation-

C.12) [70].

$$\phi_m\left(\vec{r}\right) = -\iiint\limits_V \left(\bigtriangledown' \bullet \vec{m}\left(\vec{r'}\right)\right) G\left(\vec{r}, \vec{r'}\right) dV' \tag{C.12}$$

In equation-(C.12), $\vec{m}\left(\vec{r'}\right)$ is magnetization vector at point source, $\bigtriangledown' = \left(\partial_{x'}, \partial_{y'}\right)$ is gradient of point source and $G\left(\vec{r}, \vec{r'}\right)$ is free-space scalar Green's function [70].

If net charge density is zero then we have (equation-C.13) [70],

$$\bigtriangledown \bullet \vec{j} = 0 \tag{C.13}$$

By considering that current has no divergence and there are no normal components on surface 'S' we obtain (equation-C.14) [70],

$$\oint\limits_S \vec{j} \bullet d\vec{S} = 0 \tag{C.14}$$

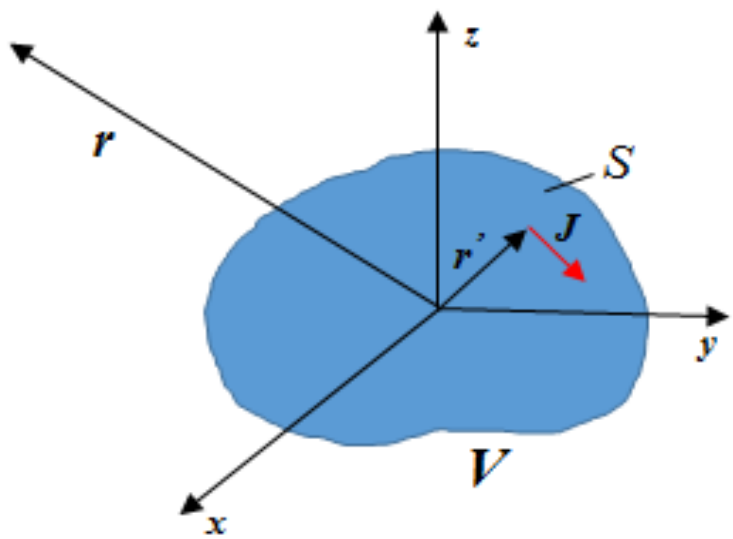

Figure C.1: Representation of current density across surface

The microscopic magnetization density is given by (equation-C.15) [70],

$$\vec{m} = \vec{r} \times \vec{j} \tag{C.15}$$

$$\oint_S \vec{m} \bullet d\vec{S} = 0 \tag{C.16}$$

By applying divergence theorem we have [70],

$$\iint_V \bigtriangledown \bullet \left(G\left(\vec{r}, \vec{r'}\right) \vec{m}\left(\vec{r'}\right)\right) = \oint_{S'} G\left(\vec{r}, \vec{r'}\right) \vec{m}\left(\vec{r'}\right) dS' = 0 \tag{C.17}$$

$$\iint_V \bigtriangledown \bullet \left(G\left(\vec{r}, \vec{r'}\right) \vec{m}\left(\vec{r'}\right)\right) = 0 \tag{C.18}$$

Therefore, by applying vector properties we have [70],

$$\iint_V \bigtriangledown \bullet \left(G\left(\vec{r}, \vec{r}\right) \vec{m}\left(\vec{r'}\right)\right) = \iint_V \bigtriangledown G\left(\vec{r}, \vec{r'}\right) \bullet \vec{m}\left(\vec{r'}\right) + G\left(\vec{r}, \vec{r'}\right)\left(\bigtriangledown \bullet \vec{m}\left(\vec{r'}\right)\right) \tag{C.19}$$

$$\iint_V \bigtriangledown G\left(\vec{r}, \vec{r'}\right) \bullet \vec{m}\left(\vec{r'}\right) + G\left(\vec{r}, \vec{r'}\right)\left(\bigtriangledown \bullet \vec{m}\left(\vec{r'}\right)\right) = 0 \tag{C.20}$$

$$\iint_V \bigtriangledown' G\left(\vec{r}, \vec{r'}\right) \bullet \vec{m}\left(\vec{r'}\right) = \iint_V -G\left(\vec{r}, \vec{r'}\right)\left(\bigtriangledown' \bullet \vec{m}\left(\vec{r'}\right)\right) \tag{C.21}$$

$$\phi_m\left(\vec{r}\right) = \int_{V'} \bigtriangledown' G\left(\vec{r}, \vec{r'}\right) \bullet \vec{m}\left(\vec{r'}\right) dV' \tag{C.22}$$

$$\phi_m\left(\vec{r}\right) = \int_{V'} \bigtriangledown' G\left(\vec{r}, \vec{r'}\right) \bullet \vec{m}\left(\vec{r'}\right) dx' dy' dz' \tag{C.23}$$

Integrating the above equation-(C.23) along the length (l) i.e., z-axis we have

$$\int_0^l dz' \phi_m\left(\vec{r}\right) dx' dy' = \int_0^l dz' \int_{dS'} \bigtriangledown' G\left(\vec{r}, \vec{r'}\right) \bullet \vec{m}\left(\vec{r'}\right) dx' dy' \tag{C.24}$$

$$\phi_m(\vec{r}) = \int_{S'} \bigtriangledown' G\left(\vec{r}, \vec{r'}\right) \bullet \vec{m}\left(\vec{r'}\right) dS' \tag{C.25}$$

The above equation-(C.25) is known as the general solution of magneto-static Poisson's equation.

In equation-(C.25), $\vec{r} = (x, y)$ is location of observation point, $\vec{r'} = \left(x', y'\right)$ is location of point source, $\bigtriangledown = (\partial_x, \partial_y)$ is gradient of observation point and $\bigtriangledown' = \left(\partial_{x'}, \partial_{y'}\right)$ is gradient of point source [70].

By using $\vec{h} = -\bigtriangledown \phi_m$ in above equation-(C.25) we obtain equation-(C.26) [70],

$$h_m(\vec{r}) = -\bigtriangledown \int_{S'} \bigtriangledown' G\left(\vec{r}, \vec{r'}\right) \bullet \vec{m}\left(\vec{r'}\right) dS' \tag{C.26}$$

Therefore, Greens function is given by,

$$G\left(\vec{r}, \vec{r'}\right) = -\tfrac{1}{2\pi} ln \left|\vec{r} - \vec{r'}\right|$$

The free-space scalar Green's function in equation-(C.26) for two-dimensional (2-D) and three dimensional (3-D) case can be derived by using one of the following cases below [70]:

Derivation of Free-Space Scalar Green's function

Case-1: 2-Dimensional (2D) free-space Green's function

In order to solve Green's function consider wave function (ϕ) satisfying inhomogeneous Helmholtz equation given by equation-(C.27) [70].

$$\bigtriangledown^2 \phi(\vec{r}) + k^2 \phi(\vec{r}) = -f(\vec{r}) \tag{C.27}$$

In equation-(C.27), '$\phi(\vec{r})$' propagates in infinite free-space where there are no reflected waves [70],

Therefore, wave function ($\phi(\vec{r})$) satisfies radiation condition given in equation-

(C.28) [70]

$$r\left(\frac{\partial\phi}{\partial r}+jk\phi\right)=0; r\rightarrow\infty \tag{C.28}$$

Radiation Condition: When outer boundary of domain is located at infinity then domain is called unbounded or open [70]. The radiation condition is specified at this outer boundary located at infinity for obtaining unique solution to problem [70].

By assuming that all sources and objects are located in free-space within finite distance from origin of co-ordinate system [70]. Therefore, electric and magnetic fields satisfies condition listed in equation-(C.29) [70].

$$\lim_{r\rightarrow\infty} r\left[\bigtriangledown\times\begin{pmatrix}E\\H\end{pmatrix}+jk_o\hat{r}\times\begin{pmatrix}E\\H\end{pmatrix}\right]=0 \tag{C.29}$$

The equation-(C.29) is known as Sommerfeld radiation condition for general three-dimensional (3D) fields [70]. Where, $r=\sqrt{x^2+y^2+z^2}$

The Green's function is obtained by solving partial differential equation (equation-C.30) [70]

$$\bigtriangledown^2 G\left(\vec{r},\vec{r_o}\right)+k^2 G\left(\vec{r},\vec{r_o}\right)=-\delta\left(\vec{r}-\vec{r_o}\right) \tag{C.30}$$

Therefore, potential $(\phi\left(\vec{r}\right))$ in equation-(C.27) is replaced by Green's function '$G\left(\vec{r},\vec{r_o}\right)$' in equation-(C.30) [70].

In figure-(C.2), consider a point source located at 'Q' which is represented by space vector '$\vec{r_o}$' with reference to origin and observation point located at point 'P' represented by space vector '$\vec{r}$' with reference to origin in xyz-plane.

Therefore, Green's function satisfies inhomogeneous wave equation listed below [70],

$$\bigtriangledown^2 G\left(\vec{r},\vec{r_o}\right)+k^2 G\left(\vec{r},\vec{r_o}\right)=-\delta\left(\vec{r}-\vec{r_o}\right)$$

The Green's function can be derived as follows [70].

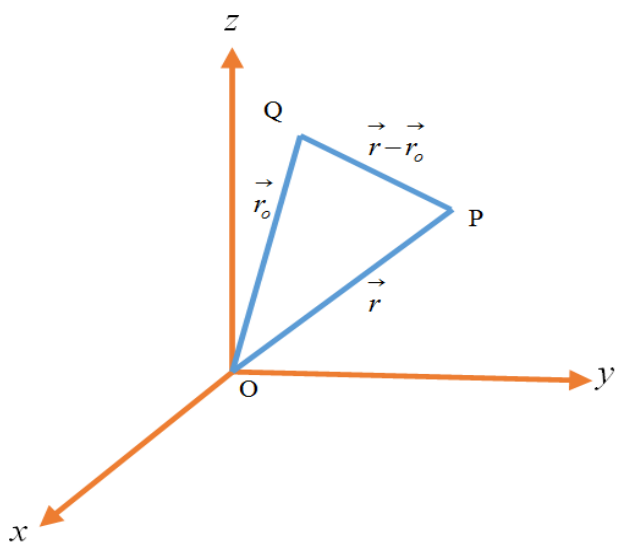

Figure C.2: Representation of point source 'Q' and observation point 'P' with reference to origin in xyz plane

Consider point charge of unit strength located at point '$\vec{r_0}$'. When volume of charge is zero then charge density is described by [70]

$$\delta\left(\vec{r}-\vec{r_o}\right)=\begin{matrix}\infty & \vec{r}=\vec{r_o}\\ 0 & \vec{r}\neq\vec{r_o}\end{matrix}$$

Since, total charge is unity, we have [70]

$$\iiint_V \delta\left(\vec{r}-\vec{r_o}\right)dV=\begin{matrix}1 & \vec{r_o}\ in\ V\\ 0 & r_o\ \vec{\notin}\ V\end{matrix}$$

In case, when point source and observation point are at different locations i.e., $\delta\left(\vec{r}-\vec{r_o}\right)=0$ when $\vec{r}\neq\vec{r_o}$ and $\iiint_V \delta\left(\vec{r}-\vec{r_o}\right)dV=1$ for $\vec{r_o}$ enclosed by volume 'V' [70].

(a): Static case (k=0):

For static case k=0 is substituted in equation-(C.30)

$$\bigtriangledown^2 G\left(\vec{r},\vec{r_o}\right)=-\delta\left(\vec{r}-\vec{r_o}\right) \tag{C.31}$$

In order to solve Green's function '$G\left(\vec{r},\vec{r_o}\right)$' in equation-(C.31) for static case

(k=0) a new co-ordinate system is introduced with its origin located at point '$\vec{r_o}$' i.e., $\vec{r_1} = \vec{r} - \vec{r_o}$ [70].

$$\bigtriangledown^2 G\left(\vec{r_1}, 0\right) = -\delta\left(\vec{r_1} - 0\right) \tag{C.32}$$

In equation-(C.32), $\bigtriangledown^2 G\left(\vec{r_1}, 0\right) = \frac{1}{r_1^2}\frac{d}{dr_1}\left[r_1^2 \frac{dG(\vec{r_1},0)}{dr_1}\right]$ from symmetry of spherical co-ordinates. Therefore we have [70]

$$\frac{1}{r_1^2}\frac{d}{dr_1}\left[r_1^2 \frac{dG\left(\vec{r_1}, 0\right)}{dr_1}\right] = -\delta\left(\vec{r_1} - 0\right) \tag{C.33}$$

From symmetry property we have,

$$\frac{1}{r_1^2}\frac{d}{dr_1}\left[r_1^2 \frac{dG\left(\vec{r_1}, 0\right)}{dr_1}\right] \cong \frac{1}{r_1}\frac{\mathrm{d}^2}{\mathrm{d}r_1^2}\left[r_1 G\left(\vec{r_1}, 0\right)\right] \tag{C.34}$$

$$\bigtriangledown^2 G\left(\vec{r_1}, 0\right) = \frac{1}{r_1}\frac{d}{dr_1}\left[r_1 \frac{dG\left(\vec{r_1}, 0\right)}{dr_1}\right] \tag{C.35}$$

By substituting the above expression for 'G' in equation-(C.32) and using $\delta\left(\vec{r_1} - 0\right) = 0$ when $\vec{r} \neq \vec{r_o}$ we obtain

$$\frac{1}{r_1}\frac{d}{dr_1}\left[r_1 \frac{dG\left(\vec{r_1}, 0\right)}{dr_1}\right] = 0 \tag{C.36}$$

The derivative of constant function is zero. Therefore, from equation-(C.36) we have,

$$r_1 \frac{dG\left(\vec{r_1}, 0\right)}{dr_1} = const = C \tag{C.37}$$

$$\frac{dG\left(\vec{r_1}, 0\right)}{dr_1} = \frac{C}{r_1} \tag{C.38}$$

By integrating both sides with respect to 'r_1' we obtain,

$$\int \frac{dG\left(\vec{r_1}, 0\right)}{dr_1} dr_1 = \int \frac{C}{r_1} dr_1 \tag{C.39}$$

$$G\left(\vec{r_1}, 0\right) = C ln\left|r_1\right| + M \tag{C.40}$$

In order to determine arbitrary constant 'C' in equation-(C.40) the equation-(C.34) is integrated over entire volume on both sides as shown below [70]

$$\iint_V \bigtriangledown^2 G\left(\vec{r_1}, 0\right) dV = \iint_V -\delta\left(\vec{r_1}, 0\right) dV \tag{C.41}$$

$$\iint_V \bigtriangledown \cdot \bigtriangledown G\left(\vec{r_1}, 0\right) dV = \iint_V -\delta\left(\vec{r_1}, 0\right) dV \tag{C.42}$$

When $\vec{r} \neq \vec{r_o}$ then $\iiint_V \bigtriangledown \cdot \bigtriangledown G\left(\vec{r_1}, 0\right) dV = -1$ from mathematical representation, therefore we have [70]

$$\iiint_V \bigtriangledown \cdot \bigtriangledown G\left(\vec{r_1}, 0\right) dV = -1 \tag{C.43}$$

Divergence Theorem

The divergence theorem states that, for any arbitrary vector $\bigtriangledown G\left(\vec{r_1}, 0\right)$, the closed surface integral of normal component of vector $\bigtriangledown G\left(\vec{r_1}, 0\right)$ over surface 'S' is equal to volume integral of divergence of $\bigtriangledown G\left(\vec{r_1}, 0\right)$ over volume 'V' enclosed by 'S' [69].

The divergence theorem in mathematical form can be represented as shown in equation-(C.44) [69]

$$\iint_V \bigtriangledown \cdot \bigtriangledown G\left(\vec{r_1}, 0\right) dV = \iint_S \bigtriangledown G\left(\vec{r_1}, 0\right) \cdot dS \tag{C.44}$$

By applying Divergence theorem (equation-C.44) to above expression we obtain

$$\int_0^{2\pi} \int_0^{r_1} \bigtriangledown G\left(\vec{r_1}, 0\right) \cdot dS = -1 \tag{C.45}$$

$$\int_0^{2\pi} \int_0^{r_1} \frac{C}{r_1} \left(R d\theta\right) = -1 \tag{C.46}$$

Since r_1=R we have,

$$\int_0^{2\pi} C d\theta = -1 \tag{C.47}$$

$$C = -\tfrac{1}{2\pi}$$

By substituting value of arbitrary constant 'C' in equation-(C.40) we obtain two-dimensional (2D) Greens function as shown in equation-(C.49) [70]

$$G\left(\vec{r_1}, 0\right) = -\frac{1}{2\pi} ln \left|\vec{r_1}\right| \tag{C.48}$$

$$G\left(\vec{r}, \vec{r_o}\right) = -\frac{1}{2\pi} ln \left|\vec{r} - \vec{r_o}\right| \tag{C.49}$$

Since, $\vec{r_1} = \vec{r} - \vec{r_o}$

(b): Case when k≠0

For case when $k \neq 0$ we have from equation-(C.30)

$$\bigtriangledown^2 G\left(\vec{r}, \vec{r_o}\right) + k^2 G\left(\vec{r}, \vec{r_o}\right) = -\delta\left(\vec{r} - \vec{r_o}\right) \tag{C.50}$$

In order to solve for Greens function in equation-(C.50) when k≠0 a new co-ordinate system is introduced with origin located at point '$\vec{r_o}$' i.e., $\vec{r_1} = \vec{r} - \vec{r_o}$. Therefore, we obtain equation-(C.51) [70]

$$\bigtriangledown^2 G\left(\vec{r_1}, 0\right) + k^2 G\left(\vec{r_1}, 0\right) = -\delta\left(\vec{r_1} - 0\right) \tag{C.51}$$

In equation-(C.51), $\bigtriangledown^2 G\left(\vec{r_1}, 0\right) = \frac{1}{r_1^2}\frac{d}{dr_1}\left[r_1^2 \frac{dG(\vec{r_1},0)}{dr_1}\right]$ from symmetry of spherical co-ordinates

$$\frac{1}{r_1^2}\frac{d}{dr_1}\left[r_1^2 \frac{dG\left(\vec{r_1}, 0\right)}{dr_1}\right] + k^2 G\left(\vec{r_1}, 0\right) = -\delta\left(\vec{r_1} - 0\right) \tag{C.52}$$

By applying symmetry property we have,

$$\frac{1}{r_1^2}\frac{d}{dr_1}\left[r_1^2\frac{dG\left(\vec{r_1},0\right)}{dr_1}\right]\cong\frac{1}{r_1}\frac{d^2}{dr_1^2}\left[r_1G\left(\vec{r_1},0\right)\right] \tag{C.53}$$

$$\frac{1}{r_1}\frac{d}{dr_1}\left[r_1\frac{dG\left(\vec{r_1},0\right)}{dr_1}\right]+k^2G\left(\vec{r_1},0\right)=-\delta\left(\vec{r_1}-0\right) \tag{C.54}$$

$$\frac{1}{r_1}\frac{d}{dr_1}\left[r_1\frac{dG\left(\vec{r_1},0\right)}{dr_1}\right]+k^2G\left(\vec{r_1},0\right)=-1 \tag{C.55}$$

The solution of equation-(C.55) is of form $G\left(\vec{r_1},0\right)=Ae^{-jk\vec{r_1}}$ from wave equation

$$\frac{1}{r_1}\frac{\partial}{\partial r_1}\left[r_1\frac{\partial}{\partial r_1}\left[Ae^{-jk\vec{r_1}}\right]\right]+k^2Ae^{-jk\vec{r_1}}=-1 \tag{C.56}$$

$$\frac{1}{r_1}\frac{\partial}{\partial r_1}\left[r_1Ae^{-jk\vec{r_1}}\left(-jk\right)\right]+k^2Ae^{-jk\vec{r_1}}=-1 \tag{C.57}$$

$$\frac{1}{r_1}A\left(-jk\right)\left\{e^{-jk\vec{r_1}}\left(-jk\right)\frac{d\left|\vec{r_1}\right|}{dr_1}r_1+e^{-jk\vec{r_1}}\frac{d\left|\vec{r_1}\right|}{dr_1}\right\}+k^2Ae^{-jk\vec{r_1}}=-1 \tag{C.58}$$

$$\int_0^r\frac{1}{r_1}A\left(-jk\right)e^{-jk\vec{r_1}}\frac{d\left|\vec{r_1}\right|}{dr_1}\left[\left(-jk\right)\vec{r_1}+1\right]rdr+\int_0^r k^2Ae^{-jk\vec{r_1}}rdr=-\frac{1}{\pi} \tag{C.59}$$

In above expression $\left(-jkr_1\right)=0\ \ and\ \ k^2Ae^{-jk\vec{r_1}}r=0$

The figure-(C.3) shows the plots of function $\left|\vec{r}\right|$ and its derivative $\frac{d\left|\vec{r}\right|}{dr}$.

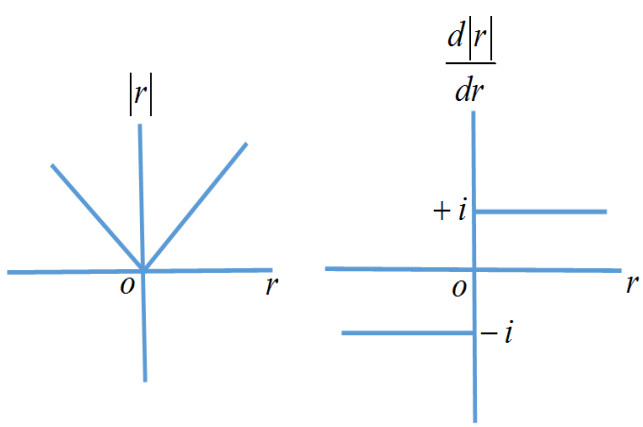

Figure C.3: Plots of function $\left|\vec{r}\right|$ and its derivative $\frac{d\left|\vec{r}\right|}{dr}$

In figure-(C.3), we have

$$\left|\frac{d\left|\vec{r_1}\right|}{dr_1}\right|_{r_1\to 0^-}^{r_1\to 0^+} = 2 \tag{C.60}$$

Therefore,

$$\int_0^r A\left(-jk\right)e^{-jk\vec{r_1}}\frac{d\left|\vec{r_1}\right|}{dr_1}\left[1\right]dr = -\frac{1}{\pi} \tag{C.61}$$

$$A\left(-jk\right)\left[2\right]dr = -\frac{1}{\pi} \tag{C.62}$$

$$A = \tfrac{1}{2jk\pi}$$

Therefore, 2-D Green's function when k$\neq$ 0 is given by

$$G\left(\vec{r_1},0\right) = \frac{1}{2jk\pi}e^{-jk\vec{r_1}} \tag{C.63}$$

$$G\left(\vec{r},\vec{r_o}\right) = \frac{1}{2jk\pi}e^{-jk\left|r-r_o\right|} \tag{C.64}$$

Since, $\vec{r_1} = \vec{r} - \vec{r_o}$

Case2: 3-Dimensional (3D) free-space Greens function

In order to derive 3-D free space Greens function consider wave function (ϕ) that satisfies inhomogeneous Helmholtz equation-(C.65) [70]

$$\bigtriangledown^2\phi\left(\vec{r}\right) + k^2\phi\left(\vec{r}\right) = -f\left(\vec{r}\right) \tag{C.65}$$

If wave function ($\phi\left(\vec{r}\right)$) propagates in infinite free space then there are no reflected waves [70]. Therefore, wave function $\phi\left(\vec{r}\right)$ satisfies radiation condition listed in equation-(C.66) [70]

$$r\left(\frac{\partial\phi}{\partial r} + jk\phi\right) = 0 \quad for \quad r\to\infty \tag{C.66}$$

The Greens function is obtained by solving the partial differential equation-(C.67)

[70]

$$\nabla^2 G\left(\vec{r},\vec{r_o}\right) + k^2 G\left(\vec{r},\vec{r_o}\right) = -\delta\left(\vec{r}-\vec{r_o}\right) \tag{C.67}$$

Therefore, potential '$\phi\left(\vec{r}\right)$' in equation-(C.64) is replaced by the Greens function '$G\left(\vec{r},\vec{r_o}\right)$' as in equation-(C.67) [70].

The representation of a point source used for solving Green's function is given as follows [70].

Consider point charge of unit strength located at point '$G\left(\vec{r},\vec{r_o}\right)'$' [70]. When volume of charge is zero then charge density is given as follows [70]

$$\delta\left(\vec{r}-\vec{r_o}\right) = \begin{matrix} \infty & \vec{r}=\vec{r_o} \\ 0 & \vec{r}\neq\vec{r_o} \end{matrix}$$

If total charge is unity, we have

$$\iiint_V \delta\left(\vec{r}-\vec{r_o}\right) dV = \begin{matrix} 1 & \vec{r}=\vec{r_o} \\ 0 & \vec{r}\neq\vec{r_o} \end{matrix}$$

By considering case where, $\delta\left(\vec{r}-\vec{r_o}\right) = 0$ when $\vec{r} \neq \vec{r_o}$ i.e., point source and observation point are at different locations and $\iiint_V \delta\left(\vec{r}-\vec{r_o}\right) dV = 1$ for '$\vec{r_o}$' enclosed by volume 'V'.

In order to solve for Greens function '$G\left(\vec{r},\vec{r_o}\right)$' in equation-(C.67) a new co-ordinate system is introduced with its origin located at point '$\vec{r_o}$' therefore we have $\vec{r_1} = \vec{r} - \vec{r_o}$ [70].

$$\nabla^2 G\left(\vec{r_1},0\right) + k^2 G\left(\vec{r_1},0\right) = -\delta\left(\vec{r_1}-0\right) \tag{C.68}$$

In equation-(C.68),from symmetry of spherical co-ordinates we have

$$\nabla^2 G\left(\vec{r_1},0\right) = \frac{1}{r_1^2}\frac{d}{dr_1}\left[r_1^2\frac{dG\left(\vec{r_1},0\right)}{dr_1}\right] \tag{C.69}$$

$$\frac{1}{r_1^2}\frac{d}{dr_1}\left[r_1^2\frac{dG\left(\vec{r_1},0\right)}{dr_1}\right] + k^2 G\left(\vec{r_1},0\right) = -\delta\left(\vec{r_1}-0\right) \tag{C.70}$$

Therefore, from symmetry property we have,

$$\frac{1}{r_1^2}\frac{d}{dr_1}\left[r_1^2\frac{dG\left(\vec{r_1},0\right)}{dr_1}\right] \cong \frac{1}{r_1}\frac{d^2}{dr_1^2}\left[r_1 G\left(\vec{r_1},0\right)\right] \tag{C.71}$$

$$\frac{d^2}{dr_1^2}\left[r_1 G\left(\vec{r_1},0\right)\right] + k^2 r_1 G\left(\vec{r_1},0\right) = 0 \tag{C.72}$$

The symmetry of Green's function for point source depends on distance $|\vec{r}-\vec{r_o}|$ [70].

The general solution of homogeneous wave equation except at location $\vec{r}=\vec{r_o}$ is of form [70]

$$\frac{Be^{ik|\vec{r}-\vec{r_o}|}+Ae^{-ik|\vec{r}-\vec{r_o}|}}{|\vec{r}-\vec{r_o}|} \tag{C.73}$$

Considering there are no reflecting waves towards the source when the wave approaches infinity the equation for Greens function is of the form

$$G\left(\vec{r},\vec{r_o}\right) = \frac{Ae^{-ik|\vec{r}-\vec{r_o}|}}{|\vec{r}-\vec{r_o}|} \tag{C.74}$$

$$G\left(r_1,0\right) = \frac{Ae^{-ik|\vec{r_1}|}}{|\vec{r_1}|} \tag{C.75}$$

Since, $\vec{r_1}=\vec{r}-\vec{r_o}$

(a): Static case k=0

In static case, k=0 is substituted in equation-(C.72)

$$\bigtriangledown^2 G\left(\vec{r_1},0\right) = -\delta\left(\vec{r_1}-0\right) \tag{C.76}$$

$$\frac{d^2}{dr_1^2}\left[r_1 G\left(\vec{r_1},0\right)\right] = 0 \tag{C.77}$$

Since, $\delta\left(\vec{r_1}-0\right)=0$ when $\vec{r}\neq\vec{r_o}$.

Therefore, we obtain,

$$G\left(\vec{r_1},0\right) = \frac{A}{r_1}+C \tag{C.78}$$

By considering partial derivative with respect to 'r_1' on both sides of above expression we obtain,

$$\frac{\partial G\left(\vec{r_1},0\right)}{\partial r_1} = A\left(-1\right)r_1^{-2} \tag{C.79}$$

$$\frac{\partial G\left(\vec{r_1},0\right)}{\partial r_1} = -\frac{A}{r_1^2} \tag{C.80}$$

In order to determine constant 'A' equation-(C.76) is integrated on both sides over entire volume 'V' [70].

$$\iiint\limits_V \bigtriangledown^2 G\left(\vec{r_1},0\right)dV = \iiint\limits_V -\delta\left(\vec{r_1},0\right)dV \tag{C.81}$$

$$\iiint\limits_V \bigtriangledown\cdot\bigtriangledown G\left(\vec{r_1},0\right)dV = \iiint\limits_V -\delta\left(\vec{r_1},0\right)dV \tag{C.82}$$

When $\vec{r} \neq \vec{r_o}$ then $\iiint_V \delta\left(\vec{r}-\vec{r_o}\right)dV = 1$

$$\iiint\limits_V \bigtriangledown\cdot\bigtriangledown G\left(\vec{r_1},0\right)dV = 1 \tag{C.83}$$

The divergence theorem in equation form is given by

$$\iiint\limits_V \bigtriangledown\cdot\bigtriangledown G\left(\vec{r_1},0\right)dV = \iiint\limits_S \bigtriangledown G\left(\vec{r_1},0\right)\cdot dS \tag{C.84}$$

Therefore, we have $dS = RSin\phi d\theta Rd\phi$

$$dS = R^2 Sin\phi d\theta d\phi \tag{C.85}$$

$$\int\limits_0^{2\pi}\int\limits_0^{\pi}\frac{\partial G}{\partial r_1}\left(R^2 sin\phi d\phi d\theta\right) = 1 \tag{C.86}$$

$$-A\int\limits_0^{2\pi}\int\limits_0^{\pi}\frac{1}{r_1^2}\left(R^2 sin\phi d\phi d\theta\right) = 1 \tag{C.87}$$

$$-A\int_0^{2\pi}\int_0^{\pi} sin\phi d\phi d\theta = 1 \tag{C.88}$$

$$-A\int_0^{2\pi}\left[-2\right]d\theta = 1 \tag{C.89}$$

$$2A\left[2\pi\right] = 1 \tag{C.90}$$

$$A = \tfrac{1}{4\pi}$$

$$G\left(\vec{r_1},0\right) = \tfrac{1}{4\pi\vec{r_1}}$$

Since, $\vec{r_1} = \vec{r} - \vec{r_o}$

$$G\left(\vec{r},\vec{r_o}\right) = \frac{1}{4\pi\left|\vec{r}-\vec{r_o}\right|} \tag{C.91}$$

(b): Case when k≠0

$$\frac{1}{r_1^2}\frac{\mathrm{d}}{\mathrm{d}r_1}\left[r_1^2\frac{dG\left(\vec{r_1},0\right)}{dr_1}\right] + k^2G\left(\vec{r_1},0\right) = -\delta\left(\vec{r_1}-0\right) \tag{C.92}$$

From symmetry property we obtain,

$$\frac{1}{r_1^2}\frac{\mathrm{d}}{\mathrm{d}r_1}\left[r_1^2\frac{dG\left(\vec{r_1},0\right)}{dr_1}\right] \cong \frac{\mathrm{d}^2}{\mathrm{d}r^2}\left[r_1G\left(\vec{r_1},0\right)\right] \tag{C.93}$$

$$\frac{\mathrm{d}^2}{\mathrm{d}r_1^2}\left[r_1G\left(\vec{r_1},0\right)\right] + k^2r_1G\left(\vec{r_1},0\right) = 0 \tag{C.94}$$

The solution of above equation is of form $G\left(\vec{r_1},0\right) = \frac{Ae^{-jk\vec{r_1}}}{r_1}$

By substituting in above expression, we obtain

$$\int_0^{r_1}\frac{1}{r_1^2}\frac{\mathrm{d}}{\mathrm{d}r_1}\left[r_1^2\frac{\mathrm{dG}}{\mathrm{d}r_1}\right]r_1^2dr_1 + k^2\int_0^{r_1}Gr_1^2dr_1 = \frac{-1}{2\pi} \tag{C.95}$$

$$\left[r_1^2\frac{\mathrm{dG}}{\mathrm{d}r_1}\right]_0^{r_1} + k^2\int_0^{r_1}Gr_1^2dr_1 = \frac{-1}{2\pi} \tag{C.96}$$

In above equation $Gr_1^2 \to 0 \;\; when \;\; r_1 \to 0$

Therefore, we have

$$\left[r_1^2 \frac{\mathrm{dG}}{\mathrm{d}r_1}\right]_{r_1 \to 0^-}^{r_1 \to 0^+} = \frac{-1}{2\pi} \tag{C.97}$$

$$r_1^2 \frac{\mathrm{d}}{\mathrm{d}r_1}\left[\frac{Ae^{-jk\vec{r_1}}}{r_1}\right]_{r_1 \to 0^-}^{r_1 \to 0^+} = \frac{-1}{2\pi} \tag{C.98}$$

$$Ar_1^2 \left[\frac{e^{-jk\vec{r_1}}\left(-jk\right)\frac{\mathrm{d}|\mathrm{r}_1|}{\mathrm{d}r_1} r_1 - e^{-jk\vec{r_1}}\frac{\mathrm{d}|\mathrm{r}_1|}{\mathrm{d}r_1}}{r_1^2}\right]_{r_1 \to 0^-}^{r_1 \to 0^+} = \frac{-1}{2\pi} \tag{C.99}$$

$$\left[-Ae^{-jk\vec{r_1}}\frac{\mathrm{d}\left|\mathrm{r}_1\right|}{\mathrm{d}r_1}\left(jkr_1 + 1\right)\right]_{r_1 \to 0^-}^{r_1 \to 0^+} = \frac{-1}{2\pi} \tag{C.100}$$

We know that $\left[\frac{\mathrm{d}|\mathrm{r}_1|}{\mathrm{d}r_1}\right]_{r_1 \to 0^-}^{r_1 \to 0^+} = 2$ from figure-(C.3) Therefore, when $r_1 \to 0$ we have $A = \frac{1}{4\pi}$ from above expression

Therefore, Green's function (3-D) is given by [70]

$$G\left(\vec{r_1}, 0\right) = \frac{e^{-jk\vec{r_1}}}{\left(4\pi\right) r_1} \tag{C.101}$$

$$G\left(\vec{r}, \vec{r_o}\right) = \frac{e^{-jk|\vec{r}-\vec{r_o}|}}{4\pi\left|\vec{r} - \vec{r_o}\right|} \tag{C.102}$$

Since, $\vec{r_1} = \vec{r} - \vec{r_o}$

APPENDIX D

RF Impedance Sensing based on Graphene

The two-dimensional (2-D) nanomaterial known as graphene has attracted wide attention recently due to its numerous applications and unique material properties [77]. This chapter demonstrates bio-sensors using coplanar waveguide (CPW) device [77]. The impedance sensing is performed using chemicals such as graphene, chitosan and DNA [77]. The experimental results presented in this chapter shows significant change in resonance frequencies [77]. In addition, permittivity has been extracted using modeling simulations and imaginary part of permittivity indicates leakage currents by using graphene, chitosan and DNA [77].

Introduction

Bio-sensors are used for various applications such as detecting disease, toxic substances etc, [77, 78-88]. In general, bio-sensing is categorized as direct labeling and label free methods [77]. The direct labeling method is performed by attaching label used for detecting new targets [77]. The main dis-advantage of direct labeling method is target coupling [77]. On the other hand label free method is is cost effective and consumes less time when compared to direct labeling method [77]. Therefore, main advantage of label free method is accuracy as it removes complexity caused by attaching label [77, 89-97]. At low frequency (d-c) applications carbon nanotubes (CNTs) are used as bio-sensors by observing the change in resistance caused by chemicals such as graphene, chitosan and DNA [83-88]. The experimental results presented in this chapter shows change in impedance versus frequency caused by the chemicals [77].

Experimental Procedure

The graphene oxide (GO) was prepared using chemical intercalation method and its thickness was measured approximately 1.1nm using atomic force microscopy (AFM) shown in figure-(D.1) [77]. Whereas the thickness of diluted graphene oxide was measured as 1.3nm as shown in figure-(D.2) [77].

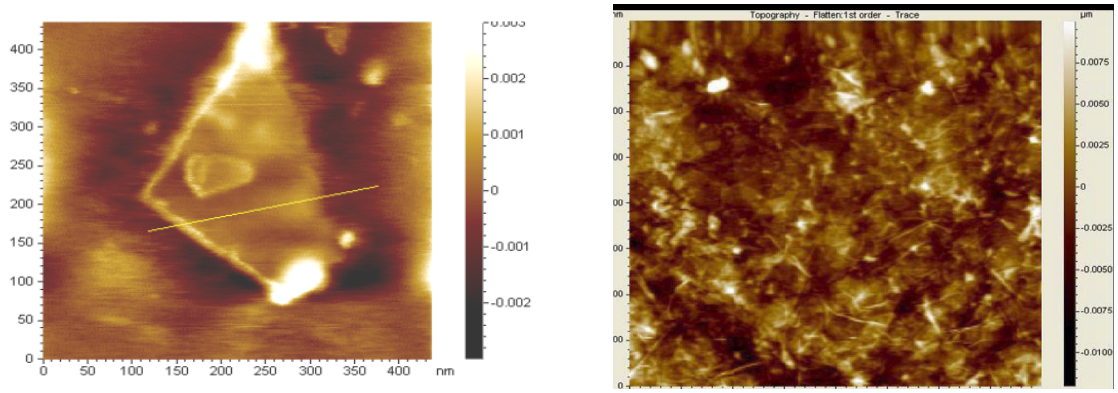

Figure D.1: AFM image of diluted (1:100) graphene oxide (Left) and concentrated graphene oxide (Right).

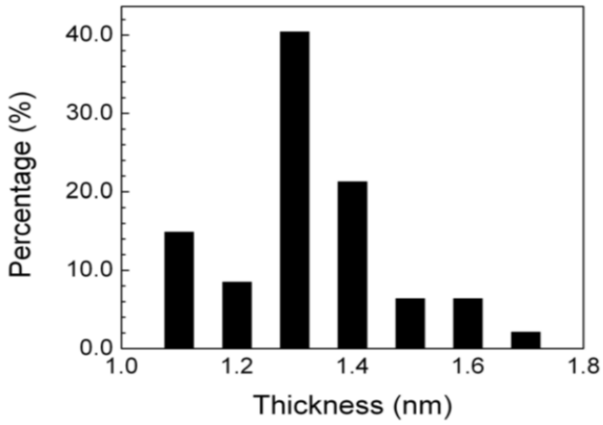

Figure D.2: Thickness distribution of diluted graphene oxide (GO).

Coplanar Waveguide Design

The coplanar wavegudies (CPWs) with various structural device parameters listed in table-(D.1) were fabricated in this work for impedance sensing [77]. The r-f mea-

surements for impedance versus frequency were performed by using Cascade r-f wafer probe station (M150) at 26GHz frequency by measuring 1-port S-parameters on network analyzer (Agilent PNA-N5230A) [77].

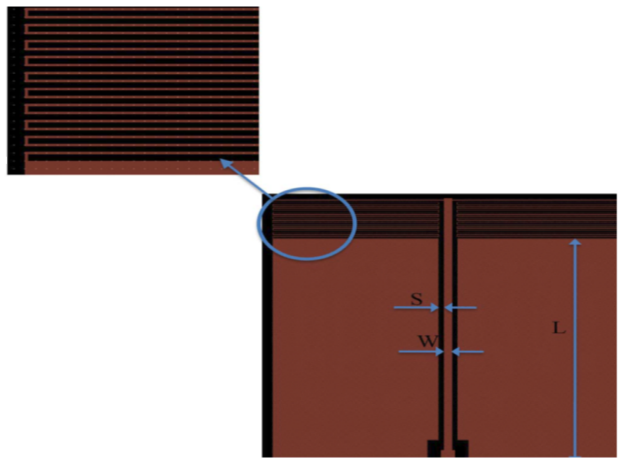

Figure D.3: Coplanar waveguide (CPW) device with meander load. The width (W) and spacing (S) of meander line are 3μm and 10μm .

Device	$L(\mu\mathbf{m})$	$W(\mu\mathbf{m})$	$S(\mu\mathbf{m})$	$Load()$
A1	1000	30	20	50
B1	1000	30	20	25
C1	1000	30	20	12.5

Table D.1: Structural parameters of fabricated coplanar waveguides (CPWs).

The structure of coplanar waveguide (CPW) device designed using Agilent advanced design system (ADS) is shown in figure-(D.3) [77]. The coplanar waveguide device was fabricated on glass substrate (AF-45) with titanium (Ti) or gold (Au) deposited during fabrication [77]. The titanium (Ti) layer of thickness 200nm was deposited between gold and glass substrate for adhesion [77]. As shown in figure-(D.3) the coplanar waveguide device consisted of meander lines as load with different number of turns. The impedance of coplanar waveguide device load are 50Ω, 25Ω and 12.5Ω (table-D.1) [77]. The table-(D.1) lists the structural parameters of fabricated coplanar waveguide devices.

Experimental Results

RF Impedance Characterization

The experiments were performed by coating coplanar waveguide (CPW) device with graphene oxide (GO) solution (40 μl) [77]. Next, chitosan (Sigma-Aldrich) chemical was used by placing it on top of graphene oxide (GO) in between graphene and DNA chemicals [77]. Lastly, a drop of DNA (calfthymus) chemical (1 μg/ml) was coated on top of chitosan [77]. The measurements for impedance sensing were performed in this work by utilizing coplanar waveguide (CPW) devices measured on network analyzer at 0.5-26GHz frequency range [77].

The equation for load impedance (Z_L) is given by equation-(D.1) [77].

$$Z_L = Z_0 \frac{Z_{in} - Z_0 tanh\,(\gamma l)}{Z_0 - Z_{in} tanh\,(\gamma l)} \tag{D.1}$$

In equation-(D.1), Z_0, is characteristic impedance, and l is length of CPW device [77]. Therefore, input impedance (Z_{in}) is obtained by measuring 1-port S-parameters (S_{11}) given by equation-(D.2) [77]

$$Z_{in} = \frac{1 + S_{11}}{1 - S_{11}} \tag{D.2}$$

By substituting equation-(D.2) in equation-(D.1) the load impedance is given by equation-(D.3) [77, 78].

$$Z_L = Z_0 \frac{(1 + S_{11}) - Z_0\,(1 - S_{11})\,tanh\,(\gamma l)}{Z_0\,(1 - S_{11}) - (1 + S_{11})\,tanh\gamma l} \tag{D.3}$$

In equation-(D.3), at low frequencies ($\gamma l << 1$) the load impedance is given by equation-(D.4) [77].

$$Z_L = \frac{1 + S_{11}}{1 - S_{11}} \tag{D.4}$$

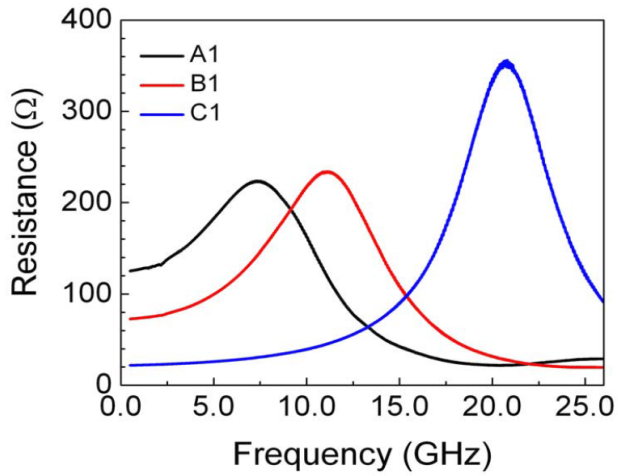

Figure D.4: Measured resistance versus frequency for coplanar waveguide (CPW) devices.

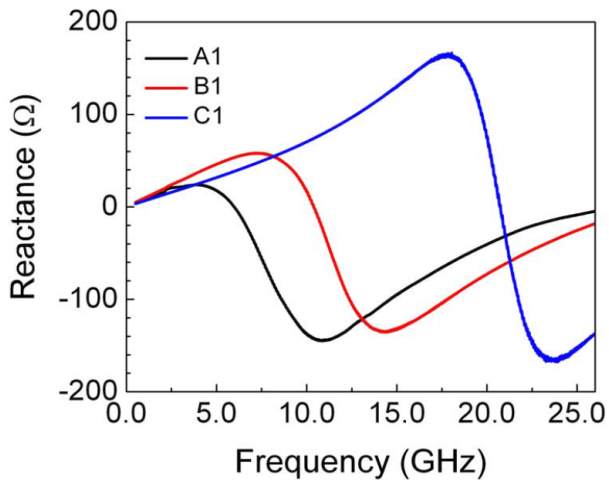

Figure D.5: Measured reactance versus frequency for coplanar waveguide (CPW) devices.

The results of measured load (Z_L) impedance versus frequency are shown in figures (D.4) and (D.5). It can be observed in figures-(D.4) and (D.5) that measured resistance and inductance versus frequency for coplanar waveguide devices (A1, B1 and C1) maximum resistance and zero inductance at 6GHz, 10.5GHz and 20.8GHz frequency [77]. The meander lines in coplanar waveguide device shows inductance

and resistance due to LC resonance phenomenon [77]. In addition, it can be observed that large number of meander line turns caused high inductance and resistance values due to low resonant frequency [77].

Effective Permittivity of Substrate

The experimental results obtained by adding chemicals on coplanar waveguide are listed in figures-(D.6) and (D.7). The figure-(D.6) shows shift in resonant frequency obtained by adding chemicals and figure-(D.7) shows decrease in resistance by adding chemicals [77]. Therefore, adding chemicals with different dielectric constant values caused change in parasitic capacitance value [77]. The change in parasitic capacitance led to resonant frequency shift observed in figures-(D.6) and (D.7) [77].

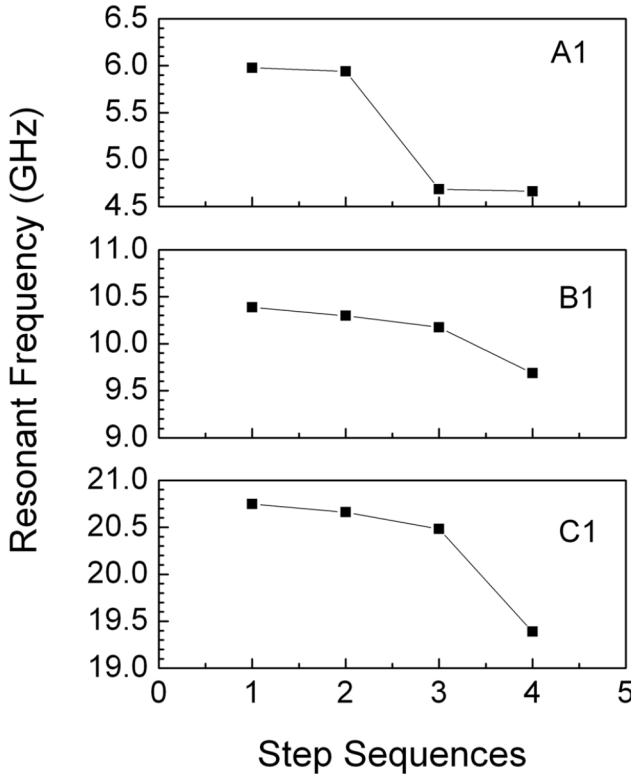

Figure D.6: RF impedance measured for coplanar waveguide (CPW) devices. (1) CPW, (2) CPW coated with graphene, (3) CPW coated with graphene and chitosan, (4) CPW coated with graphene, chitosan and DNA.

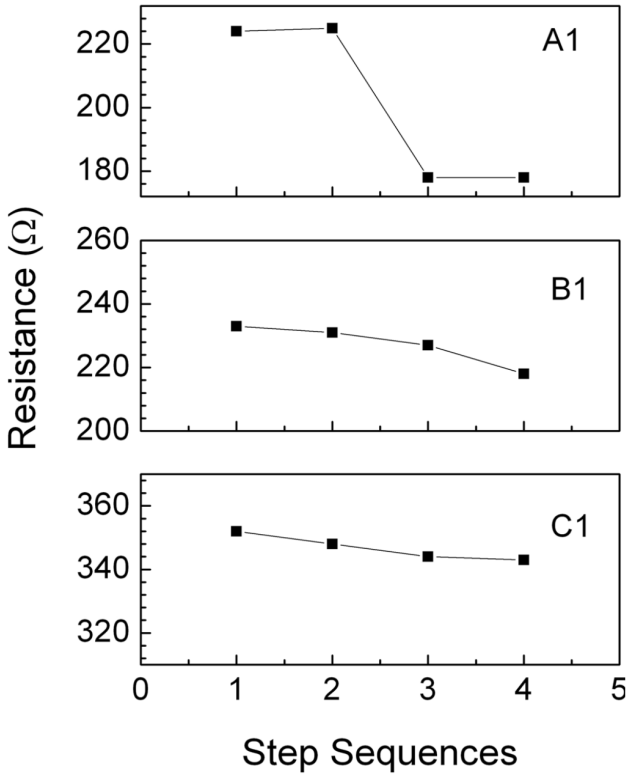

Figure D.7: Measured change in resistance at resonance frequencies. (1) CPW, (2) CPW coated with graphene, (3) CPW coated with graphene and chitosan, (4) CPW coated with graphene, chitosan and DNA.

In addition, two dimensional (2-D) electromagnetic simulations were performed using Advanced design system (ADS) software for obtaining parasitic capacitance value caused by substrates permittivity [77]. The real and imaginary part of permittivity value has been obtained from the simulation results listed in table-(D.2) [77]. The permittivity is a complex quantity given by $\left(\epsilon = \epsilon^{'} + \epsilon^{"}\right)$. The dielectric constant of graphene was larger which caused increase in capacitance and decrease in resonance frequency [77]. The major change in capacitance value was obtained due to real part of permittivity $\left(\epsilon^{'}\right)$, chemical thickness and device coverage etc, [77]. The experimental results obtained in this work are depended on properties of chemicals such as graphene oxide on coplanar waveguide device (A1, B1 and C1). Therefore, adding chemicals such as chitosan and DNA also caused shift in frequency [77].

The imaginary part of the permittivity $\left(\epsilon^{"}\right)$ and conductivity (σ) are related by

$\epsilon^{"} = \frac{\sigma}{j\omega}$. Where, ω is angular frequency [77]. The tangent loss is given by $tan\delta = \frac{\epsilon^{"}}{\epsilon^{'}}$ [77]. The leakage currents obtained in simulation results caused decrease in the resistance at resonant frequencies as shown in figure-(D.6) [77].

The equivalent circuit of coplanar waveguide (CPW) load structure is shown in figure-(D.8) [77].

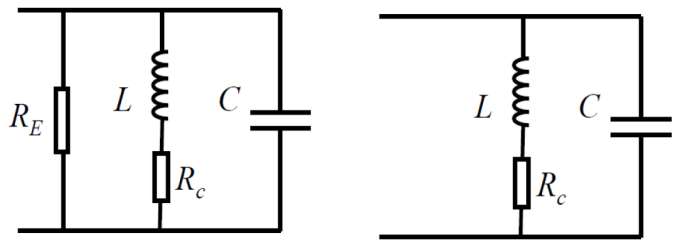

Figure D.8: Equivalent circuit of coplanar waveguide (CPW) input impedance.

In figure-(D.8), R_c is resistance of conductor and R_E is leakage current caused by chemicals [77]. The equivalent circuit of input impedance without adding any chemicals is given by (Figure-D.8 (right)) [77].

The equations-(D.5), (D.6) and (D.7) are used for calculating input impedance [77]. Where, R_{in} is real part of input impedance, X_{in} is imaginary part of input impedance and ω is angular frequency [77].

$$Z_{in} = R_{in} + jX_{in} \tag{D.5}$$

$$R_{in} = \frac{R_c\left(1-\omega^2 LC\right) + \omega^2 R_c LC}{\left(1-\omega^2 LC\right)^2 + \omega^2 R_c^2 C^2} \tag{D.6}$$

$$X_{in} = \frac{\omega L\left(1-\omega^2 LC\right) - \omega R_c^2 C}{\left(1-\omega^2 LC\right)^2 + \omega^2 R_c^2 C^2} \tag{D.7}$$

The resonant frequency ω_o is defined when X_{in}=0 given by equation-(D.8) [77].

$$\omega_o = \sqrt{\frac{1}{LC} - \frac{R^2}{L^2}} \tag{D.8}$$

The resistance and inductance of coplanar waveguide (CPW) device meander line

depends on total length [77]. The resistance and inductance are constant if eddy current is negligible [77]. Therefore, resonant frequency is given as product of inductance and capacitance as shown in equation-(D.8) [77]. The experimental measurement results showed that adding chemicals caused increase in capacitance and decrease in resonant frequency [77].

The expression for resistance at resonant frequency is given by equation-(D.9)

$$R_{in}\left(\omega_0\right) = \frac{1}{R_c} \tag{D.9}$$

The input resistance at resonant frequency is reciprocal of resistance given by equation-(D.9) and indicated by resistance peak for C1 device at resonant frequency due to low resistance load (figure-D.4) [77]. After adding chemicals the effective resistance (R_E) has leakage current shown in Figure-D.8 (left) [77]. The shunt effective resistance (R_E) caused decrease in total resistance at resonant frequency shown in figure-(D.5) [77]. In addition, leakage current caused the total resistance to decrease after adding chemicals (figure-D.7) [77].

	CPW	GO	Chitosan	DNA
ϵ (Relative)	4.05	4.10	4.20	4.73
$tan\delta$	0.00	0.015	0.02	0.05

Table D.2: Effective substrate permitivity after adding chemicals.

The resonant frequency in simulation results has been determined by relative permittivity of chemicals [77]. The conductivity of chemicals was also included during simulations in order to match the resistance at resonant frequencies [77]. The thickness and density of chemical can also be considered in future experimental analysis [77].

Conclusions

The experimental results for r-f impedance sensing are presented in this appendix chapter [77]. The experimental results showed that chemicals such as chitosan,

graphene and DNA caused change in resonant frequency and decrease in resistance for coplanar waveguide (CPW) device [77]. In addition, real and imaginary parts of permittivity showed that the proposed method of bio-sensing in this work can be used for investigating new compounds in future [77].

BIBLIOGRAPHY

Bibliography

1. P. Khalili Amiri, ‘‘Magnetic Materials and Devices for Integrated Radio-Frequency Electronics’’, PhD Thesis Delft University of Technology, 2008.

2. R.P. Feynman, R.B. Leighton, M.L. Sands, ‘‘The Feynman Lectures on Physics’’, Vol. 2, Addison-Wesley, Reading, Massachusetts, 1964.

3. S. B. Cohn and R. Levy. ‘‘History of microwave passive components with particular attention to directional couplers’’,IEEE Transactions on Microwave Theory and Techniques, Vol. 32, No. 9, pp. 1046-1054. 1984.

4. G.E. Moore,‘‘Cramming more components onto integrated circuits,’’ Electronics, Vol. 38, No. 8, pp. 114-117, 1965.

5. B. Razavi,‘‘RF Microelectronics’’, Prentice-Hall, Englewood Cliffs, New Jersey, 1998.

6. J.N. Burghartz,‘‘Status and trends of silicon RF technology,’’ Microelectron. Reliab., Vol. 41, No. 1, pp. 13-19, 2001.

7. J. R. Long. SiGe radio frequency ICs for low-power portable communication. IEEE Proceedings, vol. 93, no. 9, pp. 1598-1623. 2005.

8. H. Sobol and K. Tomiyasu.‘‘Milestones of microwaves’’, IEEE Transactions on Microwave Theory and Techniques, Vol. 50, No. 3, pp. 594-611. 2002.

9. B. Razavi, ‘‘CMOS technology characterization for analog and RF design,’’ IEEE J. Solid-State Circuits, Vol. 34, No. 3, pp. 268-276, 1999.

10. A.G. Gurevich, G.A. Melkov, ‘‘Magnetization oscillations and waves’’, CRC Press, New York, 1996.

11. B. Rejaei and M. Vroubel,“Suppression of skin effect in metal/ferromagnet superlattice conductors”, J. Appl. Phys., Vol. 96, No. 11, pp. 6863-6868. 2004.

12. I. Iramnaaz, T. Sandoval, Y. Zhuang, H. Schellevis, B. Rejaei,“High quality factor RF inductors using low loss conductor featured with skin effect suppression for standard CMOS/BiCMOS.” IEEE 61st, Electronic Components and Technology Conference (ECTC), pp. 163-168, 2011.

13. I. Iramnaaz, H. Schellevis, B. Rejaei, R. Fitch, Y. Zhuang, “High-Quality Integrated Inductors Based on Multilayered Meta-Conductors,” IEEE Microwave and Wireless Components Letters., Vol. 22, Issue 7, pp. 345-347, 2012.

14. I. Iramnaaz, H. Schellevis, B. Rejaei, R. Fitch, Y. Zhuang,“Self-Biased Low Loss Conductor Featured with Skin Effect Suppression for High Quality RF Passives,” IEEE Transactions on Magnetics, Vol. 48, Issue 11, pp. 4139-4142, 2012.

15. J. N. Burghartz, D. C. Edelstein, K. A. Jenkins, Y. H. Kwark, “Spiral inductors and transmission lines in silicon technology using copper-damascene interconnects and low-loss substrates,” IEEE Trans. Microwave Theory Tech., Vol. 45, pp. 1961-1968, 1997.

16. K. J. Herrick, J. G. Yook, and L. P. B. Katehi,“Microtechnology in the development of three-dimensional circuits,” IEEE Trans. Microwave Theory Tech., Vol. 46, pp. 18321844, 1998.

17. M. Vroubel, Y. Zhuang, B. Rejaei, J. N. Burghartz,“Patterned FeNi thin film for RF and microwave components”, Journal of Magnetism and Magnetic Materials, Vol. 258-259, pp. 167-169, 2003.

18. J.C. Rautio, V. Demir,“Microstrip conductor loss models for electromagnetic analysis,” IEEE Trans. Microwave Theory Tech., Vol. 51, pp. 915921, 2003.

19. A. S. Antonov, I. T. Iakubov,''The high-frequency magneto-impedance of a sandwich with transverse magnetic anisotropy'', J. Phys. D: Appl. Phys., Vol. 32, No. 11, pp. 12041208, 1999.

20. R.E. Collin, ''Field Theory of Guided Waves'', IEEE Press, New York, 1991.

21. By contrast, the normal component of the electric field and the tangential component of the magnetic field are usually not continuous across the surface of a zero-thickness conductor. This is because of the presence of surface charges, respectively, flow of surface current in the conductor.

22. Hassan, Hassan, Mohab Anis, and Mohamed Elmasry. ''Impact of technology scaling and process variations on RF CMOS devices.'' Microelectronics journal 37, no. 4 (2006): 275-282.

23. R. Ludwig and P. Bretchko,''RF Circuit Design: Theory and Applications'', Prentice-Hall, New Jersey, 2000.

24. Lax, Benjamin, and Kenneth J. Button. Microwave Ferrites and Ferrimagnetics. New York: McGraw-Hill, 1962. Print. Lincoln Laboratory Publications.

25. Miyazaki, Terunobu, and Hanmin Jin.''The physics of ferromagnetism.'' Berlin:Springer, 2012.

26. J.N. Burghartz, B. Rejaei, ''On the design of RF spiral inductors on silicon,'' IEEE Trans. Electron Devices, Vol. 50, No. 3, pp. 718-729, 2003.

27. J.N. Burghartz, D.C. Edelstein, M. Soyuer, H.A. Ainspan, K.A. Jenkins,''RF circuit design aspects of spiral inductors on silicon,'' IEEE J. Solid-State Circuits, Vol. 33, No. 12, pp. 2028-2034, 1998.

28. V. Korenivski and R. B. van Dover,''Magnetic film inductors for radio frequency applications'', Journal of Applied Physics., Vol. 82, No. 10, pp. 5247-5254,

1997.

29. R.M. Bozorth, ‘‘Ferromagnetism’’, D. Van Nostrand, New York, 1951. (Reprinted by Lucent Technologies, New Jersey, 1978.)

30. M. Yamaguchi, M. Baba, K.-I. Arai, ‘‘Sandwich-type ferromagnetic RF integrated inductor’’, IEEE Trans. Microwave Theory Tech., Vol. 49, No. 12, pp. 2331-2335, 2001.

31. A.M. Crawford, D. Gardner, S.X. Wang, ‘‘High-frequency microinductors with amorphous magnetic ground planes’’, IEEE Trans. Magn., Vol. 38, No. 5, pp. 3168-3170, 2002.

32. A. Gromov, V. Korenivski, K.V. Rao, R. B. van Dover, P. M. Mankiewich,‘‘A model for impedance of planar RF inductors based on magnetic films,’’ IEEE Transactions on Magnetics, Vol.34, No.4, pp. 12461248, 1998.

33. Y. Zhuang, M. Vroubel, B. Rejaei, J.N. Burghartz, ‘‘Ferromagnetic RF Inductors and Transformers for Standard CMOS/BiCMOS,’’ IEDM Tech. Dig., pp. 475-478, 2002.

34. M. Yamaguchi, T. Kuribara, K. I. Arai, ‘‘Two-port type ferromagnetic RF integrated inductor’’, IEEE MTT-S International, Microwave Symposium Digest, pp. 197-200, 2002.

35. V. Korenivski, R. B. van Dover, ‘‘Design of high frequency inductors based on magnetic films’’. IEEE Transactions on Magnetics, Vol. 34, No. 4, pp. 1375-1377, 1998.

36. J. Y. Park, M. G. Allen, ‘‘Integrated electroplated micromachined magnetic devices using low temperature fabrication processes,’’ IEEE Trans. Electron. Packag. Manuf., Vol. 23, No. 1, pp. 4855, 2000.

37. D. Makhnovskiy, A. Lagar'kov, L. Panina and K. Mohri, ''Effect of antisymmetric bias field on magneto-impedance in multilayers with crossed anisotropy'', Sensors and Actuators A: Physical, Vol. 81, No. 1, pp. 106-110, 2000.

38. R. E. Camley and D. L. Mills, ''Theory of microwave propagation in dielectric/magnetic film multilayer structures'', Journal of Applied Physics., Vol. 82,No. 6, pp. 3058-3067. 1997.

39. T. J. Klemmer, K. A. Ellis, L. H. Chen, B. van Dover, S. Jin, ''Ultrahigh frequency permeability of sputtered FeCoB thin films,'' J. Appl. Phys., Vol. 87, pp. 830833, 2000.

40. S. X. Wang, N. X. Sun, M. Yamaguchi, S. Yabukami, ''Properties of a new soft magnetic materials,'' Nature, Vol. 407, pp. 150151, 2000.

41. L. V. Panina, D. P. Makhnovskiy, K. Mohri,''Analysis of magnetoimpedance in multilayers with cross anisotropy,'' J. Magn. Soc. Jap., Vol. 23, pp. 925930, 1999.

42. Behzad Rejaei. ''Impedance of a planar solenoid with a thin magnetic core'', Journal of Applied Physics, 2007.

43. N. M. Nguyen and R. G. Meyer. ''Si IC-compatible inductors and LC passive filters'', IEEE Journal of Solid-State Circuits, Vol. 25, No. 4, pp. 1028-1031. 1990.

44. P. K. Amiri and B. Rejaei, ''Magnetostatic waves in layered materials and devices,'' J. Appl. Phys., Vol. 100, No. 10, pp. 103909, 2006.

45. J. D. Meindl, ''Interconnect opportunities for gigascale integration,'' IEEE Micro, Vol. 23, pp. 2835, 2003.

46. J. N. Burghartz, K. A. Jenkins, M. Soyuer, ‘‘Multilevel-spiral inductors using VLSI interconnect technology,’’ IEEE Electron Device Letters, Vol. 17,No. 9, pp. 428-430. 1996.

47. Tretiakov, Y., Vaed, K., Ahlgren, D., Rascoe, J., Venkatadri, S. & Woods, W. 2004,‘‘On wafer de-embedding for SiGe/BiCMOS/RFCMOS transmission line interconnect characterization’’, Interconnect Technology Conference, Proceedings of the IEEE 2004 International, pp. 166, 2004.

48. E. S. Daniel, N. E. Harff, V. Sokolov, S. M. Schreiber and B. K. Gilbert, ‘‘Network analyzer measurement de-embedding utilizing a distributed transmission matrix bisection of a single THRU structure’’, 63rd, ARFTG Conference Digest Spring, 2004. pp. 61, 2004.

49. Kaganov M. I, Paash G. Impedance of a ferromagnetic metal near antiresonance, Zh. Eksp. Teor. Fiz. 70, pp. 1112-1120, 1976.

50. R. Rosenberg, D. C. Edelstein, C.-K. Hu, K. P. Rodbell, ‘‘Copper metallization for high performance silicon technology,’’ Annu. Review Mater. Sci., Vol. 30, pp. 229262, 2000.

51. J. Lim, D. Kwon, J. Rieh, S. Kim and S. Hwang, ‘‘RF characterization and modeling of various wire bond transitions’’, Advanced Packaging, IEEE Transactions on, Vol. 28, No. 4, pp. 772-778, 2005.

52. D. F. Williams, J.-.Belquin, G. Dambrine and R. Fenton, ‘‘On-wafer measurement at millimeter wave frequencies’’, Microwave Symposium Digest, 1996., IEEE MTT-S International, pp. 1683, 1996.

53. B. Rejaei, J. N. Burghartz and H. Schellevis, ‘‘Saddle add-on metallisation (SAM) for RF inductor implementation in standard IC interconnects’’, Electron Devices Meeting, 2002. IEDM ’02. International, pp. 467, 2002.

54. B. Rejaei, M. Vroubel, Y. Zhuang, and J. N. Burghartz, ‘‘Assessment of ferromagnetic integrated inductors for Si-technology,’’ in 4th Topical Silicon Monolithic Integrated Circuits in RF Systems Meeting Dig., pp. 100103, Apr. 2003.

55. R. Soohoo,‘‘Magnetic thin film inductors for integrated circuit applications’’, IEEE Transactions on Magnetics, 15(6), pp. 1803-1805. 1979.

56. M. Yamaguchi, K. Suezawa, K. -. Arai, Y. Takahashi, S. Kikuchi, Y. Shimada, W. D. Li, S. Tanabe and K. Ito,‘‘Microfabrication and characteristics of magnetic thin-film inductors in the ultrahigh frequency region’’, Journal of Applied Physics 85(11), pp. 7919-7922. 1999.

57. Y. Zhuang, B. Rejaei, E. Boellaard, M. Vroubel, J. N. Burghartz, ‘‘GHz bandstop microstrip filter using patterned $Ni_{78}Fe_{22}$ ferromagnetic film,’’ IEEE Microw. Wireless Compon. Lett., Vol. 12, No. 12, pp. 473-475, 2002.

58. K. Shirakawa, H. Kurata, J. Toriu, H. Matsuki and K. Murakami, ‘‘A new planar inductor with magnetic closed circuit’’, Magnetics, IEEE Transactions on 27(6), pp. 5432-5434. 1991.

59. D. Chen, J. A. Brug and R. B. Goldfarb, ‘‘Demagnetizing factors for cylinders,’’ Magnetics, IEEE Transactions on 27(4), pp. 3601-3619. 1991.

60. G. Zheng, M. PardaviHorvath, X. Huang, B. Keszei and J. Vandlik, ‘‘Experimental determination of an effective demagnetization factor for nonellipsoidal geometries,’’ J. Appl. Phys., Vol.79, No. 8, pp. 5742-5744. 1996.

61. A. Aharoni, ‘‘Demagnetizing factors for rectangular ferromagnetic prisms,’’ J. Appl. Phys., Vol. 83, pp. 3432, 1998.

62. J. A. Osborn, ‘‘Demagnetizing factors of the general ellipsoid,’’ Phys. Rev., Vol. 67, pp. 351357, 1945.

63. R. I. Joseph and E. Schlomann, ‘‘Demagnetizing field in nonellipsoidal bodies,’’ Journal of Applied Physics, Vol. 36,No. 5, pp. 1579-1593. 1965.

64. L. R. Walker, ‘‘Magnetostatic modes in ferromagnetic resonance,’’ Physical Review, Vol. 105, pp. 390-399, 1957.

65. C. Kittel, ‘‘Excitation of spin waves in a ferromagnetic by a uniform rf field,’’ Phys. Rev., Vol. 110, No. 6, pp. 12951297, 1958.

66. C.E. Patton, ‘‘Magnetic excitations in solids.’’ Physics Reports 103, no. 5 (1984): 251-315.

67. B. Kalinikos and A. Slavin, ‘‘Theory of dipole-exchange spin wave spectrum for ferromagnetic films with mixed exchange boundary conditions,’’ Journal of Physics C: Solid State Physics 19(35), pp. 7013, 1986.

68. C. Bayer, J. Jorzick, B. Hillebrands, S. Demokritov, R. Kouba, R. Bozinoski, A. Slavin, K. Guslienko, D. Berkov and N. Gorn, ‘‘Spin-wave excitations in finite rectangular elements of $Ni_{80}Fe_{20}$,’’ Physical Review B 72(6), pp. 064427. 2005.

69. C. A. Balanis, Advanced Engineering Electromagnetics. New York: Wiley, 1989.

70. J. M. Jin, The Finite Element Method in Electromagnetics, 2nd ed. New York, NY, USA: Wiley, 2002.

71. P. Bryant, J. Smyth, S. Schultz and D. Fredkin, ‘‘Magnetostatic-mode spectrum of rectangular ferromagnetic particles’’ Phys. Rev. B 47, No. 17, 11255 (1993).

72. K. Y. Guslienko, S. Demokritov, B. Hillebrands and A. Slavin,‘‘Effective dipolar boundary conditions for dynamic magnetization in thin magnetic stripes,’’ Physical Review B 66(13), pp. 132402. 2002.

73. The symmetry of the kernel implies that the eigenvalues and eigenfunctions are real quantities. Furthermore, since is a Hilbert-Schmidt kernel, i.e., , upon proper normalization one has the orthonormality condition , where is the kronecker delta [see F.G. Tricomi, Integral Equations(Dover, New York, 1985)]. Without proof, we also assume that the set of the eigenfunctions is complete, so that every arbitrary function can be expanded in on the interval [-w/2, w/2].

74. G. Counil, J. Kim, T. Devolder, C. Chappert, K. Shigeto and Y. Otani, ''Spin wave contributions to the high-frequency magnetic response of thin films obtained with inductive methods'', Journal of Applied Physics 95(10), pp. 5646-5652. 2004.

75. N. J. Moll, ''Coupling of circuit structures to magnetostatic modes of ferromagnetic resonators'', Microwave Theory and Techniques, IEEE Transactions on 25(11), pp. 933-938. 1977.

76. D. Rytting. ''Network analyzer error models and calibration methods.'' White Paper, September 1998, Hewlett-Packard Company.

77. I. Iramnaaz, Y. Xing, K. Xue, Y. Zhuang and R. Fitch, ''Graphene based RF/microwave impedance sensing of DNA'', Presented at Electronic Components and Technology Conference (ECTC), 2011 IEEE 61st. 2011.

78. A. J. Haes, L. Chang, W. L. Klein and R. P. Van Duyne, ''Detection of a biomarker for alzheimer's disease from synthetic and clinical samples using a nanoscale optical biosensor'', J. Am. Chem. Soc. 127(7), pp. 2264-2271. 2005.

79. Y. Lin, F. Lu, Y. Tu and Z. Ren, ''Glucose biosensors based on carbon nanotube nanoelectrode ensembles'', Nano Letters, Vol. 4, No. 2, pp. 191-195. 2004.

80. Y. Liu, M. Wang, F. Zhao, Z. Xu and S. Dong, ''The direct electron transfer

of glucose oxidase and glucose biosensor based on carbon nanotubes/chitosan matrix'', Biosensors and Bioelectronics, Vol. 21, No. 6, pp. 984-988. 2005.

81. J. Wang, ''Carbon-Nanotube Based Electrochemical Biosensors: A Review'', Electroanalysis, vol. 17, no. 1, pp. 7-14, 2005.

82. K. Rogers, ''Recent advances in biosensor techniques for environmental monitoring'', Anal. Chim. Acta, vol. 568, no. 1, pp. 222-231. 2006.

83. C. Shan, H. Yang, J. Song, D. Han, A. Ivaska and L. Niu,''Direct electrochemistry of glucose oxidase and biosensing for glucose based on graphene'', Anal. Chem. 81(6), pp. 2378-2382. 2009.

84. M. Zhou, Y. Zhai and S. Dong, ''Electrochemical sensing and biosensing platform based on chemically reduced graphene oxide'', Anal. Chem, vol. 81, no. 14, pp. 5603-5613, 2009.

85. C. Lu, H. Yang, C. Zhu, X. Chen and G. Chen, ''A graphene platform for sensing biomolecules'', Angewandte Chemie, vol. 121, no. 26, pp. 4879-4881. 2009.

86. N. Mohanty and V. Berry, ''Graphene-based single-bacterium resolution biodevice and DNA transistor: Interfacing graphene derivatives with nanoscale and microscale biocomponents'', Nano Letters, vol. 8, no. 12, pp. 4469-4476, 2008.

87. X. Kang, J. Wang, H. Wu, I. A. Aksay, J. Liu and Y. Lin, ''Glucose oxidasegraphenechitosan modified electrode for direct electrochemistry and glucose sensing'', Biosensors and Bioelectronics, vol. 25, no. 4, pp. 901-905, 2009.

88. J. Wu, M. Xu and G. Zhao, ''Graphene-based modified electrode for the direct electron transfer of cytochrome c and biosensing'', Electrochemistry Communications, vol. 12, no. 1, pp. 175-177. 2010.

89. N. Nandi, K. Bhattacharyya and B. Bagchi, ‘‘Dielectric relaxation and solvation dynamics of water in complex chemical and biological systems’’, Chem. Rev., vol. 100, no. 6, pp. 2013-2046. 2000.

90. K. R. Foster, J. L. Schepps and B. R. Epstein, ‘‘Microwave dielectric studies on proteins, tissues, and heterogeneous suspensions’’, Bioelectromagnetics, vol. 3, no. 1, pp. 29-43. 1982.

91. J. Hefti, A. Pan and A. Kumar, ‘‘Sensitive detection method of dielectric dispersions in aqueous-based, surface-bound macromolecular structures using microwave spectroscopy’’, Appl. Phys. Lett., vol. 75, no. 12, pp. 1802-1804. 1999.

92. I. Ermolina, H. Morgan, N. G. Green, J. J. Milner and Y. Feldman,‘‘Dielectric spectroscopy of tobacco mosaic virus’’, Biochimica Et Biophysica Acta (BBA)-General Subjects, vol. 1622, no. 1, pp. 57-63. 2003.

93. M. Suzuki, J. Shigematsu and T. Kodama, ‘‘Hydration study of proteins in solution by microwave dielectric analysis’’, J. Phys. Chem., vol. 100, no. 17, pp. 7279-7282. 1996.

94. C. Dalmay, A. Pothier, P. Blondy, F. Lalloue and M. Jauberteau,‘‘Label free biosensors for human cell characterization using radio and microwave frequencies’’, Microwave Symposium Digest, 2008 IEEE MTT-S International.

95. C. Dalmay, A. Pothier, M. Cheray, F. Lalloue, M. Jauberteau and P. Blondy, ‘‘Label-free RF biosensors for human cell dielectric spectroscopy’’, International Journal of Microwave and Wireless Technologies, vol. 1, no. 06, pp. 497-504, 2009.

96. B. Blad and B. Baldetorp,‘‘Impedance spectra of tumour tissue in comparison with normal tissue; a possible clinical application for electrical impedance

tomography'', Physiol. Meas. 17(4A), pp. A105. 1996.

97. A. Vander Vorst, A. Rosen, and Y. Kotsuka, IEEE Press, Los Alamitos, 2006.

List of Publications

Journals

- Hussaini, S., Rejaei, B., Zhuang, Y., Vishal, K., ‘‘Theoretical and Experimental study of magneto-dynamics in thin ferromagnetic films based on the single-turn solenoid device’’, IEEE Microwave and Wireless Components Letters, in preparation (2015).

- Iramnaaz, I., Schellevis, H., Rejaei, B., Fitch, R., Zhuang, Y., ‘‘Self-Biased Low Loss Conductor Featured With Skin Effect Suppression for High Quality RF Passives’’, Magnetics, IEEE Transactions on, On page(s): 4139 - 4142 Volume: 48, Issue: 11, Nov. 2012.

- Iramnaaz, I., Schellevis, H., Rejaei, B., Fitch, R., Zhuang, Y., ‘‘High-Quality Integrated Inductors Based on Multilayered Meta-Conductors’’, Microwave and Wireless Components Letters, IEEE, On page(s): 345 - 347 Volume: 22, Issue: 7, July 2012.

Conferences

- Iramnaaz, I., Sandoval, T., Zhuang, Y., Schellevis, H., & Rejaei, B. (2011). High quality factor RF inductors using low loss conductor featured with skin effect suppression for standard CMOS/BiCMOS. Electronic Components and Technology Conference (ECTC), 2011 IEEE 61st, 163-168.

- Iramnaaz, I., Xing, Y., Xue, K., Zhuang, Y., & Fitch, R. (2011). Graphene based RF/microwave impedance sensing of DNA. Electronic Components and Technology Conference (ECTC), 2011 IEEE 61st, 1030-1034.

About the Author

Sheena Hussaini was born in Hyderabad, India, on November 13, 1986. She received bachelors degree in electronics and communication engineering from Jawaharlal Nehru Technological University (JNTU), India in 2008. She joined Wright State University in September 2008 for Masters in electrical engineering and started working on research in RF/Microwave research laboratory. Her masters thesis was focused on Graphene based RF/Microwave impedance sensing and low-loss conductors for RF applications. She continued her studies as a Ph.D. candidate at Wright State in 2011. Her doctoral research is focused on Integrated Magnetic Components for Radio Frequency Applications. During her study at Wright State from 2010 until 2015 she served as graduate teaching assistant (GTA) and research assistant (GRA) at department of electrical engineering.

Sheena has published two journal papers in peer-reviewed IEEE journals and two papers in IEEE internal conferences. There are two more manuscripts in preparation to be submitted for publications in 2015. She has given two oral presentations at IEEE conferences and one poster presentation at local conference. She received IEEE best paper award at AIAA/ASME, 8th Dayton Engineering Sciences Symposium for category sensors in 2013 . She was awarded Ph.D. in engineering assistantship by college of engineering and computer science (CECS) at Wright State University in 2014. In November 2014, she joined Nokia as R&D Engineer in RF Mobile broadband.